Thermochemical dynamics of laser-irradiated semiconductor nanostructures

Bennett E. Smith

A dissertation
submitted in partial fulfillment of the
requirements for the degree of

Doctor of Philosophy

University of Washington

2016

Reading Committee:

Peter J. Pauzauskie, Chair

David J. Masiello

Philip J. Reid

Program Authorized to Offer Degree:
Department of Chemistry

University of Washington

Abstract

Thermochemical dynamics of laser-irradiated semiconductor nanostructures

Bennett E. Smith

Chair of the Supervisory Committee:
Assistant Professor Peter J. Pauzauskie
Materials Science & Engineering

Unique and novel applications of nanoscale materials are continuously being found. Applications span across many fields, including medicine, physics, chemistry, and engineering. Properties of nanoparticles are commonly studied through laser-mediated experiments, but the intense fields generated by laser light will often influence temperatures of the system under study, which may or may not be the intention of the experimentalist. Understanding and quantifying these thermal effects is beneficial, if not crucial, to the researcher. Our studies have focused on the interplay between intrinsic properties of a material, its dimensions, and its environment.

The main method utllized in the Pauzauskie group for studying individual nanoparticles is the optical trap, where a highly focused laser is used to isolate a particle from any supporting substrate. Although temperature studies in a laser trap were actively being pursued by the group, it was quickly realized that chemical reactions could be initiated by properly selecting the correct material. In chapter 2, experiments detailing the generation of reactive singlet oxygen species $^1O_2$ from trapped semiconducting nanowires will be described. The implications of potential reactions between the trapped structure and the $^1O_2$ molecules are then discussed.

In chapter 3, the nonlinear effects produced by the intense fields within an optical trap are addressed. Potassium niobate ($KNbO_3$) nanowires are selected as an ideal material for the

demonstration of second harmonic and sum frequency generation through the co-alignment of near-infrared lasers. It is shown that the unexpected heating found while trapping these supposedly unabsorbing particles can be attributed to the many crystallographic defects produced in the growth process as evidenced by high resolution transmission electron microscopy.

Final experiments were based on laser cooling of cadmium sulfide nanoribbons. Chapter 4 describes the implementation of a custom Raman system with a 532 nm source, necessary for the anti-Stokes excitation of the 2.42 eV band gap ($\sim$ 510 nm) for CdS. The ability to acquire Raman scattering spectra has been extremely beneficial to the group for a wide variety of experiments. As an example, the results of a high pressure-induced phase transition in silicon nanowires are given and discussed in terms of pressure vs. temperature as driving factors, where analytical theory developed in our lab was written into Python to simulate temperatures of nanowires under Raman excitation.

Finally, chapter 5 gives the details for initial, trapping experiments of CdS nanoribbons and results from an analytical solution to the heat equation. Although the combination of experimental results and analytical/numerical calculations prove useful in determining a nonlinear absorption coefficient for the nanostructures, it was ultimately decided that laser cooling of CdS suspensions was unlilkely due to the material's instability in aqueous media. The experiments were altered to monitor the resonance frequencies of cantilevered nanoribbons in vacuum to provide an orthogonal method for measuring temperatures of CdS nanoribbons under 532 nm excitation, compared to pump-probe techniques found in the literature. Results from temperature calibrations of nanoribbons show a Young's modulus temperature coefficient of $\sim$150 ppm/K which should allow for the detection of $\Delta T = -40K$ as claimed by others; however, measurements made in our lab have, so far, only shown heating.

Future efforts would benefit from determination of the quantum yields of individual

nanoribbons. If the assertions made that this is the first semiconductor to demonstrate laser cooling can be corroborated by independent techniques, it would provide clear evidence that the refrigeration is physically occurring; but without external verification, researchers will likely remain skeptical.

TABLE OF CONTENTS

LIST OF FIGURES

ACRONYMS

AFM: atomic force microscope

CSNR: cadmium sulfide nanoribbon

DAC: diamond anvil cell

DDA: discrete dipole approximation

EM: electromagnetic

MACE: metal-assisted chemical etching

NA: numerical aperture

NIR: near-infrared

PL: photoluminescence

QPD: quadrant photodiode

SAED: select area electron diffraction

SEM: scanning electron microscope

SINW: silicon nanowire

SOSG: Singlet Oxygen Sensor Green reagent

TEM: transmission electron microscope

TPL: two-photon photoluminescence

XRD: x-ray diffraction

YLF: yttrium lithium fluoride

ACKNOWLEDGMENTS

I would like to thank my advisor, Professor Peter J. Pauzauskie. His enthusiasm for learning and experimentation was an inspiration to me for the past 5 years and, I am certain, will continue to inspire future students for years to come. Likewise, I am appreciative to Professor Emeritus E. James Davis for all of his guidance and feedback and honored to have been able to collaborate on so many fruitful projects.

The Pauzauskie Lab has attracted many bright and creative people with whom it has been a pleasure to work. Among all the members of the group, there have been innumerable conversations that were valuable in both aiding active experiments as well as producing new projects altogether. Thanks to Dr. Leron Vandsburger, Dr. Paden Roder, Xuezhe Zhou, Matthew Crane, Matthew Lim, Automm Lombardo, Robert Hashimoto, Peter Meisenheimer, and Stuart Frazier for all their help.

I must also thank my family. My parents have been supportive of my education in every way since I was in grade school; their encouragement is always refreshing. I hope they're not too disappointed that I did not pursue plastic surgery...my winter home in Hawaii will be more shack than palace. And finally I am forever indebted to my wife: she has sacrificed more than anyone for my graduate school. Thank you for being such a caring and devoted mother to our amazing and indefatiguable children and such a loving and supporting partner during my physical and mental absence for the past 5 years.

DEDICATION

to my wife

and our beautiful children

Chapter 1
INTRODUCTION

As a newer research group, the Pauzauskie lab has spent the past 6 years developing expertise in essential analytical techniques as well as developing new and novel methods for synthesizing and characterizing the chemical and physical properties of micro- and nano-scale particles. My interest in light-matter interactions, or spectroscopy, helped the group to expand its abilities and infrastructure to better understand these processes at the microscopic and single-particle level. Since my arrival, the facilities have grown from a microscope and simple, near-infrared (NIR) single-beam optical trap, to include integrated Raman scattering and photoluminescence (PL) systems with additional excitation sources in the visible spectrum, co-alignment of mulitple NIR beams for multiple traps and nonlinear optical studies, a diamond anvil cell for high-pressure studies up to 30 GPa, a cryostat for low-T and/or low pressure measurements, and most recently, pulsed laser control and an avalanche photodiode for PL lifetime measurements. The development and implementation of these systems and equipment have allowed me, and the group as a whole, to explore a wide variety of projects while building the knowledge base and experimental infrastructure to complete the targeted project of photothermally cooling (or heating) CdS cantilevers. With this dissertation, my hope is to describe the techniques I have developed for our group and their associated, completed projects before detailing the final experiments pertaining to laser cooling of semiconductor nanomaterials.

1.1 Optical Trapping

The first assembled instrument in our laboratory was a single-beam optical trap, seen in figure 1.1a. An optical trap has the unique capability to manipulate and study single particles in

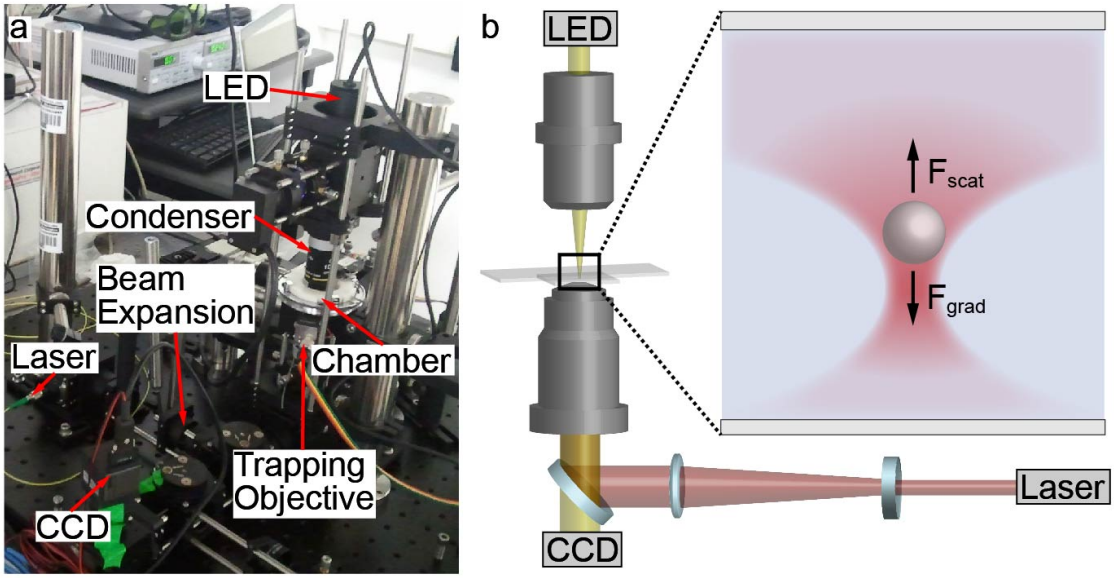

Figure 1.1: (a) Photograph of the optical trap used by the Pauzauskie lab in early 2012. (b) Schematic outlining the basic components and forces in an optical trap.

isolation from any substrate. To realize optical trapping, a laser beam is expanded to overfill the back aperture of a high numerical aperture (NA) objective, typically an oil- or water-immersion objective, which focuses the beam to a diffraction limited spot within a suspension of the particles of interest. Although this is all that is necessary for the trapping process to occur, it would be a little benefit to the user if the trapped particle could not be observed; therefore, a white light source and a focusing objective (often referred to as the "condenser") are placed opposite from the trapping objective with an appropriate dichroic mirror inserted into the system for imaging onto a CCD camera (Fig. 1.1b). The first demonstration of optical trapping was by Arthur Ashkin in 1986 and the physics that permit a dielectric particle to be trapped in an electric field gradient are described in his seminal paper [1]. Essentially, there are two competing forces generated: the forward force due to transferred momentum from the scattered photons, described by

$$F_{scat} = \frac{k^4 \alpha^2}{6\pi c n_0^3 \epsilon_0^2} I(\mathbf{r}) \hat{z} \tag{1.1}$$

and the Lorentz force caused by the induced dipole in the in the electromagnetic (EM) field gradient,

$$F_{grad} = \frac{1}{2}\alpha \nabla E^2. \tag{1.2}$$

The sum of these competing forces results in a slightly downstream displacement of the particle relative to the field maximum.

While residing in the potential well generated by the electric field gradient, the particle will continue to undergo a Brownian motion as a result of the momentum transfer from colliding solvent molecules. The complex motion due to the different forces acting on the particle is dependent on temperature, which will be discussed in detail in Sec. 2.1. Therefore, if the forward-scattered laser light can be monitored, an analysis of the motion can be used to extract temperatures of trapped particles. The literature on optical trapping often ignores or makes assumptions regarding the temperatures of trapped particles, so the group's initial studies of photothermal effects on particles in a laser tweezer (LT) system not only formed the background to further explore laser refrigeration in a LT but also provided the field with additional insight into potential heating due to the intense fields produced by an optical trap.

1.2 Laser Cooling

The concept of laser cooling through anti-Stokes photoluminescence was initially proposed by Pringsheim in 1929 [2]. Initial skepticism that the process would violate the second law of thermodynamics was addressed when, in 1946, Landau described the entropy of light and how it should be included in the description of the cooling system [3]. His analysis demonstrated that the entropy of incident and emitted light is proportional to the solid angle and bandwidth (see Sec. 5.4). Consequently, using a light source with the narrowest beam and frequency profile (e.g. laser) to excite fluorescence with isotropic spatial emission and broad bandwidth will result in the highest cooling efficiency [4], regardless of the cooling medium (e.g. atomic, molecular, rare-earth ion, semiconductor). The ability to refrigerate

solid-state materials without moving parts (e.g. fans, pumps) or cryogens (e.g. liquid nitrogen, liquid helium, etc.) would be beneficial for a number applications, including photodetectors and athermal lasers. Our group has been exploring both the cooling of rare-earth doped crystals [5] and, more recently, semiconductor nanostructures [6].

1.2.1 Rare-earth glasses and crystals

The first experimental demonstration of laser refrigeration of a solid was not until 1995 when Epstein et al. [7] were able to cool an ytterbium-doped glass, ZrF_4-BaF_2-LaF_3-AlF_3-NaF-PbF_2 (ZBLANP), by 0.3 K. Since then, a variety of hosts, including $KGd(WO_4)_2$ [8], $BaYF_4$ [9], $Y_3Al_5O_{12}$ (YAG) [10], and $YLiF_4$ (YLF) [11], among many others [12], have been tested with successful cooling results. Additionally, other trivalent rare-earth dopants (Tm^{3+} [13] and Er^{3+} [14]) have been shown to cool in various host materials. In terms of absolute temperatures, the most recent achievement was a record of 91 K for a 10% Yb^{3+}-doped YLF crystal in vacuum [11].

With all the progress made for various hosts, ions, concentrations, etc., it had not yet been determined if any system could be refrigerated in water. Specifically, it was uncertain if the cooling power of an Yb-doped crystal could be sufficient to refrigerate an aqueous solution. Using temperature measurement methods outlined in section 2.1, our group has found that microscopic 10% Yb^{3+}-doped YLF crystals can be optically trapped at wavelength of 1020 nm to induce cooling of the crystal and, consequently, the local fluid [5]. Specifically, we were able to use a hydrothermal synthesis to produce micrometer-scale square bipyramids of YLF with a 10% Yb^{3+} concentration and subsequently show their potential for trapping in a NIR LT (Fig. 1.2a). The trivalent ytterbium ion has an electronic configuration of $[Xe]4f^{13}$ which can be equivalently viewed as consisting of a the closed xenon shell and a single hole. A single hole in the $4f$ shell will have spin $s = 1/2$ and orbital angular momentum $l = 3$. Consequently, the total spin and orbital angular momentum are $S = 1/2$ and $L = 3$. For rare earth metals, spin-orbit coupling is of considerable magnitude and is described by the total angular momentum quantum number, $J = |L - S|, ..., |L + S|$, meaning the ^2F state is split

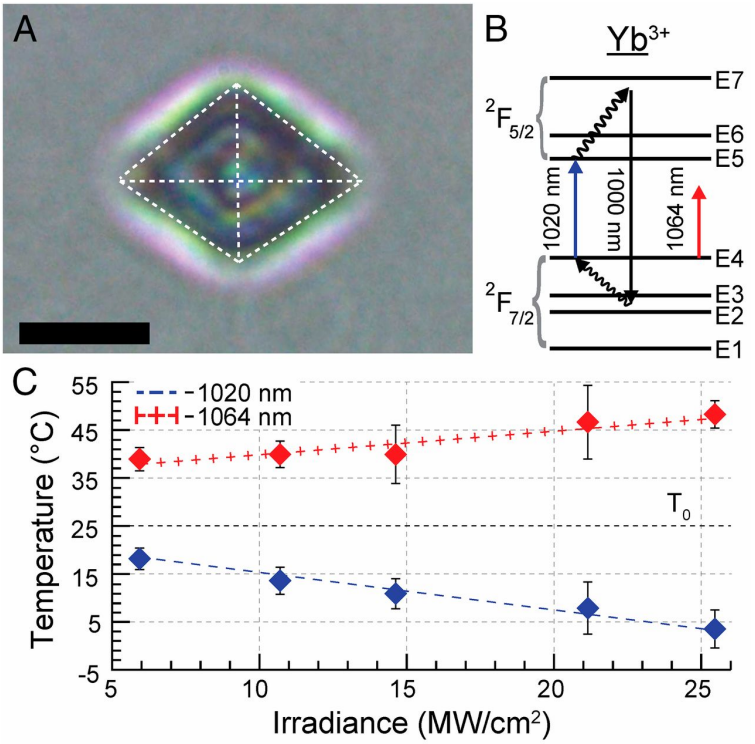

Figure 1.2: Laser refrigeration of optically trapped YLF microcrystals. (A) Optical micrograph of an optically trapped YLF crystal. (Scale bar, 3 μm.) (B) Crystal-field energy level configuration of Yb^{3+} dopant ions and used cooling scheme. (C) Extracted temperature (T_p) of optically trapped particles in D_2O as determined using the outlined CBM analysis. Yb^{3+}-doped YLF particles are shown to cool when trapping wavelength is resonant with the E4 - E5 transition (λ = 1,020 nm) but heat when the trapping wavelength is below the transition (λ = 1,064 nm). Reprinted with permission from [5].

into two manifolds, $^2F_{7/2}$ and $^2F_{5/2}$, with an energy difference corresponding to a wavelength of $\sim$1 μm [15]. Spherical symmetry in an isolated ion would result in a simple two level system. However, the degeneracy of each level is lifted due to the non-spherically symmetric arrangement of charges from the ions in the crystal lattice. In the case of $YLiF_4$, the low symmetry of the scheelite (tetragonal) structure splits the $^2F_{7/2}$ and $^2F_{5/2}$ manifolds into 4 and 3 levels, respectively (Fig. 1.2b) [16]. The trivalent lanthanide ions still retain their $5s$ electrons, so they remain fairly shielded from the crystal field resulting in weak crystal field splitting. In the case of laser refrigeration, although a larger splitting would increase efficiency

by producing a larger difference in the excitation (λ_p) and average emission ($\bar{\lambda}_L$) wavelengths ($\eta_{cool} = (\lambda_p - \bar{\lambda_L})/\bar{\lambda_L}$) weaker splitting actually enhances cooling at lower temperatures by maintaining a significant population at the ground state manifold edge [15].

The cooling of an Yb^{3+}-doped material is maximized by pumping electrons from the $E4$ level to $E5$ level. In the case of Yb^{3+}:YLF, this transition corresponds to a wavelength of 1020 nm. After excitation, the long lifetime of the Yb^{3+} excited state allows the manifolds to thermalize so that subsequent radiative relaxation results in emission of greater energy. However, if a laser of insufficient energy to excite from $E4$ to $E5$ is used, obviously the mechanism of cooling cannot proceed. In our experiments, this exact comparison is made by trapping microcrystals at 1020 nm or 1064 nm resulting in cooling or heating, respectively, as the laser power is increased (Fig. 1.2c).

As an independent method for confirming the cooling observed with trapped YLF crystals, ratiometric emission of the $^2H_{11/2}$ to $^4I_{15/2}$ and $^4S_{3/2}$ to $^4I_{15/2}$ transitions, which has been demonstrated previously as a reliable method for thermometry [17], was used to qualify heating under a 975 nm illumination and cooling under a 1020 nm illumination (Fig. 1.3C). The visible emission, which is bright enough to be seen by the naked eye (Fig. 1.3A, right panel), is produced as a result of energy transfer from the excited Yb^{3+} ions to the Er^{3+} ions. The long lifetimes of the relevant states (>100 μs) allow the population of two states to come to a thermal equilibrium where the relative intensities can be described by the Boltzmann distribution,

$$\frac{I_2}{I_1} \propto \exp\left(\frac{-(E_2 - E_1}{k_b T}\right). \tag{1.3}$$

The bright emission can then be collected and passed into a spectrometer to resolve the individual transitions (Fig. 1.3). Then, using a custom written Matlab script (see Appendix A.1), the ratio of the two bands can be used to infer trends regarding the crystal's internal temperature relative to the laser power. The absolute temperature, unfortunately, could not be extracted using this method due to inconsistent ratios between individual particles, thereby precluding the application of an ensemble calibration [5]. Although the introduction

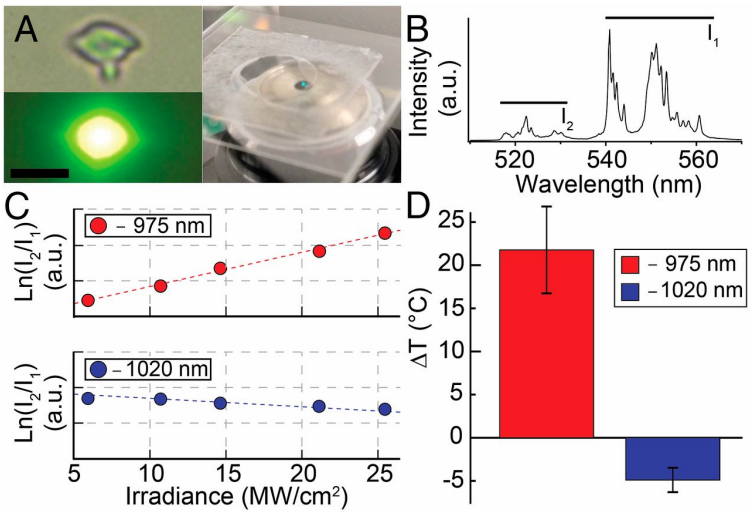

Figure 1.3: Upconversion and ratiometric thermometry of codoped YLF. (A) Bright-field optical micrograph showing a codoped 2%Er^{3+},10%Yb^{3+}:YLF particle in Brownian motion (Top Left) and a dark-field optical micrograph of the crystal when trapped with λ = 1,020 nm (Bottom Left). (Scale bar, 4 μm.) Upconverted photoluminescence can be seen with the unaided eye (Right). (B) Photoluminescence spectra of the corresponding dark-field image showing the integration regions I_2 and I_1, representing emission from Er^{3+} energy states E_2 ($^2H_{11/2}$) and E_1 ($^4S_{3/2}$) to the ground state E_{ground} ($^4I_{15/2}$), respectively. (C) Natural logarithm of the ratio I_2/I_1 showing a linear increase (Top) with laser irradiance at λ = 975 nm and a linear decrease (Bottom) with laser irradiance at λ = 1,020 nm. (D) Laser refrigeration of the codoped YLF crystal analyzed in (C) measured via CBM analysis at an irradiance of 25.5 MW/cm^2. Reprinted with permission from [5].

of non-radiative pathways through the many electronic states found in the Er^{3+} ion reduces the cooling efficiency of the crystal relative to the purely Yb^{3+}-doped YLF crystal, an average ΔT of -5 °C is observed (Fig. 1.3) for trapping at 1020 nm while ΔT = +22°C for 975 nm.

1.2.2 Semiconductors

Rare earth (RE)-doped crystals have achieved the lowest temperature to date for solid-state refrigeration [11], but there is a great interest in laser cooling of semiconductors due to its increased potential for reaching temperatures closer to absolute zero. For RE-doped materials, the low density of RE ions results in a Maxwell-Boltzmann distribution of electrons, such

that as temperature decreases the probability of an electron populating the $E4$ state will also decrease (Fig. 1.4a). Experimentally, I have observed the decrease in quantum yield of a Czochralski-grown 5%Yb^{3+}-doped $YLiF_4$ crystal as a result of the decrease in the $E4$ level population as seen in Fig. 1.5. For semiconductors, however, the distribution of electrons in the valence band obey Fermi-Dirac statistics, meaning the band edge will remain populated even at 0 K (Fig. 1.4b).

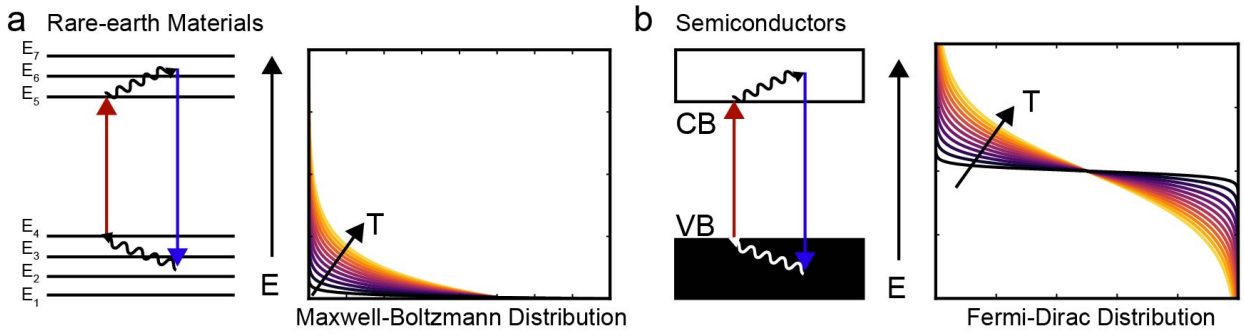

Figure 1.4: Representation of the laser refrigeration process and temperature-dependent statistical distributions for different materials. (a) For Yb^{3+}-doped materials, the trivalent ions can be treated with Maxwell-Boltzmann statistics which predicts decreased populations of the $E4$ level as temperature decreases. (b) Semiconductors obey Fermi-Dirac statistics which means that the valence band (VB) edge would remain populated even at absolute zero, allowing for continued excitation to the conduction bamd (CB).

Experimentally, a claim was made in 1999 of having cooled gallium arsenide quantum wells by 10% [18]. However, discussion of high carrier densities' effect on the photoluminescence and interpreted temperature cast doubt on the initial report [19]. More recently, nanoribbons of cadmium sulfide have been reported to cool by 40 K from room temperature by Zhang et al. (Fig. 1.6) [6]. In their experiments, an isolated CdS nanoribbon was suspended over a small (3 x 3 μm) cavity etched into the supporting Si substrate and irradiated by a laser (514 or 532 nm) which is red-tuned relative to the material's band gap (E_g) for anti-Stokes refrigeration. To probe the temperature, the green laser was momentarily blocked while a blue laser ($h\nu > E_g$) briefly illuminated the same ribbon and photolumi-

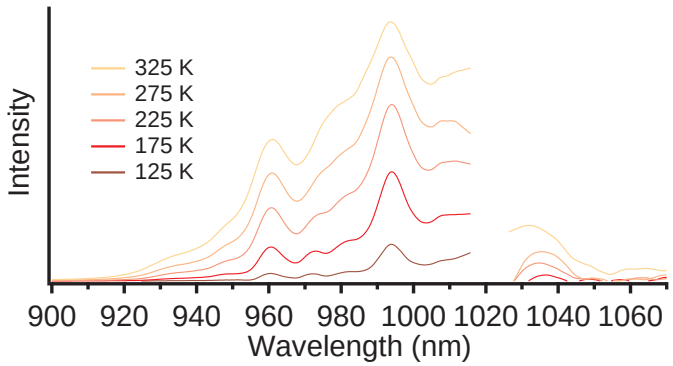

Figure 1.5: Temperature dependent photoluminescence spectra of Czochralski-grown 5%Yb^{3+}-doped $YLiF_4$ demonstrating a decreasing quantum yield with reduced temperatures.

nescence (PL) was collected and compared to temperature calibrated PL. But, so far, the results have not yet been duplicated and given the propensity for misinterpreting semiconductor luminescence spectra as they pertain to internal temperature, it would benefit the community to provide additional methods for determining temperatures of micro- and nanoscale structures. The initial goal of my research was to attempt reproduction of the laser cooling of CdS nanoribbons through the same optical trapping technique used on Yb^{3+}:YLF microcrystals; however, as it will be pointed out it Sec. 5.4, cooling of un-passivated ribbons in an aqueous medium is improbable, so my experiments were adjusted to monitor the temperature-dependent mechanical resonances of cantilever nanoribbons in vacuum.

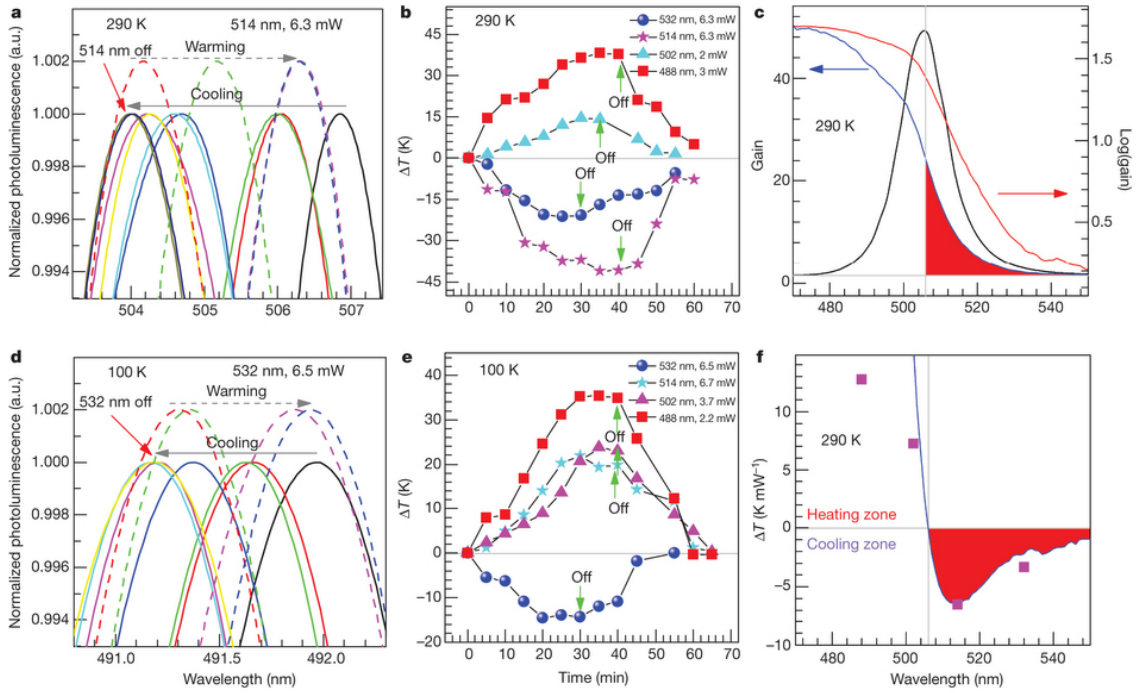

Figure 1.6: **a**, Evolution of PPLT spectra starting from 290 K, pumped by a 514-nm laser with a power of $\sim$ 6.3 mW. Solid curves represent the cooling cycle, and the dashed curves represent the warming up after the pump laser is switched off. Dashed curves are shifted vertically for clarity. **b**, Temperature change, ΔT, versus time pumped by four laser lines (532, 514, 502 and 488 nm), using data extracted from the PPLT spectra (shown in **a** for 514-nm pumping) and corresponding calibration curve around 290 K. **c**, Photocurrent gain spectrum (linear scale, blue; logarithmic scale, red) and Stokes photoluminescence spectrum (black) of a single CdS nanobelt at 290 K. **d**, Evolution of PPLT spectra for another nanobelt pumped by a 6.5-mW, 532-nm laser starting from 100 K. We observe cooling and warming cycles similar to those in **a**. **e**, Temperature change, ΔT, versus time pumped by four laser lines (532, 514, 502 and 488 nm), using data extracted from the PPLT spectra (shown in **d** for 532-nm pumping) and the corresponding calibration curve around 100 K. **f**, Summary of measured maximum ΔT (pink squares) and theoretically calculated temperature change (blue curve) normalized to pump power for different pump wavelengths at 290 K. In **c** and **f**, the red regions correspond to the cooling zone. Reprinted with permission from [6].

Chapter 2

OPTICAL TRAPPING OF SILICON NANOWIRES

As discussed in Sec. 1.1, one of the first instruments and experimental methods built for the group was a single-beam optical trap. Briefly, a laser beam is focused down to a diffraction limited spot producing intense electromagnetic fields able to induce a dipole in nearby, suspended nano- and micro-sized particles. These polarized particles are attracted to the maximum of the electric field gradient and can be pulled into the trap.

2.1 Temperature Extraction in an Optical Trap

Considering all the forces, including trapping potential and the stochastic bombardment of fluid molecules (i.e. Brownian motion), that are acting on the particle, its complex motion can be described by the Langevin equation,

$$m\ddot{x}(t) + \gamma_0\dot{x}(t) + \kappa x(t) = (2k_BT\gamma_0)^{1/2}\eta(t). \tag{2.1}$$

Here, $x(t)$ is the particle's position, m is its mass, γ_0 is the friction coefficient, and κ is the spring constant produced by the harmonic potential of the laser trap. The term $(2k_BT\gamma_0)^{1/2}\eta(t)$ represents the random motion due to Brownian forces at an absolute temperature T. For spherical and 1-dimensional particles, the Stokes drag coefficient can be expressed as

$$\gamma_0 = 6\pi R\nu(T) \qquad \text{(spherical)} \tag{2.2}$$

$$= \frac{4\pi L}{\ln L/2R + 0.84}\nu(T) \qquad \text{(1D)} \tag{2.3}$$

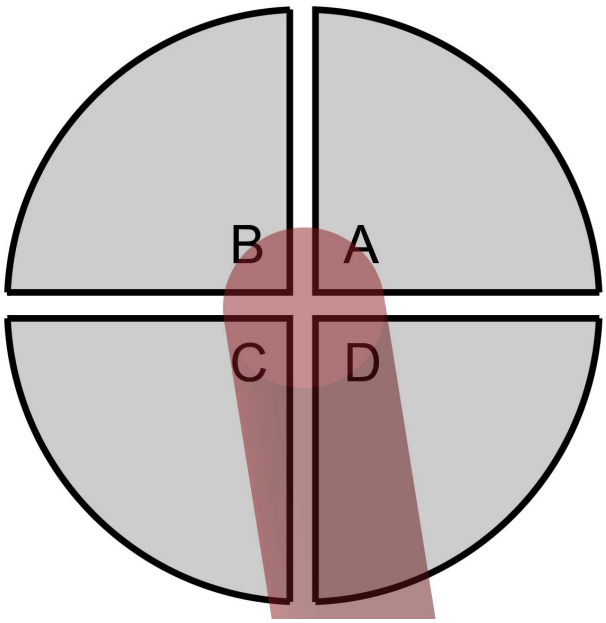

Figure 2.1: Schematic of a quadrant photodiode which is used to monitor the Brownian dynamics of an optically trapped particle through photovoltages produced by the forward-scattered laser light.

where R is the sphere or nanowire radius, L is the length of the 1D particle, and $\nu(T)$ is the temperature-dependent viscosity of the surrounding fluid. In the case of the 1D particle, the factor of 0.84 is the result of effects due to end facets [20]. A characteristic time for the loss of kinetic energy due to friction, $t_{inert} \equiv m/\gamma_0$, is smaller than the experimental sampling rate by a factor of 10^{-3} [21]. We can therefore drop the initial term in Eq. 2.1, which then gives

$$\dot{x}(t) + 2\pi f_c x(t) = (2D)^{1/2}\eta(t), \tag{2.4}$$

where the corner frequency, $f_c \equiv \kappa/(2\pi\gamma_0)$, and Einstein equation of diffusion,

$$D = k_B T/\gamma_0, \tag{2.5}$$

have been introduced.

To obtain temperatures from trapped particles, the LT setup was modified from the simple system outlined in Fig. 1.1 by introducing another NIR dichroic mirror, a quadrant photodiode (QPD), and a piezo controlled stage (Fig. 2.2). This allows the forward-scattered laser light to be reflected and focused onto the QPD for analysis. A QPD consists of 4 identical detectors where each occupies a quadrant and provides its respective photocurrent: $A,\ B,\ C,\ D$ (see Fig. 2.1). The forward-scattered laser light is focused into the center of the QPD and the position is monitored by the relative signals from each of the quadrants:

$$X = \frac{(B+C)-(A+D)}{A+B+C+D} \tag{2.6}$$

$$Y = \frac{(A+B)-(C+D)}{A+B+C+D}. \tag{2.7}$$

The time-dependent voltage signals from the QPD are then Fourier transformed which results in a Lorentzian profile representing the thermal motion of the particle in the trap as a function of frequency, written as

$$P_T(f) = \frac{D}{\pi^2(f^2+f_c^2)}. \tag{2.8}$$

However, the initial transformation of voltage signal gives an uncalibrated power spectrum. To extract a diffusion constant in relevant units, we have utilized a technique outlined by Tolić-Nørrelyke et al. [23]. Briefly, a piezo stage is controlled electronically to oscillate the trapped particle at a particular frequency, f_{drive}, and amplitude, A, which corresponds to a spike in the power spectrum (Fig. 2.2c) and a new description of the Lorentzian

$$P(f) = P_T(f) + P_{response}(f) = \frac{D}{\pi^2(f^2+f_c^2)} + \frac{A^2}{2(1+f_c^2/f_{drive}^2)}\delta(f-f_{drive}). \tag{2.9}$$

If we can assume a linear relation between position in meters and position volts, that is

$$x(t) = \beta x^{volt}(t), \tag{2.10}$$

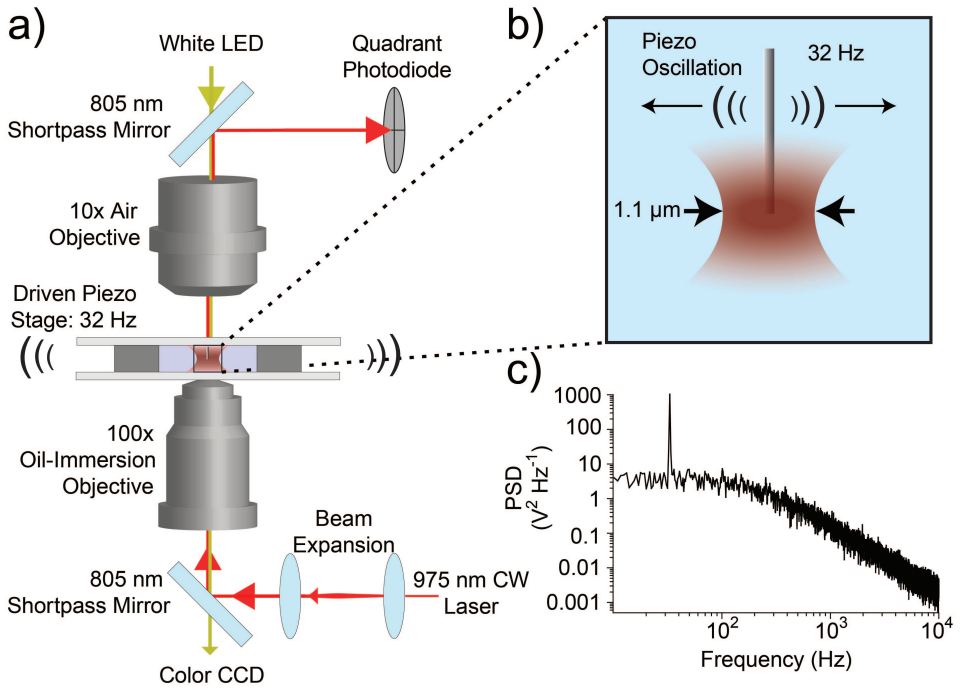

Figure 2.2: Method for extracting temperatures from trapped particles. (a)Schematic of the modified LT system including an 805 shortpass mirror, quadrant photodiode, and electronically controlled piezo stage. (b) Schematic of a trapped silicon nanowire with an of oscillation 32 Hz. (c) Example power spectral density (PSD) of a trapped nanowire with spike produced at 32 Hz due to stage oscillation. Reprinted with permission from [22].

then the power spectrum can be calibrated according to the relation

$$P_{response}(f) = \beta^2 P^{volt}_{response}(f). \tag{2.11}$$

The calibration factor is

$$\beta = \sqrt{W_{th}/W_{ex}} \tag{2.12}$$

where W_{th} is the theoretical power determined by the actual movement of the stage, given as

$$W_{th} = \frac{A^2}{2(1 + f_c^2/f_{drive}^2)}, \tag{2.13}$$

and the experimental power, W_{ex}, is found by observing the spike in the power spectrum,

$$W_{ex} = [P^{volt}(f_{drive}) - P_T^{volt}(f_{drive})]\Delta f. \tag{2.14}$$

With β determined, a diffusion constant in m^2/s can be calculated and a temperature extracted according to Einstein's equation, (Eq. 2.5). The implementation of the signal acquisition and analysis was conducted using LabView software. Outlines of the associated block diagrams can be seen in Appendix A.3.

2.2 Initial Experiments on Photothermal Heating of Silicon Nanowires

Silicon is the second most abundant element in the earth's crust, by mass, and, as a high-purity semiconductor, has become the foundation for modern technology. Its low cost, strong literature presence, and simple, albeit often hazardous, handling and preparation protocols made it a suitable material for the group's initial studies on LT photothermal heating.

To obtain silicon nanowires [24], high purity silicon wafers were immersed in a 1:1 solution of 10 M HF:0.04 M $AgNO_3$ for approximately 3 hours. The proposed mechanism for etching suggests that Ag^+ ions are reduced at the surface of the Si wafer, thereby introducing local positive carriers (i.e. holes) into the Si. The net positive charge at the silicon surface directly

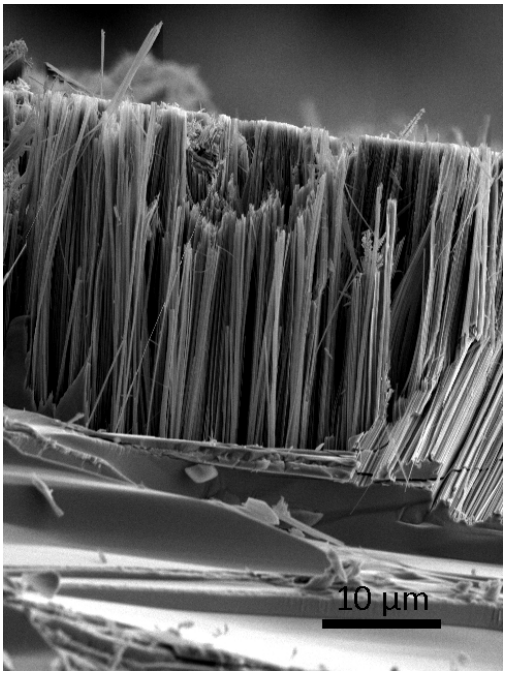

Figure 2.3: Scanning electron micrograph of silicon nanowires after etching

beneath the Ag deposits will attract transient HF_2^- species, consequently etching the Si and leaving pillars with lengths proportional to the etch time but little control over diameter (Fig. 2.3). The deposited silver film can then be removed by immersing the wafer in a 1:1 solution of 30% NH_4OH:30% H_2O_2. Once the array of silicon nanowires (SiNWs) have been prepared, ultrasonication in a solvent (typically aqueous) will generate a suspension of SiNWs that can be used for trapping experiments. The indirect band gap of Si results in very little absorption, even at energies greater than the 1.1 eV band gap. As a result, very little heating of intrinsic SiNWs is observed [22, 25]. To increase the absorption of SiNWs, ion implantation can be used to damage the lattice and introduce dopant atoms. The amorphization of the lattice can increase heating through scattering, while activated dopants can act as recombination centers.

One example from our group's work is the relative heating of intrinsic, Si-doped and Au-doped SiNWs in a NIR optical trap [22]. In these experiments, SiNWs were trapped

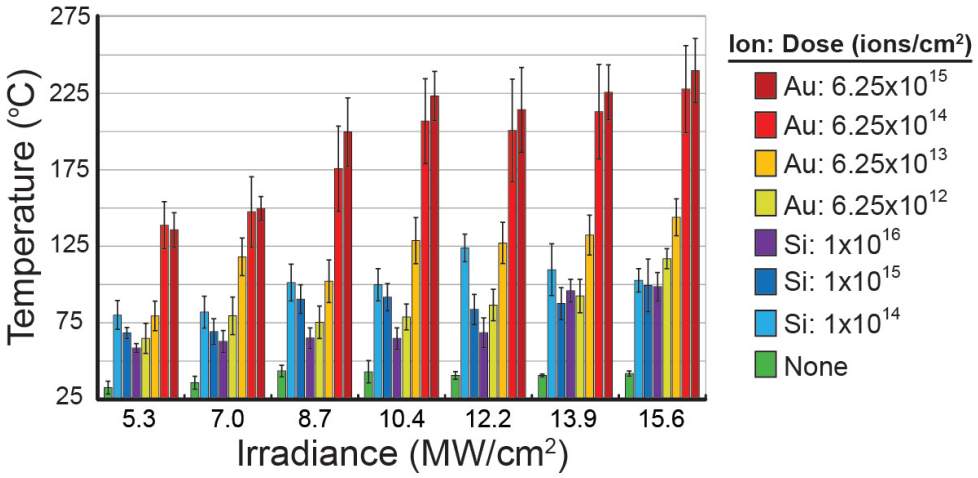

Figure 2.4: Results from laser tweezer temperature measurements of intrinsic, Si-implanted, and Au-implanted SiNWs. Reprinted with permission from [22].

at a wavelength of 975 nm and at irradiances from 5 to 15 MW/cm^2 (Fig. 2.4). It was found that intrinsic SiNWs heated very little above room temperature. If the SiNWs were implanted with Si ions, the induced lattice damage resulted in increased heating. Although, no correlation between temperature and increasing Si ion concentration was observed for the implantation doses used. This suggests that the ion dosages tested were already past a saturation limit of lattice damage. If Au ions are used, however, a significant increase in temperature with increasing ion dosages is found, even to the point of superheating water, which has been reported previously [26] occurs due to the high pressures needed to nucleate bubbles at the nano-scale.

During the course of these initial SiNW heating experiments, peculiar morphologies were occasionally observed during atomic force microscopy (AFM) measurements. For example, Fig. 2.5 shows a SiNW deposited onto a glass slide after having been optically trapped. One end of the nanowire appears slightly enlarged in diameter. It was proposed that some photo-induced reaction between the SiNW and local environmental molecules (e.g. H_2O, O_2) could be occurring in the LT. As a result, my first independent experiments as a member of the laboratory were to test whether a reaction was proceeding during trapping experi-

ments. I would eventually learn that generation of reactive oxygen species from silicon was a well known phenomenon [27–30], but my experiments would provide evidence that chemical reactions, whether adverse or desired, could be initiated in an optical trap.

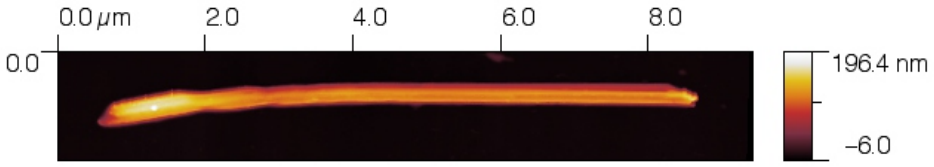

Figure 2.5: Measurement taken with an atomic force microscope showing a SiNW nanowire deposited onto a glass slide after optical trapping. One end of the nanowire appears larger in diameter, possibly due to photo-induced oxidation during trapping.

2.3 $^1O_2$-generation from Silicon Nanowires

Photodynamic therapy has been used over the past two decades to clinically treat metastatic tumors through the conversion of naturally available triplet-oxygen molecules ($^3O_2$) into highly reactive singlet oxygen ($^1O_2$) [31]. Singlet oxygen then reacts with a range of proteins, lipids, and nucleic acids in vivo to prevent angiogenesis within [32, 33] and metastasis from solid tumors [32, 34]. In this process, visible light is absorbed by an intermediate photosensitizing molecule (e.g., Photofrin [35]) to create electronic excited states that then transfer their energy to $^3O_2$ molecules, converting them to $^1O_2$ through a triplet-triplet annihilation process.

Even though photodynamic therapy (PDT) has been studied for well over a century it has only been in clinical use since 1993 [31] and currently there are a dozen FDA-approved photosensitizers based on small molecules [36]. Two of the primary challenges of using molecular PDT agents is their long in vivo half-lives and also their non-specific distribution throughout the body of a patient [35]. This often leads to extended (week-long) periods of time in which a patient must avoid direct exposure to sunlight. For this reason, researchers have

been studying novel ways of targeting tumor cells including micellar [37] and liposomal [38] systems, carbon nanotubes [39], gold nanoparticles [40], and porous silica [41] or silicon [42] materials as well as exploring new solid-state nano-materials, including metals [43, 44] and semiconductors [28, 45], as direct photosensitizers with predominant excitation wavelengths in the visible spectral window. In particular, silicon nanocrystals have been shown to sensitize singlet oxygen [27, 46] and have the benefit of biodegradability [47] as opposed to inert materials like gold nanocrystals.

The shape of nanoscale materials has also been shown to affect uptake within targeted tumor cells [48–50] due in part to the high surface area to volume of one-dimensional materials [51]. Furthermore, recent theoretical calculations have shown [52] that silicon nanowires can be designed to exhibit significant morphology dependent resonances during photothermal laser heating. In this way, the shape of nanostructures can be optimized to enhance the uptake and optical absorption relative to small molecule pharmaceuticals with fixed sizes and absorption coefficients.

The phototoxicity of silicon nanomaterials under illumination with wavelengths in the blue spectral region ($450 < \lambda < 500$ nm) has also been demonstrated [28]. Blue light, however, lies outside the NIR biological transparency window resulting in a low tissue penetration depth which has motivated recent experiments with photoexcitation of both gold nanocrystals [53, 54] that can absorb light via plasmon resonance, and upconverting nanocrystals [55, 56] that excite surface-grafted PDT molecules following the upconversion of rare-earth ions in nanocrystalline fluoride host materials. Photoexcitation of silicon nanostructures in the NIR would increase the penetration depth and expand silicon's potential as a PDT agent [42]. We demonstrate here that NIR laser radiation ($\lambda = 975$ nm) can be used to optically excite individual silicon and gold nanowires for the local generation of $^1O_2$ within a single beam optical trap.

Silicon nanowires were synthesized from p-type silicon wafers using metal assisted chemical etching (MACE) with silver as the active etching metal [24]. High-angle annular dark field transmission electron microscopy (HAADF TEM) was used to confirm the presence of

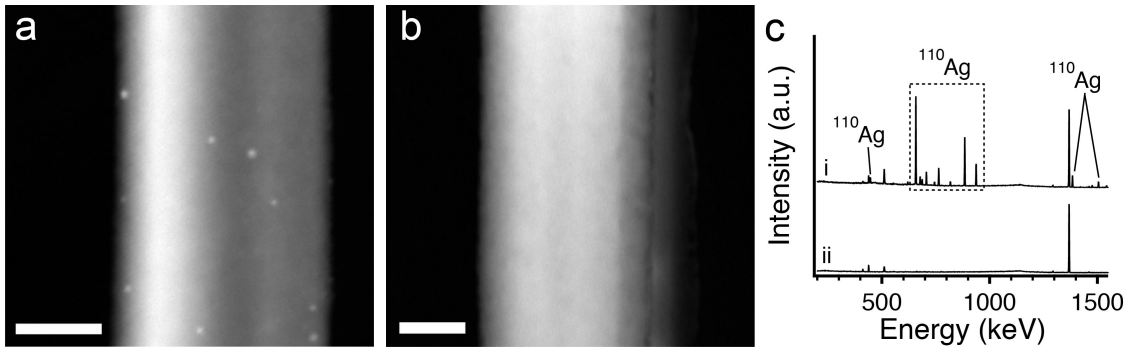

Figure 2.6: (a) High-angle annular dark field TEM image of a single silicon nanowire without silver etching, demonstrating the presence of silver deposits. Scale bar = 50 nm. (b) High-angle annular dark field image of a silver-etched silicon nanowire with no detectable silver. Scale bar = 50 nm. (c) Neutron activation analysis of (i) silicon nanowire array before (i) and after (ii) silver-etching process.

silver domains on SiNWs following their synthesis (Figure 2.6a). TEM imaging also confirms that the silver nanocrystals can be removed following an aqueous etching step that dissolves silver (Figure 2.6b). Given that metallic nanocrystals [57] have recently been demonstrated to generate singlet oxygen, it must be implicitly ruled out that there is no residual silver to interfere with the experimental measurements.

Neutron activation analysis (NAA) is a sensitive measure of metallic elemental composition and was used to analyze the residual amount of silver both with and without the silver-etch (Figure 2.6c). The distinct gamma-ray emission from the ^{110}Ag isotope decay was used to identify and quantify the silver concentration in the SiNWs. Before silver etching, the Ag concentration is measured to be 291 ppm, whereas after silver etching the amount of Ag is below the detection limits of NAA (< 100 parts per trillion).

The surface of silicon nanowires following MACE in hydrofluoric acid is expected to be hydrogen terminated, however the metal-etching step is highly oxidative and may also oxidize the surface of silicon nanowires. Fourier-transform infrared absorption spectroscopy on silicon nanowires following the silver-etching step reveals the presence of a silicon dioxide passivation layer that is also confirmed by oxygen k-edge scanning transmission x-ray ab-

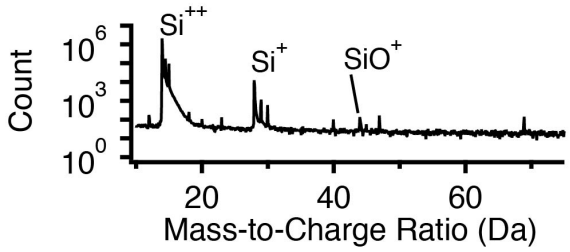

Figure 2.7: Atom probe tomography (APT) mass spectrum from a single SiNW demonstrating no detectable silver signal (Ag^{+}: 107 Da, Ag^{++}: 53.5 Da).

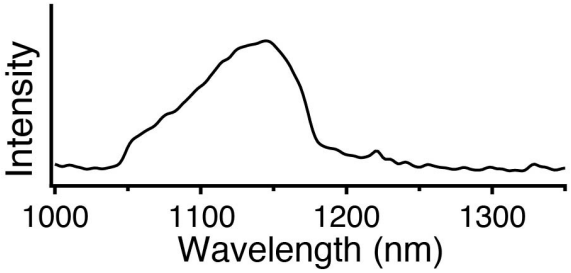

Figure 2.8: Photoluminescence of SiNWs excited by a 975 nm laser source.

sorption microscopy. Atom-probe tomography measurements on silicon nanowires further confirm the presence of a surface oxide layer, as well as the absence of silver in the bulk of the nanowires following the silver etch (Figure 2.7).

Laser trapping of individual nanowires was performed using a custom instrument shown in Figure 2.9a. A 975 nm laser is expanded to overfill the back aperture of a 100x oil immersion objective (NA=1.25) and then focused into a chamber with an aqueous nanowire suspension. The silicon nanowires are trapped and photoexcited by the 975 nm (1.27 eV) laser (Fig. 2.9b), which is above silicon's band gap (1.11 eV), to produce excitons as evidenced by the observation of excitonic emission from SiNWs after Ag etching (Figure 2.8), where 75% of the excitons are in a triplet state [58]. The excitons then diffuse to the surface and, through a Dexter electron exchange mechanism, excite molecular oxygen in solution to the singlet state (Figure 2.10a) via a triplet-triplet annihilation process.[46] Singlet oxygen molecules

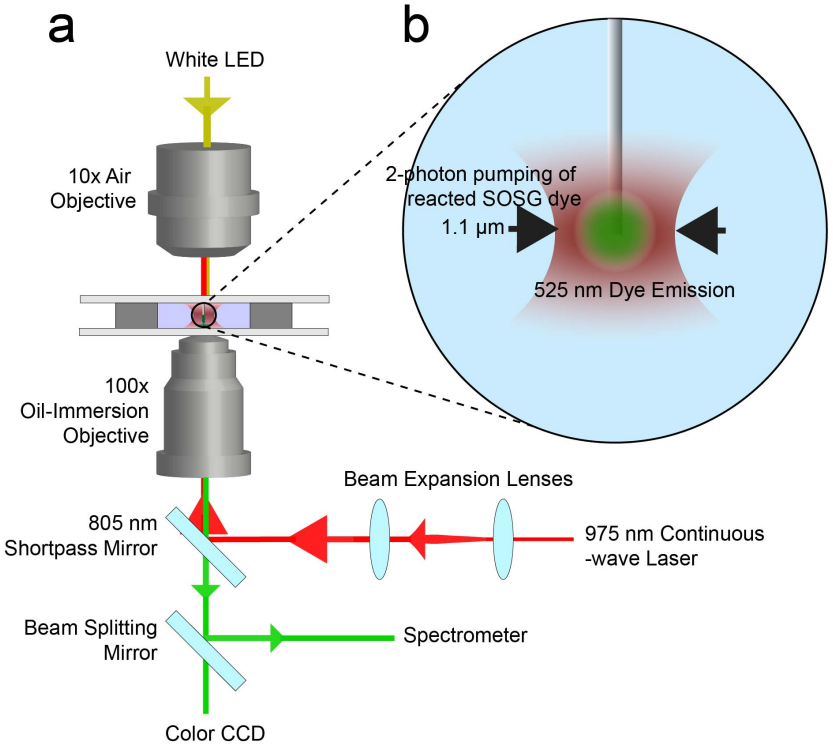

Figure 2.9: (a) Schematic outlining the components used in the trapping experiments. (b) Depiction of a nanowire trapped with the focused Gaussian, NIR laser (beam waist = 1.1 μm) in a solution of SOSG with localized pumping of reacted SOSG.

have been reported to have a decay time of 3.7 μs in water, leading to diffusion distances on the order of 250 nm from the silicon-water interface[59] at room temperature. Singlet-oxygen excited states can also relax to their ground state through emission of a photon at 1270 nm. However, their long lifetimes at room temperature also allow for reactions with Singlet Oxygen Sensor Green (SOSG) molecules, which selectively exclude reaction with superoxide anions and peroxide [60], to make a 1,4-endoperoxide, SOSG-EP (Fig. 2.10b).

In addition to trapping single silicon nanowires and photoexciting triplet excitons in silicon, the laser trap also has a sufficient irradiance ($\sim$MW/cm^2) for two-photon photoexcitation (2PPE) of SOSG-EP to the electronic excited state, SOSG-EP* (Figure 2.11). The green emission from SOSG-EP* can be visualized through use of a CCD camera (Figure

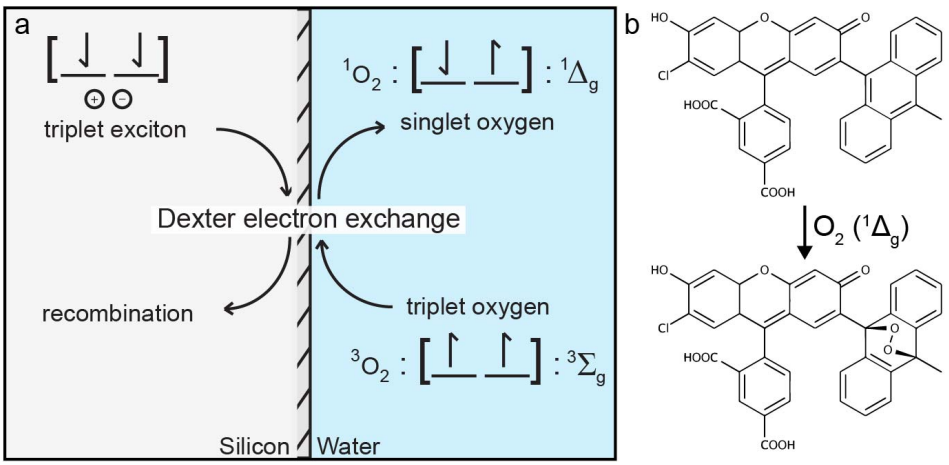

Figure 2.10: (a) Silicon-water interface diagram showing the transfer of electrons from surface excitons in silicon to dissolved oxygen molecules. (b) Structure of SOSG before reaction with singlet oxygen and its associated endoperoxide (SOSG-EP) after reaction with singlet oxygen.

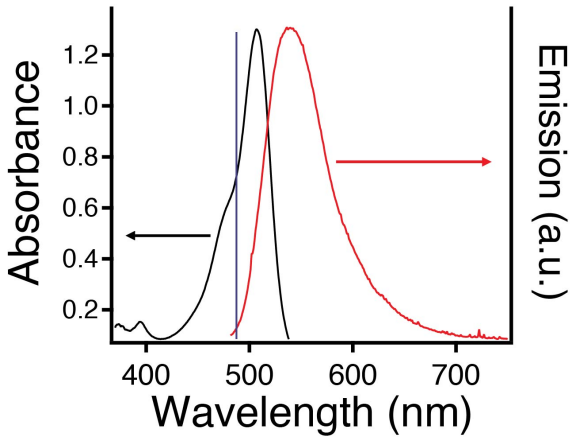

Figure 2.11: Absorption (black) and emission (red) spectra for SOSG-EP; the blue vertical line represents the 2-photon wavelength for a 975 nm trapping source.

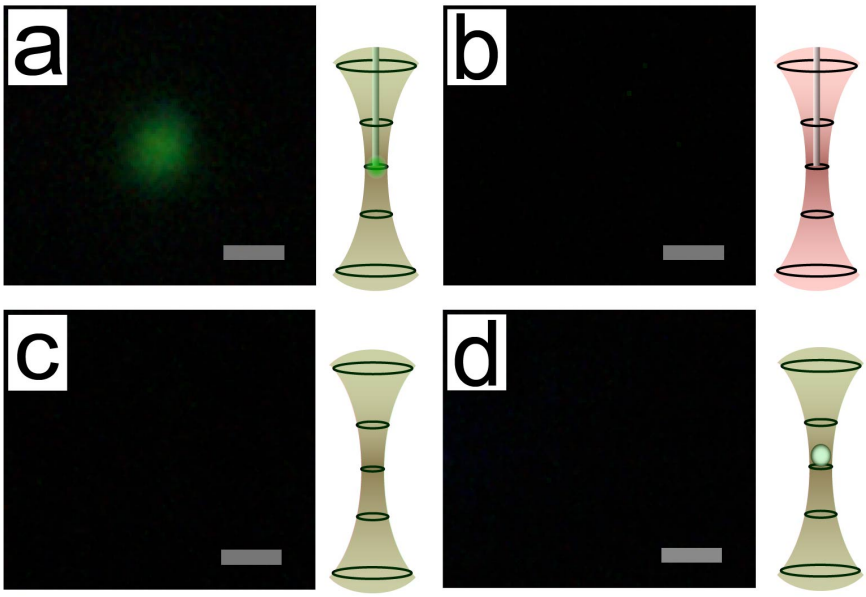

Figure 2.12: Singlet-oxygen ($^1O_2$) generation from silicon nanowires. Digital micrographs of (a) a single optically trapped silicon nanowire in SOSG solution, (b) a single optically trapped silicon nanowire in water alone, (c) illumination of a chamber of SOSG solution, and (d) a single optically trapped silica bead in a solution of SOSG.

2.12a). The potential for visible photoluminescence from the porous SiNWs was eliminated as a possible source of emission by performing an identical control experiment with optically trapped SiNWs in the absence of SOSG (Figure 2.12b). It also has been demonstrated recently that there is negligible ($< 5°C$) photothermal heating of optically-trapped SiNWs via analysis of their Brownian dynamics [25].

Generation of singlet oxygen directly from SOSG has been reported previously [61] using UV or visible irradiation. An additional control experiment was performed to test for potential photogeneration of $^1O_2$ from SOSG molecules themselves at an identical NIR irradiance (Figure 2.12c). Clearly, the NIR source is unable to excite $^1O_2$ directly or through photosensitization of the SOSG molecule. Similarly, a final control experiment combining SOSG and SiO_2 microspheres (Figure 2.12d) exhibit no detectable $^1O_2$ generation at the bead's fully oxidized surface which is expected since SiO_2 is an insulator and would not generate

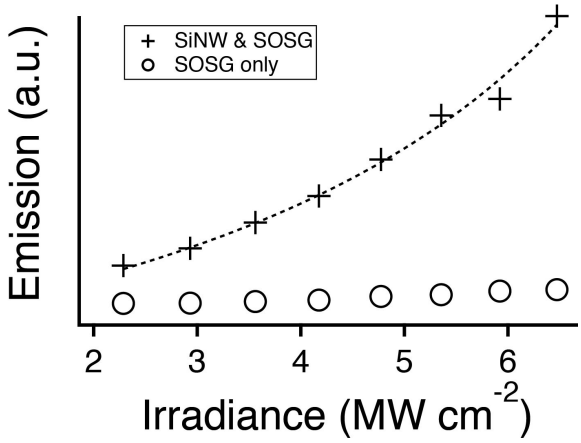

Figure 2.13: SOSG-EP emission from a single trapped SiNW as a function of 975 nm laser irradiance, demonstrating the nonlinearity of SOSG-EP excitation.

the excitons necessary to sensitize $^1O_2$. A quadratic dependence on the integrated emission from SOSG as a function of laser power is observed (Figure 2.13), indicating that SOSG is excited by a two-photon mechanism.

Enhanced singlet oxygen generation within a suspension of SiNWs is also observed at much lower laser irradiance. A cuvette with a concentrated suspension of SiNWs and SOSG was placed in the path of the 975 nm laser beam at an irradiance of 8 W/cm^2 (beam power = 260 mW, spot size = 2 mm) and removed at regular intervals to monitor the change in SOSG-EP concentration under 405 nm excitation. Comparison with a cuvette containing SOSG alone shows a significant increase in $^1O_2$ production (Figure 2.14). The approach demonstrated above for analyzing single silicon nanowires may also be extended to other nanoscale materials including noble metals. Gold nanocrystals have been shown to induce significant photothermal super-heating of water when optically trapped [26] and several recent reports have indicated that noble metal nanoparticles are capable of photogeneration of singlet oxygen [53, 54, 57]. In Figure 2.15 we show that it is possible to observe the generation of singlet oxygen from single gold nanorods that have been synthesized through electrochemical deposition within track-etched polycarbonate membranes. To confirm that

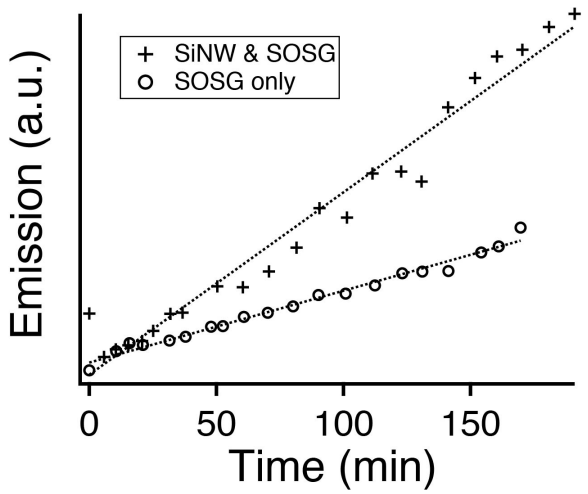

Figure 2.14: Comparison between a solution of SiNWs & SOSG and a solution of only SOSG. Both solutions were irradiated by a 975 nm laser at equal powers and, at each data point, were illuminated with a 405 nm diode to obtain the momentary emission spectrum from generated SOSG-EP. The data demonstrate an enhanced generation of singlet oxygen when SiNWs are present.

the observed emission is from SOSG-EP and not 2PPL from the AuNRs, a single AuNR was trapped without SOSG (Figure 2.15c) and long exposure micrographs showed no observable emission (Figure 2.15d).

We have demonstrated that a near-infrared laser trap can be used to observe the photogeneration of $^1O_2$ molecules from individual silicon and gold nanowires that are suspended within an aqueous trapping medium. To our knowledge, there have been no prior reports of observing the photosensitization of $^1O_2$ at the level of single nanostructures. Although the optical absorption coefficient of silicon at NIR wavelengths is not as high as for visible wavelengths, the use of NIR radiation allows for deeper tissue penetration. Furthermore, this work suggests that singlet-oxygen may also be generated during photothermal heating of gold and semiconductor nanostructures, including recently reported [62, 63] silicon/gold composite nanostructures that have been investigated for in vivo solid tumor photothermal ablation. The NIR generation of $^1O_2$ from silicon nanowires may also affect the long-term

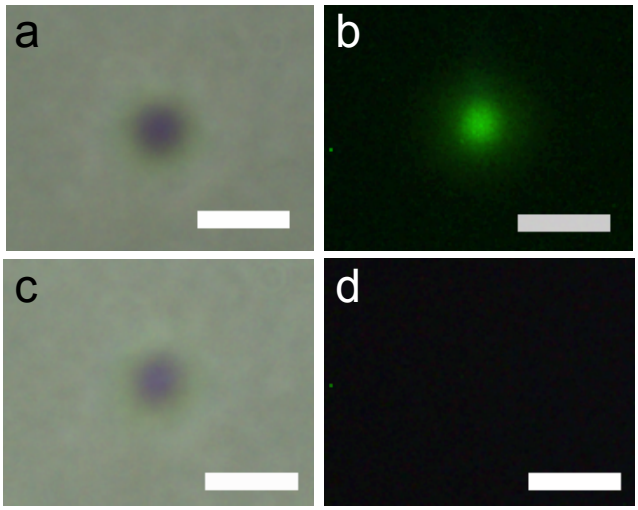

Figure 2.15: Singlet-oxygen ($^1O_2$) generation from a single optically-trapped gold nanowire. (a) Bright field micrograph of an electrochemically synthesized gold nanorod (AuNR) optically trapped in a solution of SOSG using the same setup used for SiNWs, diagrammed in Figure 2.9a. (b) Micrograph of the SOSG-EP emission from the AuNR trapped in (a). (c) Micrograph of an optically trapped AuNR in water alone. (d) Micrograph of the AuNR in (c) demonstrating no emission in the absence of SOSG. All scale bars = 2 μm.

stability of catalysts used for solar energy conversion through adverse, photo-induced corrosion[64]. Future studies will investigate how the efficiency of $^1O_2$ generation is affected by size-dependent morphology-dependent-resonances [52].

Chapter 3

NONLINEAR OPTICAL PHENOMENA

After completing my experiments on singlet oxygen generation from SiNWs, our group was invited to submit an original research article relating to Professor Pauzauskie's previous publication in Nature demonstrating a tunable nonlinear probe in a LT [65]. As a young group, the easiest choice was to begin experiments with a familiar material that was simple to synthesize: $KNbO_3$ nanowires (KNNWs). At this point, my interest in laser spectroscopies pushed me to lead the experiments and explore nonlinear optics within our system. By co-aligning all 3 of the existing NIR lasers into the trapping objective, sum frequency generation could be observed in addition to harmonic generation of a single beam. Through the use of a tunable NIR laser, we were able to demonstrate Fabry-Pérot resonances within a single KNNW and the previously discussed methods for temperature extraction show that increased heating of trapped KNNWs relative to solvent background absorption occurs as result of lattice defects.

3.1 Introduction to Nonlinear Optics

The nonlinear response of materials to intense electric fields were only realized after the advent of the laser. The first reported example was second harmonic generation (SHG) of a ruby laser in crystalline quartz [66]. Since then researchers in the field of nonlinear optics have demonstrated harmonics as high as $n = 221$ [67]. Harmonic generation has a significant utility in converting lasers beams of frequency ω into beams with frequency of $n\omega$ where n is an integer. Other commonly used nonlinear effects include parametric processes such as sum frequency generation (SFG), difference frequency generation (DFG), and optical parametric oscillation (OPO), or non-parametric processes like two-photon absorption (TPA)

and stimulated Raman scattering [68]. Applications of nonlinear processes vary significantly and include laser frequency modulation [66, 69], two-photon luminescence [70], vibrational spectroscopy [71], two-photon medical imaging [72], nonlinear photodynamic therapy [55, 73], and information technology [74].

3.2 Nonlinear reponse of $KNbO_3$ nanowires in an optical trap

Nanostructures have gained in popularity as nonlinear optical materials [75–79], notably for biomedical theranostics [80]. Applications include drug delivery [81], photothermal [82] and photodynamic [83, 84] therapy, and imaging [85]. Nonlinear nanoparticles are especially advantageous for biomedical imaging [86] as they allow for the use of near infrared (NIR) light which penetrates deeper into living tissue than visible light due to lower absorption [87]. One-dimensional structures have the advantage of a large surface area providing a scaffold for adsorption and conjugation. Potassium niobate is a popular nonlinear material [88] and has even had nonlinear effects demonstrated from optically trapped nanowires [65]. However, knowing the temperature of $KNbO_3$ nanomaterials under NIR illumination is important not only for phase-matching conditions but also if it is to be used in vivo for theranostic applications given the low temperature threshold ($\sim$42°C [89]) for cellular damage. Here, the Brownian dynamics of optically trapped KNNWs are analyzed in order to extract temperatures. Nonlinear processes, including SHG and SFG, are observed from the trapped KNNWs and Fabry-Pérot type cavity enhanced SHG is demonstrated using a tunable NIR laser which suggests the possibility of synthetically tuning the lengths and diameters of nanowire cavities for increased harmonic conversion [76–78].

Monoclinic $KNbO_3$ nanowires were grown hydrothermally using a previously-reported method [90]. Briefly, 12.6 g of KOH was dissolved in 15 mL DI H_2O and sonicated for 5 minutes. After adding 0.87 g of niobium metal powder to this solution it was placed into a teflon-lined autoclave and heated to 150°C for 15 hours. The crystal structure of the as-synthesized KNNWs was determined using characterization techniques including: SAED, XRD, Raman spectroscopy, and scanning transmission x-ray microscopy.

Samples for scanning electron microscopy (SEM), x-ray diffraction (XRD), and Raman spectroscopy were prepared by evaporating an aqueous suspension onto a clean silicon wafer. Scanning electron micrographs were acquired on a JEOL JSM-7000F scanning electron microscope in secondary electron imaging mode with a 10.0 kV accelerating voltage and 10.0 mm working distance. Bright-field TEM and select area electron diffraction (SAED) images were taken on a FEI Tecnai G2 F20 at an accelarating voltage of 200 keV. SAED images were taken with a camera length of 490 mm. XRD measurements were performed on a Bruker D8 Discover with GADDS XRD system using Cu K_α radiation. Raman spectra were obtained using a home-built setup using a Coherent Compass 532 nm SLM laser at 10 mW power. The laser was focused onto the sample using a Mitutoyo 50x long working distance objective (NA=0.55). Backscattered light was dispersed onto a Princeton liquid nitrogen-cooled silicon CCD using an Acton 500i SpectraPro spectrograph.

Near-edge X-ray absorption fine structure (NEXAFS) spectroscopy was perfomed on the Advanced Light Source beamline 5.3.2.2 at Lawrence Berkeley National Laboratory. Samples were prepared by evaporating a 2μL suspension of nanowires onto a lacey carbon TEM grid and placing the TEM in the beamline under 0.33 atmospheres of helium. Soft x-rays (250 - 800 eV) were focused onto the sample with a spot size of 31 nm using 25 nm Fresnel zone plates. The oxygen K-edge was observed in the energy window of 525 - 550 eV.

Optical trapping of individual KNNWs was accomplished with a home-built system (Fig. 3.3). A 330 mW Thorlabs 975 nm diode laser, 4 W SpectraPhysics 1064 nm diode-pumped solid-state laser, and 10 W Sahajanand Laser Technology 1020-1040 nm tunable DPSS Yb:YAG disk laser were co-aligned, expanded, and focused into a chamber using a Nikon 100x oil immersion objective (NA=1.25). SHG and SFG signals were collected using the same objective and detected with the same spectrometer used for the Raman measurements. Trapping chambers consisted of 75x25x1 mm glass slide and #1 coverslip with a droplet of NW suspension and imaging spacer (Grace Bio-Labs) confined between them.

The crystal structure of the KNNWs synthesized by the hydrothermal method has been characterized extensively [90] and the current results support a monoclinic phase. SEM

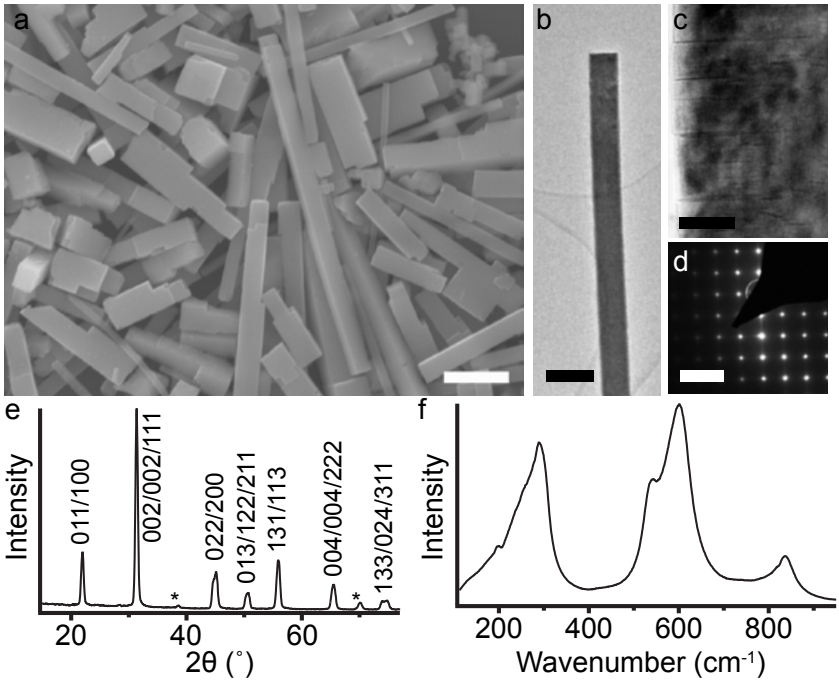

Figure 3.1: Characterization of hydrothermally grown nanowires. a) Scanning electron micrograph of KNNWs demonstrating square cross-sections. Scalebar = 500 nm. b) Transmission electron micrograph of a single KNNW. Scalebar = 300 nm. c) Higher magnification of KNNW in b to show extended planar defects in a KNNW. Scalebar = 30 nm. d) Select area electron diffraction pattern of the KNNW in b. Scalebar = 5 nm^{-1} e) X-ray diffraction of a $KNbO_3$ powder sample with crystal planes indicated. Asterisk denotes peaks not associated with $KNbO_3$ and are likely from Nb metal precursor. f) Raman scattering from a $KNbO_3$ powder sample.

images clearly show the orthogonal cross sections of KNNWs signifying highly crystalline growth (Fig. 3.1a) with an average edge length measuring 152 ± 49 nm, which lies below the single-mode waveguide cutoff for 975 nm in $KNbO_3$: 229 nm. However, the inhomogeneous contrast found in the bright field TEM image of an individual KNNW (Fig. 3.1b) indicates a significant amount of extended crystallographic defects (Fig. 3.1c) including stacking faults and twinning planes. The corresponding SAED pattern (Fig. 3.1d) confirms a monoclinic phase with a [100] growth direction. Streaking can also be seen in the SAED pattern which agrees with stacking faults observed in brightfield micrographs. X-ray diffraction (Fig. 3.1e)

and Raman spectra (Fig. 3.1f) also support a monoclinic phase. Weak signals can be seen in the XRD plot at 38° and 70° which are not attributable to $KNbO_3$ and are likely from residual Nb metal precursor. However, analysis of these peaks using the Scherrer equation [91] gives a particle size > 15 nm which are not observed in TEM brightfield images or SAED patterns from individual KNNWs, meaning there is no Nb metal within the KNNWs themselves. Since 1-dimensional $KNbO_3$ structures are easily identified optically during laser trapping experiments, Nb precursor material can be excluded as a contributing factor for heating of trapped KNNWs.

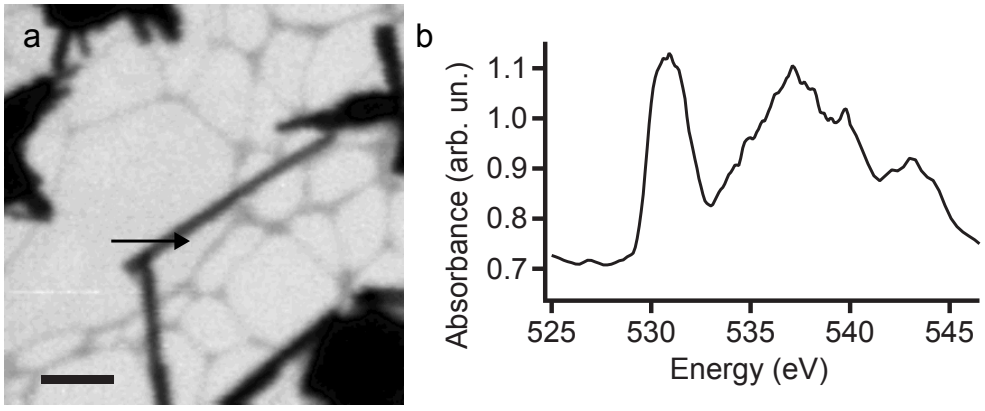

Figure 3.2: (a) Scanning transmission x-ray micrograph of KNNWs suspended on a lacey carbon TEM grid. The arrow indicates the line drawn with the linescan used to determine the spectrum in panel (b). X-ray energy for the micrograph is 540 eV. Scalebar = 1 μm. (b) Near edge X-ray absorption fine structure (NEXAFS) of the O K-edge from the monoclinic KNNW linescan in (a) demonstrating the effect of hybridization of the O 2p orbitals with the Nb orbitals.

The chemical bonding environment surrounding the niobate ion can be probed with scanning transmission x-ray microscopy (STXM). A suspended KNNW was imaged using STXM (Fig. 3.2a) and a linescan of the nanowire was used to extract an x-ray absorption spectroscopy (XAS) profile in the energy range of 520 - 580 eV. Observation of the O K-edge at 530 eV shows a slight deviation from the simple O 1s $\rightarrow$ O np transition. The XAS profile of $KNbO_3$ has been explained previously [92] through the hybridization of O 2p and with

several different Nb orbitals including 4d (t_{2g}), 4d (e_g), 5s, and 5p. The spectrum measured from our material (Fig. 3.2b) matches well with the previous report well.

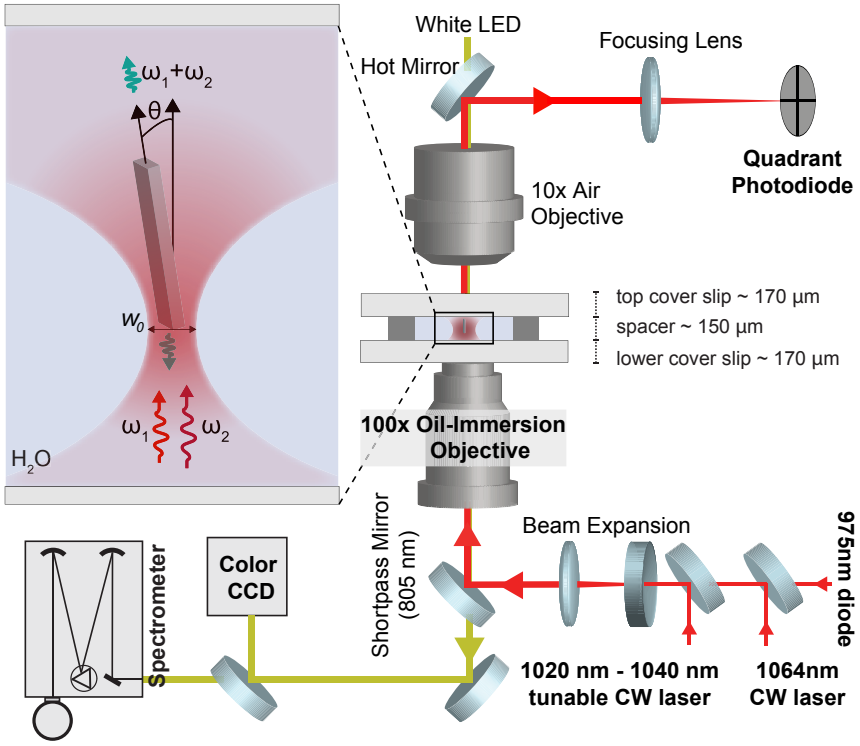

Figure 3.3: Schematic of the experimental optical trapping setup used for nonlinear optical studies of $KNbO_3$ nanowires.

The electric fields generated within an optically-trapped KNNW is of sufficient intensity that the material will respond nonlinearly, described by the second-order polarization:

$$\mathbf{P}(t) = \epsilon_0 \chi^{(2)} \mathbf{E}^2(t). \tag{3.1}$$

Here ϵ_0 is the permittivity of free space, $\chi^{(2)}$ is the second-order nonlinear susceptibility, and $\mathbf{E}(t)$ is the electric field. Gases, liquids, amorphous solids, and many crystal structures display inversion symmetry and, therefore, have a vanishing $\chi^{(2)}$. $KNbO_3$, however, is a non-centrosymmetric crystal which will demonstrate second-order nonlinear effects. If a field

consisting of two frequency components (ω_1, ω_2), expressed as

$$\mathbf{E}(t) = \mathbf{E}_1 \cos(\omega_1 t - kx) + \mathbf{E}_2 \cos(\omega_2 t - kx), \tag{3.2}$$

is incident on a nonlinear material, it can be seen that, following Eq. 3.1, the resultant fields will include second harmonic frequencies ($2\omega_1$, $2\omega_2$), the sum frequency ($\omega_1 + \omega_2$), and the difference frequency ($\omega_1 - \omega_2$). In the current experiment, co-aligned lasers of different frequencies are used to demonstrate simultaneous SHG and SFG in trapped KNNWs. In one experiment the 975 and 1064 nm lasers were used to trap the same NW producing their respective second harmonic signals at 487.5 and 532 nm in addition to the sum frequency signal at 509 nm (Fig. 3.4a). Figure 3.4b shows the potential of tunable SFG from an optically trapped KNNW. Eleven spectra are overlaid with each spectrum showing SHG from the 1064 nm laser, SHG from the NIR tunable laser set to a particular wavelength, and the SFG signal from the tuned and 1064 lasers. It can be inferred from these observations that there is also radiation generated at wavelengths corresponding to the difference frequencies: 11.7 μm (106 meV), the difference between 1064 nm + 975 nm and 24.7 - 46.1 μm (27 - 50 meV), the difference between the tunable NIR laser + 1064 nm. However, the estimated power for SHG and SFG signals, accounting for grating and detector efficiencies, is 10^{-14} W and, assuming a similar efficiency for DFG, the mid-infrared powers would be over an order of magnitude less than visible powers. Even with water's high absorption in the mid-infrared, solvent heating due to DFG is unlikely due to neglible powers generated. Figure 3.4c shows the relative intensities of SHG polarized parallel and perpendicular to the 1064 nm fundamental beam. The ratio of polarization for SHG ($\sim$10) indicates that the visible luminescence from a trapped KNNW is able to maintain a significant amount of coherence which could be beneficial for applications where lasing is required on a micro- and nano-scale.

Optical trapping of a single nanostructure with parallel end facets also permits the observation of Fabry-Pérot resonances (Fig. 3.5), depending on the particle geometry and wavelength of light. In this case, the second harmonic of the tunable laser lies in the range

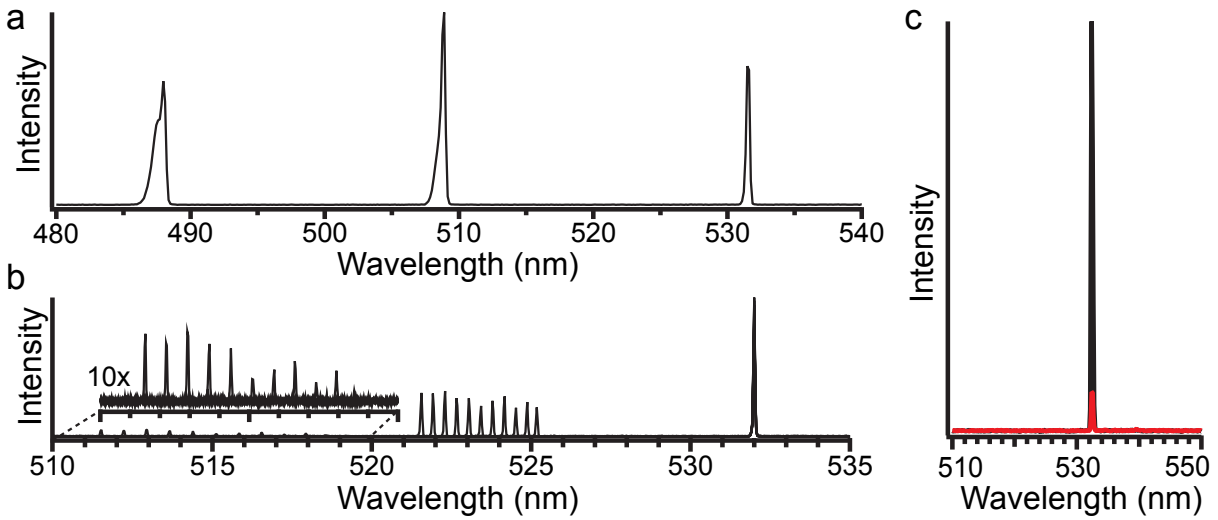

Figure 3.4: Sum frequency generation. a) Sum frequency generation from a KNNW using co-aligned 975 and 1064 nm lasers. b) Tunable sum frequency generation from a KNNW using a co-aligned 1064 nm DPSS laser and a tunable 1020-1040 nm DPSS laser. c) SHG of 1064 nm fundamental laser with polarizer parallel (black) and perpendicular (red) to the fundamental polarization.

510 - 520 nm while the cavity length is approximately 4 micrometers. The mode spacing is expressed [93]:

$$\Delta\lambda = \frac{\lambda^2}{4L[\lambda\frac{\partial n}{\partial\lambda} - n]} \tag{3.3}$$

where λ is the wavelength, n is the refractive index of the material, $\partial n/\partial\lambda$ is the dispersion of the refractive index, and L is the length of the NW. Using reported [94] values for the optical properties of $KNbO_3$, the predicted mode spacing is 6.5 nm which matches well with the experimental value of 5.8 nm. The width of the SHG signal can also be used to comment on the quality factor, Q, of the KNNW based on the formula $Q = \omega_0/\delta\omega$, giving a value of $\sim$80.

Temperatures of particles within an optical trap are often ignored based on assumptions of neglible absorption. But the significant temperature dependence of phase-matching for nonlinear materials requires a better understanding of the heat generated in these materials

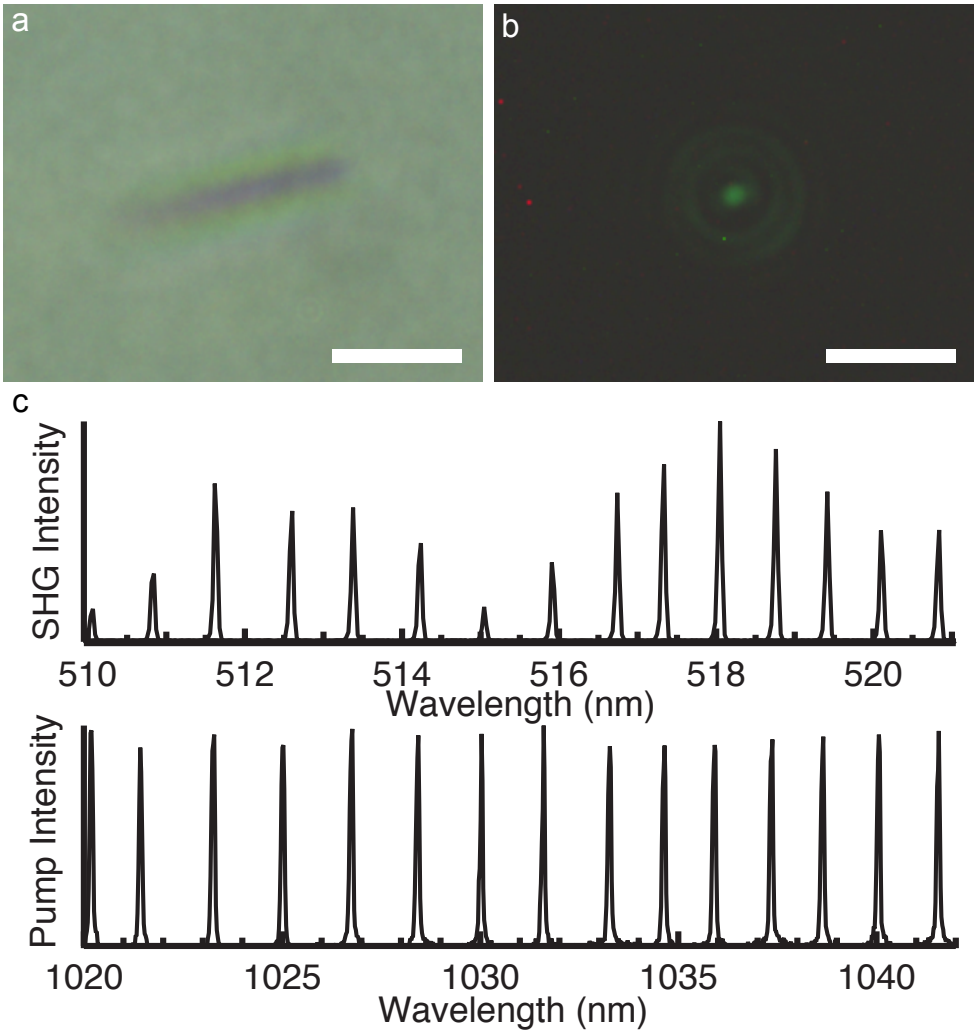

Figure 3.5: (a) Bright field image of a KNNW in Brownian motion. Scale bar = 2 μm. (b) Long-exposure, dark image demonstrating SHG from the KNNW while trapped with a 1030 nm source. Scale bar = 2 μm. (c) A NIR tunable laser was tuned from 1020 to 1040 nm while maintaining a constant trapping power (lower panel). The second harmonic generation from a KNNW was detected at each discrete pump wavelength (upper panel). The oscillations with the SHG are due to a Fabry-Pérot resonance within the NW.

under intense illumination. It has been demonstrated that back focal plane interferometry of forward-scattered laser light can be used to monitor the Brownian motion of a trapped NW. [25] In these experiments the forward-scattered laser light is collected and focused onto a quadrant photodiode where the voltage-to-displacement calibration factor is found using a piezo-oscillation method [23]. Once the calibration factor is determined the experimental diffusion coefficient can be found by fitting the calibrated QPD power spectrum [21]. The temperature of the trapped NW can then be determined by equating the experimental diffusion coefficient to the hot Brownian motion diffusion coefficient of a heated particle in a locally non-isothermal environment [95, 96] and solving for the particle's temperature. Temperatures of trapped KNNWs were found using this method and are compared to temperatures of SiO_2 beads at identical trapping powers in Fig. 3.6. The bandgap of $KNbO_3$ lies in the ultraviolet region of the spectrum [97] so one would expect little one- or two-photon absorption from the NIR wavelengths used to trap the NW. However, crystal defects can enhance optical absorption within the lattice resulting in heat generation. [98] The inhomogeneous contrast seen in the KNNW bright-field TEM micrograph (Fig. 3.1b and c) indicates lattice distortion which is further supported by the SAED pattern where the faint linear streaks between spots characteristic of large numbers of extended crystallographic defects. Experimental temperatures can be used in conjunction with recent theory [25] for heating of finite cylinders in order to estimate the imaginary refractive index, k of a trapped KNNW. By assuming a circular cylinder with a length of 4.12 μm (Fig. 3.5a) and diameter equal to the edge length of the KNNW square cross section (150 nm), it is found that $k \approx 0.0005$, which corresponds to an equivalent absorption coefficient of $\alpha \approx 60cm^{-1}$.

We have demonstrated that the use of a tunable, 1020-1040 nm, continuous-wave NIR trapping source with hydrothermally synthesized potassium niobate nanowires provides tunable second harmonic generation which can then be used to demonstrate cavity-enhanced emission through Fabry-Pérot resonances. Additionally, the range of tunability of the nonlinear emission in the visible region can be extended by introducing a second, co-aligned NIR laser source resulting in sum frequency generation. Given the potential for application

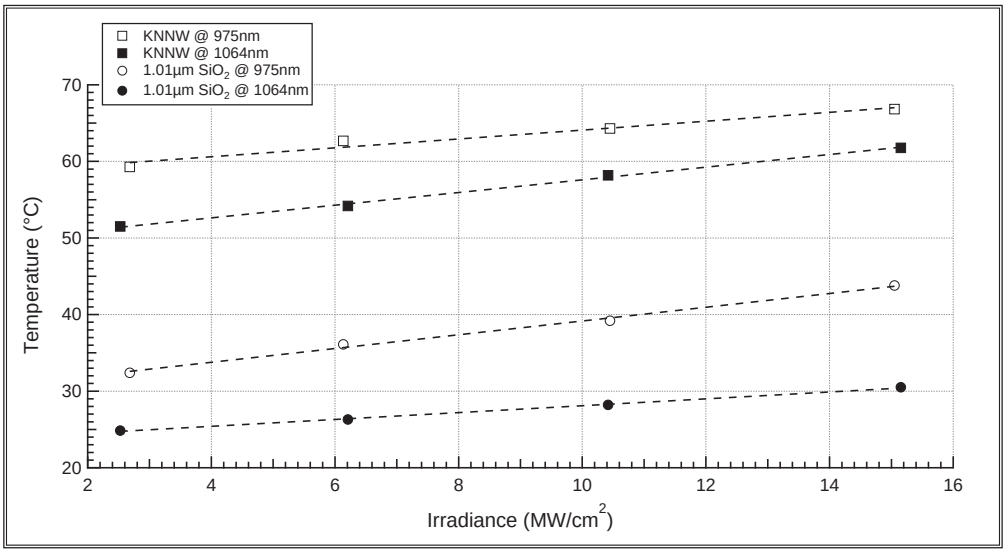

Figure 3.6: Temperatures of trapped KNNWs (squares) and SiO_2 beads (circles) using a 975 nm laser diode (open) or 1064 nm DPSS laser (closed) measured using Brownian analysis of forward-scattered laser light.

of these nonlinear materials in theranostic nanomedicine, the heat generated by nanoscale particles in the intense fields necessary for nonlinear effects could have a significant impact. Temperature measurement through analysis of particle Brownian motion shows an increase from room temperature to ∼60°C at an irradiance of approximately 10 MW/cm^2 which we attribute to crystallographic defects evidenced in the contrast from bright field TEM and SAED patterns. Future efforts could exploit the narrow linewidth and tunability of the visible SHG from individual KNNWs, for example, to selectively pump narrowband absorbers like rare-earths or photosensitizers for photodynamic therapy.

Chapter 4

RAMAN SPECTROSCOPY

Raman scattering from molecules and solids was predicted in 1923 by German, theoretical physicist A. Smekal [99], and experimentally reported by C. V. Raman (quelle coïncidence!) and K. S. Krishnan in India in 1928 [100, 101]. Since then, Raman spectroscopy has become a common laboratory technique for applications ranging from routine compound identification to cutting edge research. It is often used in a complimentary manner to infrared (IR) spectroscopy in that it provides the ability to probe molecular vibrations that would otherwise be unobservable through IR techniques. The differences are a result of the distinct selections rules, where direct vibrational transitions require a change in dipole moment, μ, with the vibration [102]. Mathematically, this is written as

$$[\mu]_{\nu_0,\nu_1} = \int \psi^*_{\nu_0}(Q)\mu\psi_{\nu_1}(Q)dQ, \tag{4.1}$$

where ν_0 and ν_1 are the ground and excited vibrational states, respectively, ψ is the eigenfunction of the vibrational quantum state, and Q is the normal coordinate for the vibration. For Raman scattering, the polarizability, α, must transform with the vibration, or

$$[\alpha]_{\nu_0,\nu_1} = \int \psi^*_{\nu_0}(Q)\alpha\psi_{\nu_1}(Q)dQ. \tag{4.2}$$

A vibration is considered IR-active if the integral in Eq. 4.1 is non-zero. It will be Raman-active if Eq. 4.2 is non-zero. While the two methods are not mutually exclusive for a particular vibration, many normal vibrations are transparent to IR absorption due to its selection rule. Additionally, solid-state materials, which have been the main focus of the group, can be a challenge for IR sample preparations. Whereas Raman spectroscopy is amenable to

studies of the solid phase and a system can be assembled with a single, high-quality laser, a few optics, and a spectrometer. Our group was lucky enough to have had a functioning spectrograph and liquid nitrogen-cooled CCD donated for our research. All that remained was the laser and optics. And considering my interest in studying laser refrigeration of CdS nanoribbons, we selected a 532 nm source with associated optics. Since its assembly, our Raman setup has been extremely beneficial to each of the members of the group for a wide variety of experiments.

4.1 Theory of Raman Spectroscopy

As implied previously, the origin of Raman spectra is the interaction of the incident electromagnetic field with vibrational (or rotational) quantum levels. If we consider the light wave to have an electric field strength of E and frequency ν, this can be expressed

$$E = E_0 \cos 2\pi\nu t \tag{4.3}$$

where E_0 is the amplitude and t is the time. If a molecule is illuminated by the EM wave, the resulting dipole, P, is related to the electric field through the polarizability, α, and described by

$$P = \alpha E = \alpha E_0 \cos 2\pi\nu t. \tag{4.4}$$

For a molecule vibrating with frequency ν_i, the nuclear displacement, q, can be written as

$$q = q_0 \cos 2\pi\nu_i t \tag{4.5}$$

where q_0 is the vibrational amplitude. For small amplitudes of vibration, the polarizability is a linear function of q, that is

$$\alpha = \alpha_0 + \left(\frac{\partial\alpha}{\partial q}\right)_0 q. \tag{4.6}$$

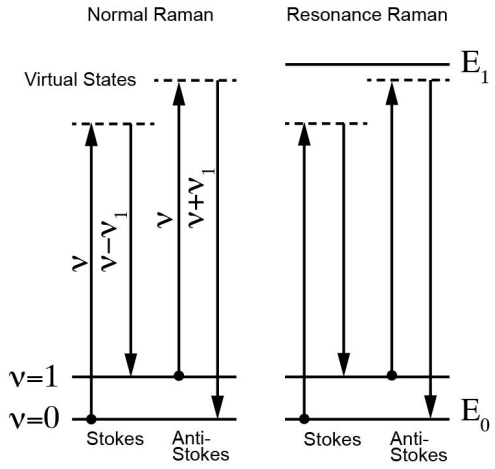

Figure 4.1: Diagrams representing the mechanisms in normal Raman (left) and resonance Raman transitions.

Here, α_0 is polarizability of the unperturbed molecule and $\left(\frac{\partial\alpha}{\partial q}\right)_0$ is the polarizability's rate of change with respect to nuclear displacement, taken at the equilibrium position. If the preceding equations are combined, we can see that the following relations are produced

$$P = \alpha E_0 \cos 2\pi\nu t \tag{4.7}$$

$$= \alpha_0 E_0 \cos 2\pi\nu t + \left(\frac{\partial\alpha}{\partial q}\right)_0 q_0 E_0 \cos 2\pi\nu t \cos 2\pi\nu_i t \tag{4.8}$$

$$= \alpha_0 E_0 \cos 2\pi\nu t + \frac{1}{2}\left(\frac{\partial\alpha}{\partial q}\right)_0 q_0 E_0[\cos(2\pi(\nu+\nu_i)t) + \cos(2\pi(\nu-\nu_i)t)]. \tag{4.9}$$

Looking at Eq. 4.9, the first term on the right-hand side represents the Rayleigh scattering, the second term $(\nu+\nu_i)$ represents the anti-Stokes scattering and the third $(\nu-\nu_i)$ represents the Stokes scattering. These processes are represented schematically in the left panel of Fig. 4.1. The right panel represents resonance Raman in which the Raman scattering of a Raman-active vibrational mode can be enhanced by the existance of electronic states near the virtual state produced by the excitation laser. The inclusion of this diagram is particularly relevant for the case of CdS under a 532 nm excitation. The energy of a photon from a 532 nm laser

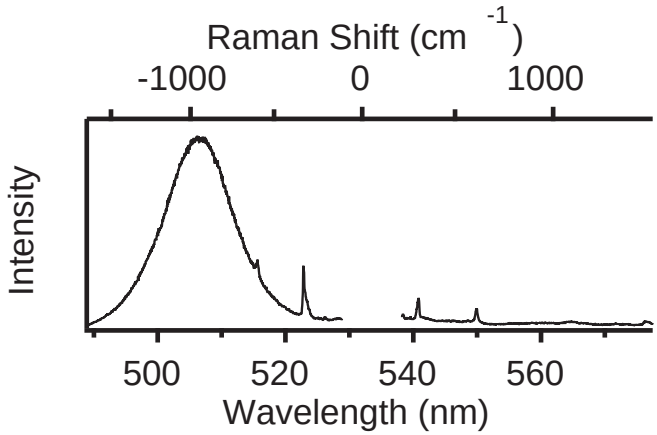

Figure 4.2: Raman scattering and anti-Stokes photoluminescence of a CdS nanoribbon demonstrating the strong anti-Stokes Raman lines as a result of resonance with the CdS bandgap.

(2.33 eV) lies just below the band gap of CdS (2.42 eV) such that the annihilation of lattice phonons to produce anti-Stokes scattering will generate photons that are more resonant (i.e. closer in energy) with the bandgap (Fig. 4.2).

Following the demonstration of singlet oxygen generation from SiNWs in a LT, it was of interest to probe the existence of the $^1O_2$ species by using our Raman system to excite carriers in a silicon substrate to sensitize the O_2 molecules and subsequently observe red-shifted scattering unique from the ground state vibrational mode [103]. The experimental setup consisted of a Si chip mounted in a Janis ST-500 cryostat, initially pumped down to pressures below 10^{-7} mbar, and cooled to 76 K. Once the sample had reached 76 K, bursts of oxygen were introduced into the cryostat with the aim of condensing the O_2 molecules on the Si surface since the boiling point of oxygen is 90 K. The cycling of O_2 flow was continued until there was a detectable O_2 Raman signal at the surface of the Si. Unfortunately, the goal of exciting O_2 molecules to the $^1\Delta$ state and observing their unique vibrational mode was not accomplished, likely as a result of photothermally heating the substrate and re-evaporating the adsorbed molecules. However, as a result of the measurement, we were able to observe the O, Q, and S branches from the rotational-vibrational Raman spectrum of unadsorbed

O_2 molecules (Fig. 4.3).

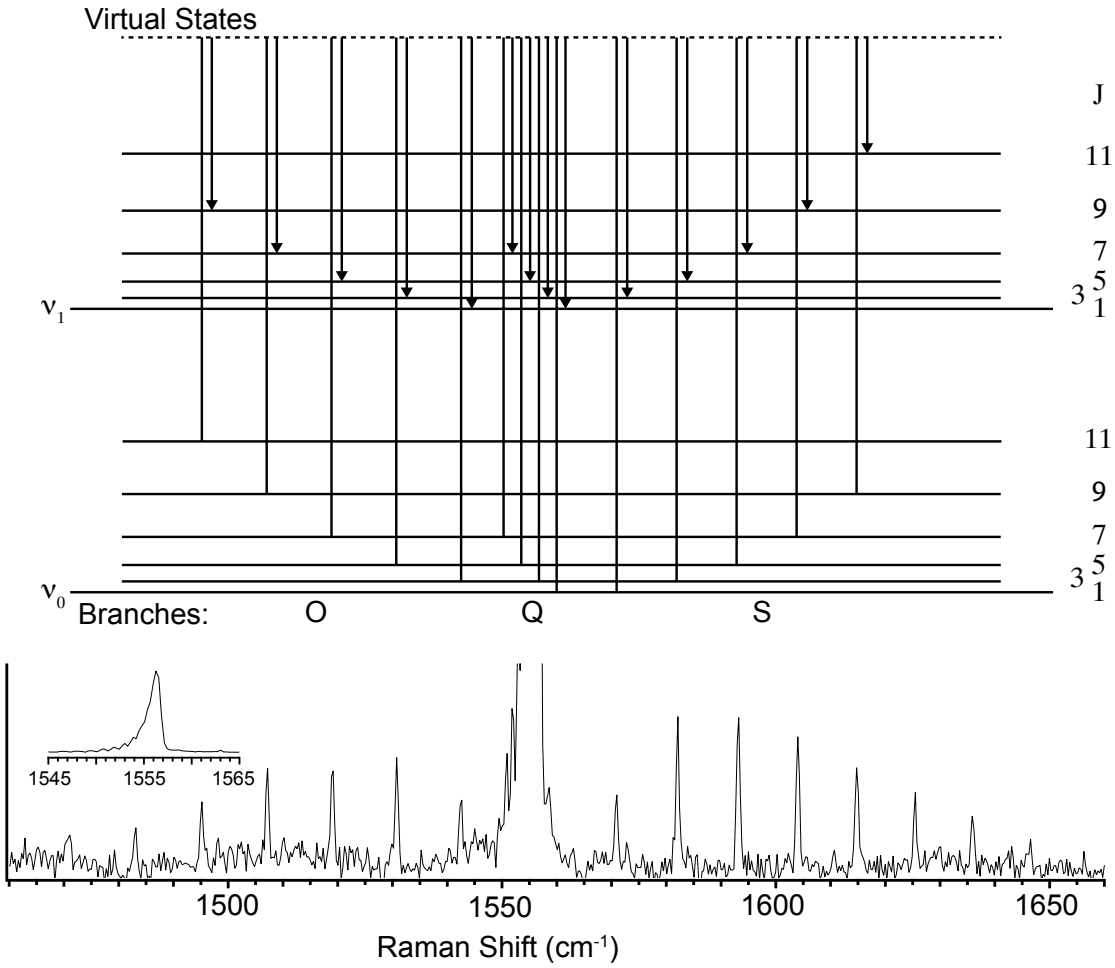

Figure 4.3: Energy level diagram depicting the transitions between the ground and lowest vibrational quantum state and associated rotational states for a ground ($^3\Sigma$) state O_2 molecule and the experimentally observed rotational-vibrational Raman spectrum.

Selection rules for diatomic molecules state that for vibrational transitions

$$\Delta\nu = \pm 1 \tag{4.10}$$

and for rotational transitions

$$\Delta J = 0,\ \pm 2. \tag{4.11}$$

Additionally, for molecules with a non-singlet electronic state there is coupling between the rotational angular momentum of the molecule and the electronic spin [104]. The end result for the case of the O_2^{16} $^3\Sigma$ ground electronic state is that the rotational levels $J = 0, 2, 4, ...$ do not exist. Looking at the experimental data, we can see rotational states in the S branch as high as 17 and the data match earlier reports well [105].

4.2 High Pressure Phase Transitions of Silicon Nanowires

Silicon is the second most abundant element in the Earth's crust [106] and the foundation of the modern electronics industry. It is used for integrated circuits in information technology and as an energy conversion material in photovoltaics. Unfortunately, one of the biggest drawbacks for silicon's use in solar energy conversion is its indirect band gap. Theoretical [107, 108] and experimental [109–111] efforts are looking at the properties of exotic phases of silicon and their potential as improved photovoltaic (PV) absorbers.

The phase diagram of silicon [112] reveals several polytypes at elevated pressures. At a pressure of ∼11 GPa, Si-I begins to transition to Si-II which has a body-centered tetragonal crystal structure and metallic electronic structure [113]. As pressure increases past approximately 15 GPa, Si-V begins to emerge with a primitive hexagonal phase [114–116]. But neither Si-II nor Si-V are stable at atmospheric pressure and, therefore, have not been observed experimentally outside of high pressures. Si-III (body-centered cubic) and Si-IV (diamond hexagonal), however, are stable at atmospheric pressure and have been synthetisized [109, 117] as well as recovered from high-pressure phase transitions [118–120]. While Si-III is a semimetal [118] and could have applications in electronics, Si-IV is a semiconductor with a reported indirect band gap near 0.8-0.9 eV and direct transition at 1.5 eV [117]. The direct transition for Si-IV makes it appealing for PV applications due to higher absorption efficiency in the visible spectrum.

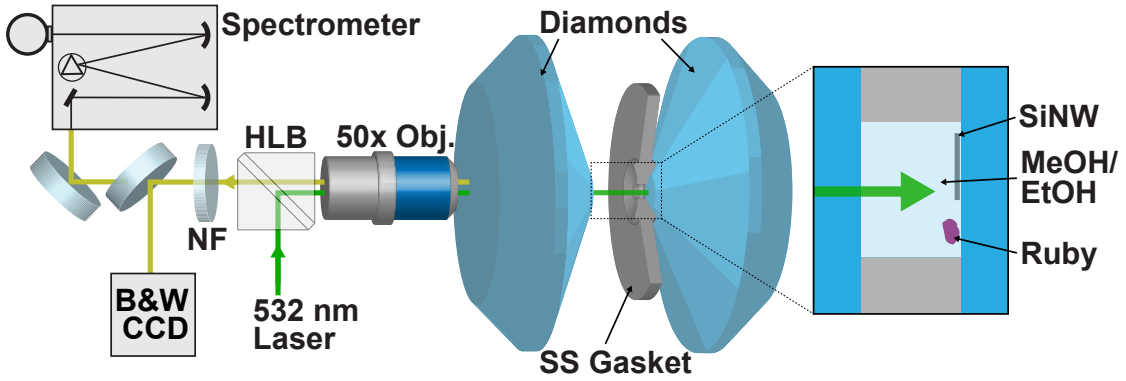

Figure 4.4: Schematic of the diamond anvil cell (DAC) and components for Raman scattering measurements. A holographic laser bandpass (HLB) filter is used to pass the 532 nm Raman probe into a 50x objective which focused the beam into DAC. Nanowire Raman scattering and ruby photoluminescence were collected with the same objective and sent to a spectrometer or CCD for imaging. A 532 nm notch filter (NF) was used to eliminate strong Rayleigh scattering.

Nano-structured silicon can also prove advantageous for light-absorbing materials. For example, periodic dielectric structures, including photonic crystals (PC), are used to control and confine the movement of photons in two or three dimensions[121, 122]. PCs of silicon can be synthesized using finely controlled methods such as lithography [123] and glancing angle deposition [124]. Recently, a 2-D silicon PC was shown to increase absorption efficiency of photovoltaic cells by 31% when compared with a c-Si film with a distributed Bragg reflector [125]. Additionally, theory has shown that morphology-dependent resonances can enhance internal fields in silicon nanowires [52]. Experimental results have demonstrated increased absorption in nanowire-patterned silicon as compared with planar silicon across the visible and near-infrared regions of the electromagnetic spectrum [126]. Although Si-IV nanowires with direct-gap transitions have been synthesized through chemical vapor deposition methods[117], we show here that Si-IV can be recovered in silicon nanowires previously prepared through chemical etching after near-hydrostatic compression up to 17 GPa in a diamond anvil cell (DAC). These results demonstrate the feasability of designing PCs with cubic silicon and recovering exotic phases after pressurization while maintaining complex

morphologies created through lithographic processing.

Silicon nanowires (SiNWs) were prepared through metal-assisted chemical etching (MACE) [24]. A silicon wafer with <111> orientation, doped with boron to a resistivity of 11 Ω cm, was immersed in a solution of 1:1 volume ratio of 10 M HF:0.04 M $AgNO_3$ for 3 hours. The etched wafer was then immersed in a 1:1 volume ratio solution of 30% (v/v) NH_4OH:28% (v/v) H_2O_2 which has been shown to remove any residual silver particles [83]. The resulting nanowire array was sonicated to suspend the nanowires in deionized H_2O. Pressure modulation was achieved using a Boehler-Almax plate DAC and diamonds with 0.3 mm culets. A tungsten probe was used to transfer nanowires dried from the suspension onto the diamond anvil culet along with micrometer-scale ruby grains which were used to monitor the pressure inside the cell [127]. A rhenium gasket was used as a spacer after it was dimpled to a thickness of 50 μm and a hole with 150 μm diameter was drilled with an electrostatic-discharge machine (Hylozoic Products, Seattle). The cell was then sealed and pressurized initially using either a 4:1 volume ratio or methanol:ethanol mixture or cryogenically loaded argon as a near-hydrostatic pressure transfer medium. By gradually tightening the cell, the diamond culets were advanced closer to each other, thereby increasing pressure in the cell.

Raman scattering from individual SiNWs at high pressures was observed by focusing a 532 nm laser through a 50x objective into the DAC, as illustrated in Figure 4.4, to a spot size of $\sim$3 μm and dispersing the back-scattered signal onto a liquid nitrogen-cooled charge-coupled device (CCD) through a 0.5 m spectrograph with a 2400 l/mm holographic grating and slit-width of 20 μm giving a resolution of 0.3 cm^{-1}. Raman shift values obtained from spectra of SiNWs were calibrated to $\pm$1 cm^{-1} using Raman scattering spectra from cyclohexane.

In situ Raman spectra from 12 individual SiNWs at increasing pressures (Fig. 4.5) show a quadratic dependence of the Si-I first-order longitudinal-transverse optical (LTO) phonon

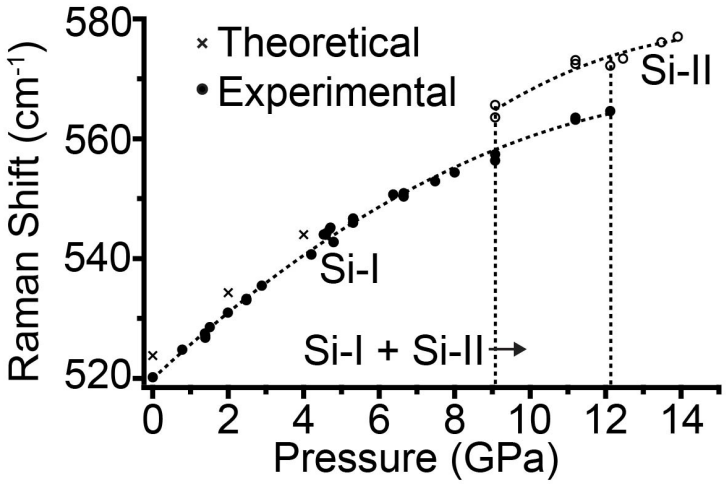

Figure 4.5: In-situ Raman scattering from 12 individual SiNWs under compression in the DAC shows the onset of the Si-I to Si-II phase transition near 9 GPa with a complete transition to Si-II at 12.3 GPa. DFT simulations of the Si-I LTO mode agree well with experimental results in the range of 0 to 4 GPa.

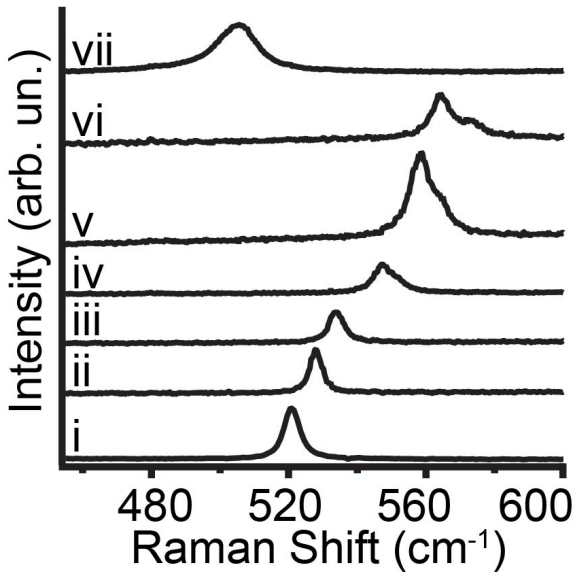

Figure 4.6: Raman scattering of a SiNW at (i) atmospheric pressure before compression, (ii) 1.4 GPa, (iii) 2.5 GPa, (iv) 6.4 GPa, (v) 9.1 GPa, (vi) 11.2 GPa, and (vii) after decompression to atmospheric pressure, confirming a Si-IV phase.

with a fit described by the equation

$$\omega_I = 520.0 \pm 0.44 \text{ cm}^{-1} + (5.88 \pm 0.17 \text{ cm}^{-1} \text{ GPa}^{-1})P + (-0.184 \pm 0.014 \text{ cm}^{-1} \text{ GPa}^{-2})P^2. \tag{4.12}$$

The vibrational frequencies of atoms in a solid are dependent on the volume and can be described by the mode Grüneisen parameter

$$\gamma_i = -\frac{\partial \ln \omega_i}{\partial \ln V} = \frac{1}{\chi_T \omega_i} \frac{\partial \omega_i}{\partial P} \tag{4.13}$$

where ω_i is the frequency of the ith mode, V is the crystal volume, and χ_T is the isothermal compressibility. Using a bulk value [128] for $\chi_T = 0.01012$ GPa^{-1}, the mode Grüneisen parameter is calculated to be 1.12, which is in agreement with other findings [129, 130].

Unique to these measurements is the existence of two modes simultaneously (Fig. 4.6) in the pressure range of 9–12 GPa, which is likely due to the decrease in hydrostaticity of Ar, the pressure medium used in this particular case, above 9 GPa [131]. Previous reports [112, 113, 115] have shown through X-ray measurements that both Si-I (diamond) and Si-II (tetragonal) (Fig. 4.7) are stable at these pressures, however, Raman scattering from Si-II has, to the author's knowledge, not yet been observed. The two distinct modes have a separation of approximately 10 cm^{-1} which persists until 12.3 GPa when the signal from the Si-I mode vanishes, suggesting the completion of the Si-I to Si-II phase transition. The continuity of the new mode past the I-II phase transition and up to 14 GPa indicates that the origin of the mode is indeed from the Si-II phase since it has been shown [114, 115] to be the stable phase across the range of 12–14 GPa. The next increase in pressure resulted in a sudden jump to 17 GPa, at which point the Raman signal was no longer discernible. This loss of signal is likely due to another phase transition, Si-II to Si-V (primitive hexagonal), which is expected near 15 GPa [113]. Upon decreasing the pressure from the maximum pressure achieved (17 GPa) to 10 GPa it was noted that Raman scattering could not be recovered from any of

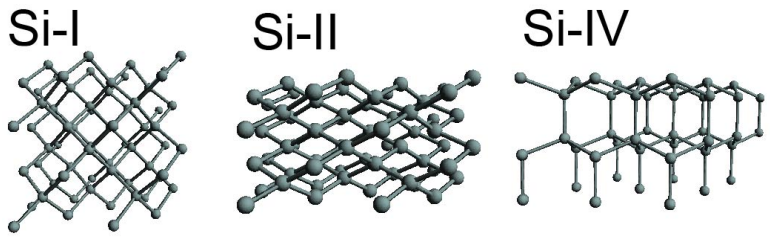

Figure 4.7: Crystal structures for the relevant phases of silicon: diamond cubic (Si-I), body-centered tetragonal (Si-II), and diamond hexagonal (Si-IV).

the SiNWs. Attempts were made to decrease pressure gradually below 10 GPa to probe for additional phase changes, but further loosening of the DAC tension screws resulted in an uncontrolled pressure release to 1 bar. However, once atmospheric pressure was restored and the NWs could be probed directly, Raman signal from exotic phases was observed with the dominant signal resulting from the Si-IV phase (Fig. 4.6) which has a diamond hexagonal structure. Recovery of Si-IV in MACE-prepared SiNWs demonstrates the possibility of also recovering Si-IV in exotic morphologies of Si produced through lithography [123] or other methods.

We were also interested in evaluating the predictive capabilities of density functional theory (DFT) for pressure-dependence of Raman shifts and high pressure phase transitions. Simulations were performed with the Quantum Espresso software package [132] using a diamond cubic unit cell with 8 Si atoms and a lattice parameter of 5.43 Å. A variable cell relaxation and subsequent phonon calculation were performed across a range of pressures, yielding theoretical Raman shifts for the LTO mode of Si-I. For the range of 0-4 GPa, the numerically calculated value for $\Delta\omega/\Delta P$ was found to be 5.05 cm^{-1}/GPa, which has a difference of less than 2% from the experimental result. However, as the simulated pressure was increased past 4 GPa, the disagreement between theory and experiment became significant and no phase change occurred in the simulation even up to pressures of 80 GPa. The results of these simulations indicate the inaccuracy of DFT for high pressure phase transitions of Si.

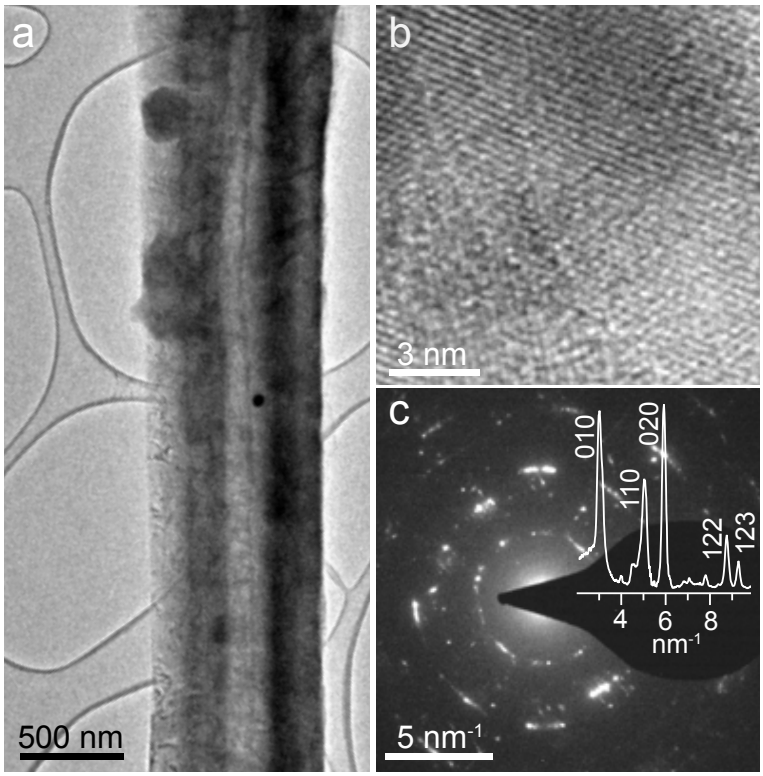

Figure 4.8: (a) Bright-field transmission electron micrograph of a SiNW recovered from DAC experiments which ultimately reached a pressure of 17 GPa. (b) High resolution TEM of the SiNW shows that a crystalline structure was maintained upon decompression. (c) SAED of the SiNW demonstrates diffraction from multiple domains and the integrated ring pattern can be indexed to a Si-IV phase.

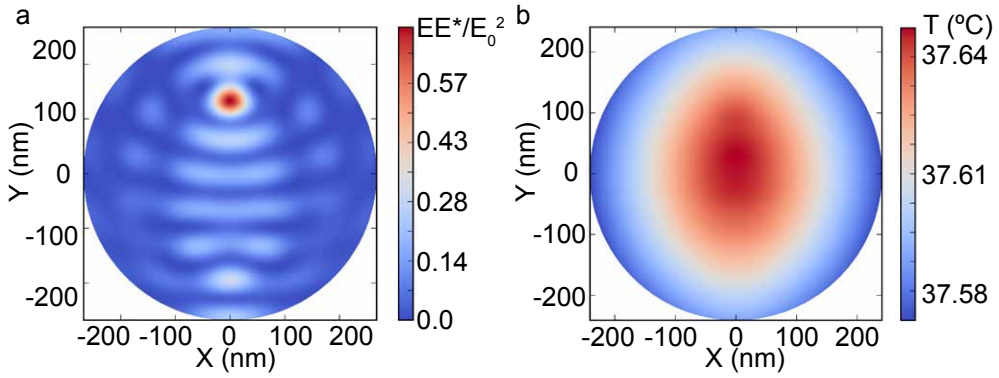

Figure 4.9: (a) Theoretical, normalized internal electric field for a SiNW with a 483 nm diameter illuminated with a 532 nm laser in solid argon. (b) Theoretical temperature profile for the SiNW under 25 kW/cm^2.

After decompression, recovered SiNWs were then transfered to a lacey carbon transmission electron microscopy (TEM) grid for further structural characterization. Bright-field TEM images reveal multiple domains within a single nanowire (Fig. 4.8a). High-resolution TEM (Fig. 4.8b) shows the crystallinity of one domain as an example while ring patterns from select area electron diffraction (SAED) (Fig. 4.8c) over the entire nanowire confirm the existence of multiple phases within a single SiNW where each of the strongest peaks can be indexed to planes from the Si-IV wurtzite phase with unit cell parameters of $a = 3.8$ Å and $c = 6.27$ Å. Secondary peaks suggest domains of either Si-I or Si-III, but the intensities are too weak for conclusive assignment.

Laser heating was reported by Khachadorian et al. [133] to have influenced Raman measurements of SiNWs. The results, however, did not show any change in Raman shift or linewidth of the LTO Si mode for laser powers in the range of 1 to 40 mW. Moreover, all Raman measurements conducted at higher pressures near phase transitions (> 8 GPa) were done with a laser power of 5 mW or less. To make predictions of the SiNW temperature due to photothermal heating an analysis of laser heating of infinite cylinders [52] was performed using the Python computer code (see Appendix A.5). The analysis was applied to predict the temperature of a SiNW in a matrix of 4:1 methanol:ethanol having a thermal conductivity

of 2 W/m K [134]. This provides an upper bound on the temperature when considering the NW is positioned in contact with one diamond anvil surface. As shown in Figure 4.9a, the internal field has a maximum that is approximately 70% of the incident field's magnitude which corresponds to a temperature rise that is less than 13°C. Calculations for cylinders in a solid matrix of argon where the thermal conductivity is 5x higher [135] than that of the ethanol:methanol mixture predict a temperature rise of only 2°C. Therefore, pressure is likely the primary mechanism behind the observed phase transition to Si-IV.

In conclusion, silicon is one of the most popular materials in PV devices even though its indirect bandgap limits its conversion efficiency. Nanowires can be used to enhance internal fields and optical absorption but conversion of Si-I to Si-IV with a direct transition could also significantly increase efficiency in PV devices. Raman scattering from individual SiNWs up to a pressure of 17 GPa indicates the onset of a pressure-induced phase change from Si-I to Si-II near 9 GPa with complete transtition at 12.3 GPa and Si-II to Si-V transition between 14 and 17 GPa. We have also recovered NWs at atmospheric pressure which demonstrate polymorphic Si with Si-IV as the dominant phase as evidenced by Raman scattering. Contrast seen in bright-field TEM images indicate multiple domains while high resolution TEM and SAED confirm that these domains are poly-crystalline and exhibit a Si-IV phase. Although the quantities of material obtained in these pressure-induced phase transition experiments are insufficient for solar-cell applications on a large scale, it does provide a method of studying their properties on a single particle level. It would also be of interest to perform compression recovery experiments on 1-D PCs of silicon to learn how the phase will influence the photonic properties of nanostructured Si materials (e.g. photonic crystals) that cannot be synthesized via vapor-liquid-solid syntheses.

Chapter 5

CADMIUM SULFIDE

5.1 Nonlinear heating of CdS nanoribbons

Heating and cooling of micro- and nano-scale particles photothermally can play a useful role in various fields of research including biomedicine (e.g. photodynamic therapy for destroying cancer cells), aerosol processes (e.g. atmospheric heating and cooling), optical data storage, and optical trapping. Much work has focused on spherical particles [136, 137] and droplets [138]. However, the novel properties of 1-D materials (i.e. nanowires) have recently generated a strong interest in wide range of fields [139], including lasers[140, 141], sensors [142], and solar conversion [143]. Optical tweezers provide an ideal method for studying individual nanowires, but because of the large irradiances used for optical trapping with lasers, significant heating occurs for many materials, and for highly absorbing materials superheating [26] or even boiling, as with carbon in water, of the solvent has been observed [144]. Since the fluid can also absorb at the laser wavelength the particle temperature depends on internal photothermal heating as well as heat transfer between the fluid and the particle. Consequently, there is need to predict the heating characteristics of such systems and the effects of the system parameters on the particle temperature. Here, we explore the optical trapping of CdS nanoribbons in D_2O in a laser tweezer to determine the contributions of fluid heating and photothermal particle heating to the particle temperature, where D_2O was selected rather than H_2O due to its lower absorption at the wavelengths used for trapping [145].

As a model material, CdS nanoribbons (CSNR) were synthesized using a chemical vapor deposition (CVD) method. [146] High purity (99.995%, Sigma Aldrich) CdS powder was placed in an alumina boat in a quartz tube with a 50 sccm flow of Ar with 5% H_2. The tube

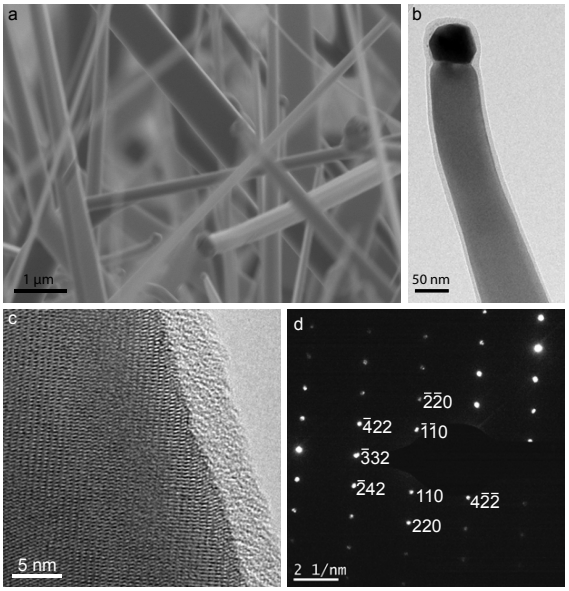

Figure 5.1: Characterization of synthesized CdS nanoribbons. (a) Scanning electron micrograph of as-synthesized CdS nanoribbons on a silicon wafer. (b) Low magnification transmission electron micrograph of a single CdS nanoribbon and the catalytic gold particle at the tip. (c) High-resolution transmission electron micrograph the same nanoribbon in (b) demonstrating the crystalline structure of the core with an amorphous surface layer. (d) Select-area electron diffraction of the nanoribbon in (b) and (c).

furnace temperature was set to $730°C$ and held for 30 min. Gold nanorods were deposited onto a <111> silicon wafer which was then placed downstream from the alumina boat in the quartz tube. After cooling to room temperature, a dense array of nanoribbons can be seen in scanning electron microscope (SEM) micrographs (Fig. 5.1a). Individual ribbons were transferred to a lacey carbon transmission electron microscope (TEM) grid for structural characterization. Brightfield (Fig. 5.1b) and high resolution (Fig. 5.1c) demonstrate high crystallinity with neglible defects as evidenced by homogeneous diffraction contrast. Select area electron diffraction (Fig. 5.1d) corroborates previous reports[146] of a wurtzite crystal phase with a $[11\bar{2}0]$ growth direction.

To obtain a suspension for optical trapping, the as-grown film of nanoribbons (Fig. 5.1a) was sonicated in D_2O for 5 minutes and diluted to an optimal concentration for trapping.

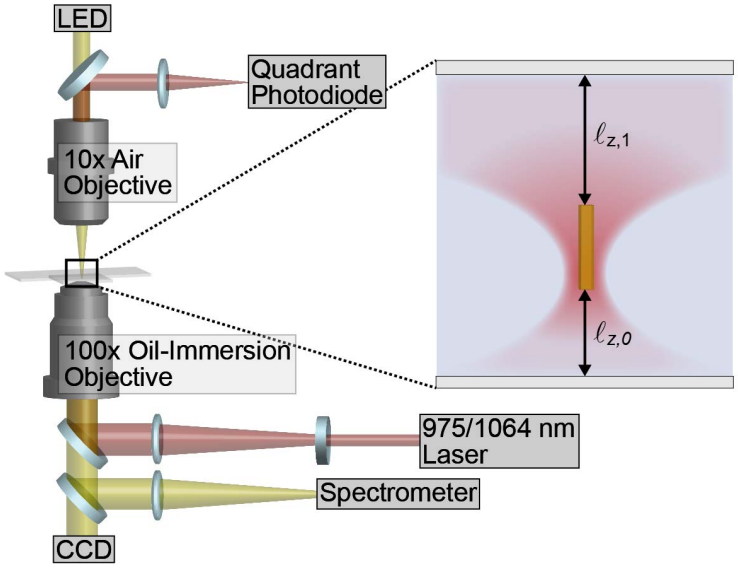

Figure 5.2: Schematic of the optical trapping system. Two near infrared (975 and 1064 nm) laser sources were co-aligned and expanded to overfill the back aperture of a 100x oil-immersion objective which was used to trap CSNRs in an aqueous suspension. The forward-scattered laser light was passed onto a quadrant photodiode for analysis of the particles' Brownian dynamics. Particles were imaged with a white LED and color CCD. Visible luminescence was characterized with a spectrometer. The zoom inset represents a single trapped CSNR and the distances between the bottom and top coverslips as used in the analytical theory.

A chamber was prepared by placing a drop of the CSNR suspension between a standard microscope slide and a #1 coverslip using a SecureSeal imaging spacer (Grace Bio-Labs). Trapping of individual CSNRs was accomplished using a custom system 5.2 where either a 1064 nm (SpectraPhysics) or 975 nm (Thorlabs) laser were expanded to overfill the back aperture of a 100x oil-immersion objective (Nikon, NA=1.25).

The intense irradiances (> 5 MW/cm^2) experienced in an optical trap are sufficient to induce a nonlinear response from certain materials, including two-photon pumping of aqueous dye solutions [83] and second harmonic generation (SHG) or sum frequency generation (SFG) from non-centrosymmetric nanostructures [147]. CSNRs, as mentioned above, exhibit a wurtzite structure which does not contain a center of symmetry. With a non-zero $\chi^{(2)}$, CSNRs

produce SHG signals when trapped at 1064 nm (Fig. 5.3a(i)) or, when trapped at 975 nm, SHG and two-photon photoluminescence (TPL) (Fig. 5.3a(ii)). Integration of the CSNR TPL (Fig. 5.3) demonstrates this nonlinearity within the irradiance range produced in the trap. It is evident from the spectrum that the TPL visible emission is produced non-parametrically when illuminated by the 975 nm laser and will, therefore, heat the CSNR through phonon generation (non-radiative relaxation) after absorption of one visible or two near infrared photons. The effect of the trapping wavelength relative to the particle temperature will be further discussed below. Although we also observed that when the 1064 and 975 nm lasers are co-aligned, the SFG signal is also observed in addition to the two SHG lines (Fig. 5.3a(iii)), the complications of modeling the temperature of a particle interacting with two optical traps simultaneously precludes the extraction of temperatures in this case.

Temperatures of trapped CSNRs were found using the previously described method (see Sec. 2.1. The Brownian dynamics of the trapped particle were analyzed by collecting the forward-scattered laser light through a 50x objective (Mitutoyo) and then focusing onto a quadrant photodiode (Thorlabs). The characteristic power spectrum of trapped CSNR can be fit to the functional form[23]

$$P(f) = \frac{D}{\pi^2(f^2 + f_c^2)} \tag{5.1}$$

to determine the diffusion coefficient, D, and corner frequency, f_c. Through the Einstein relation $D = k_B T/\gamma_{NR}$, the temperature, T, of the trapped particle can be found. The Stokes drag for a nanoribbon, γ_{NR}, was approximated using the formula for a cylindrical nanowire[25]

$$\gamma_{NR} = \frac{4\pi L}{\ln(L/2R) + 0.84}\eta(T) \tag{5.2}$$

where L and R are the length and radius of a nanowire, respectively, and $\eta(T)$ is the temperature-dependent viscosity of the solvent.

Temperatures for trapped CSNRs and silica microspheres as a function of irradiance are presented in Fig. 5.4. There is no significant difference between the resulting average tem-

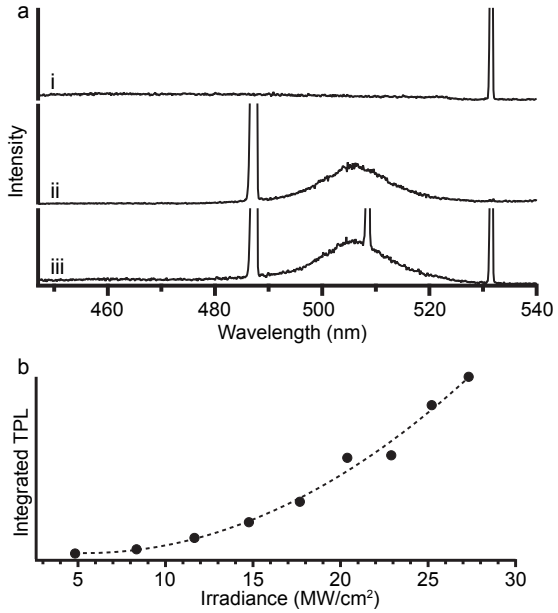

Figure 5.3: Nonlinear effects of an optically trapped CdS nanoribbon. (a) (i) SHG from a CdS nanoribbon trapped at 1064 nm. (ii) SHG and 2PPL from a CdS nanoribbon trapped at 975 nm. (iii) Co-aligned lasers with wavelengths of 975 and 1064 nm are able to generate second harmonics of both laser frequencies and the associated sum frequency in addition to the 975-pumped TPL from the CdS exciton within a single nanoribbon. (b) Integration of the TPL from a CdS nanoribbon trapped at 975 nm at increasing irradiance shows the nonlinear emission.

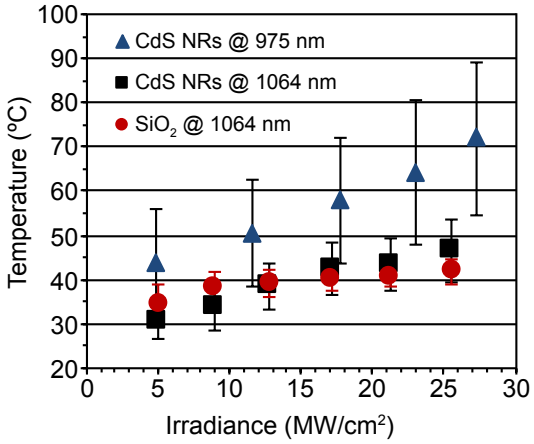

Figure 5.4: Average temperatures of 12 CdS NRs and 15 SiO_2 beads trapped with a 1064 nm laser in D_2O and 16 CdS NRs trapped at 975 nm.

peratures of the CdS nanoribbons and SiO_2 beads when trapped at 1064 nm. Consequently, we conclude that electromagnetic energy absorption by fluid heating dominated the particle heating since the SiO_2 beads do not absorb at the 1064 nm laser wavelength. However, when CdS NRs are trapped at a wavelength of 975 nm, the measured temperatures show a nonlinear increase compared to the linear trend exhibited by particles trapped at 1064 nm. To understand the influence of internal heating of the nanoribbons due to laser heating, we have developed a theoretical analysis of the photothermal heating process.

5.2 Rectangular Heating Theory Outline

Heating of a rectangular particle (rod, ribbon, or cube) due to electromagnetic radiation can be described by the unsteady-state, three-dimensional energy equation, which is written as

$$\rho_1 \hat{C}_1 \frac{\partial T}{\partial t} = \kappa_1 \left(\frac{\partial^2 T}{\partial x^2} + \frac{\partial^2 T}{\partial y^2} + \frac{\partial^2 T}{\partial z^2} \right) + S(x, y, z, t). \tag{5.3}$$

Here T is the particle temperature, x, y, z, and t are spatial and temporal coordinates and ρ_1, $\hat{C}_1$, and κ_1 are the density, heat capacity, and thermal conductivity, respectively, of the

particle. To simplify the solution, the dimensionless variables and parameters are defined as

$$\begin{gathered}\Theta = \frac{T - T_\infty}{T_\infty}, \quad \xi = \frac{x}{l_x}, \quad \eta = \frac{y}{l_y}, \quad \zeta = \frac{z}{l_z}, \\ \tau = \frac{\kappa_1 t}{\rho_1 \hat{C}_1 l_x^2}, \quad a = \frac{l_x}{l_y}, \quad b = \frac{l_x}{l_z},\end{gathered} \tag{5.4}$$

and the dimensionless heat source is

$$S^*(\xi, \eta, \zeta, \tau) = \frac{l_x^2 S(x, y, z, t)}{\kappa_1 T_\infty}, \tag{5.5}$$

where the temperature of the surrounding fluid far from the particle surface is T_∞, and l_x, l_y, and l_z are the dimensions of the particle, as shown in Fig. 5.6. With these substitutions, the dimensionless heat equation is now

$$\frac{\partial \Theta}{\partial \tau} = \frac{\partial^2 \Theta}{\partial \xi^2} + a^2 \frac{\partial^2 \Theta}{\partial \eta^2} + b^2 \frac{\partial^2 \Theta}{\partial \zeta^2} + S^*(\xi, \eta, \zeta, \tau). \tag{5.6}$$

The source term $S(x, y, z, t)$ depends on the intensity, polarization, and optical and electronic properties of the incident illumination, and is related to the internal electric field by

$$S = \frac{2\pi \mathrm{Re}[N_1]\mathrm{Im}[N_1]}{\lambda_{inc} \mu c} \mathbf{E} \cdot \mathbf{E}^*, \tag{5.7}$$

where N_1 is the complex refractive index of the particle, μ is its magnetic permeability, λ_{inc} is the wavelength of the incident irradiation, c is the speed of light in a vacuum, and $\mathbf{E}$ and $\mathbf{E}^*$ are the internal electric vector and its complex conjugate, respectively.

For the special cases of cylindrical rods and spheres, Mie theory can be applied to determine the source function, but for other geometries numerical methods are needed. Using a representative geometry as observed using atomic force microscopy (AFM) (Fig. 5.6a & b) a CSNR was modeled (Fig. 5.6c) using software involving the discrete dipole approximation (DDA) [148]. In the DDA numerical method, a particle is taken as finite number, N, of individual dipoles (Fig. 5.5). As N increases the resolution and accuracy of the simulation

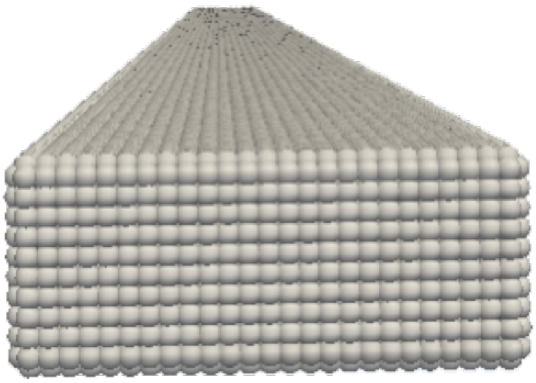

Figure 5.5: Representation of a rectangular nanowire discretized into an array of individual dipoles for numerical calculations of internal fields using the discrete dipole approximation.

may improve, but, obviously, this will come at a computational cost. The induced dipole, $\mathbf{P}_i$, at each point i is related to the electric field at the same point, $\mathbf{E}_i$ and its respective polarizability, α_i, through the relation

$$\mathbf{P}_i = \alpha_i \mathbf{E}_i, \tag{5.8}$$

where the polarizability is related to the dielectric constant, ϵ_i of the material. Although the Clausius-Mossotti polarizability was initially proposed by Purcell and Pennypacker [149]

$$\alpha_i^{CM} = \frac{3d^3}{4\pi} \frac{\epsilon_i - 1}{\epsilon_i + 2}, \tag{5.9}$$

where d is the spacing between dipoles, it is generally agreed upon that there needs to be some correction to account for radiative reactions [148]. A specific implementation of the DDA method will often provide multiple definitions for the dipole polarizability, depending on the

user's preference. The electric field felt at each dipole is then the combined result of the incident field and the field induced by every other dipole in the geometry. Mathematically, this is written as

$$\mathbf{E}_i = \mathbf{E}_{i,inc} - \sum_{j \neq i} \mathbf{A}_{ij} \mathbf{P}_j. \tag{5.10}$$

The complex matrix $\mathbf{A}_{ij}$ is often referred to as the interaction matrix and written as

$$\mathbf{A}_{ij} = \frac{\exp(ikr_{ij})}{r_{jk}} \left[k^2(\hat{r}_{ij}\hat{r}_{ij} - \mathbf{1}_3) + \frac{ikr_{ij} - 1}{r_{ij}^2}(3\hat{r}_{ij}\hat{r}_{ij} - \mathbf{1}_3) \right], \; i \neq j, \tag{5.11}$$

where $k \equiv \omega/c$, $r_{ij} \equiv |\mathbf{r}_i - \mathbf{r}_j|$, $\hat{r}_{ij} \equiv (\mathbf{r}_i - \mathbf{r}_j)/r_{ij}$, and $\mathbf{1}_3$ is the 3 x 3 identity matrix. The computational problem is reduced down to set of linear equations

$$\sum_{j=1}^{N} \mathbf{A}_{ij} \mathbf{P}_j = \mathbf{E}_{i,inc} \tag{5.12}$$

which are then solved for iteratively to obtain the polarizations of each dipole. This can then be used to calculate the field at each dipole according to Eq. 5.8.

An example of the normalized heat source ($\mathbf{E} \cdot \mathbf{E}^* / \mathbf{E}_{\mathbf{inc}}^{\mathbf{2}}$) for a CdS nanoribbon under 975 nm illumination is presented in Figure 5.6d & e. As the dimensions decrease the internal field becomes more uniform, while for larger sizes the three-dimensional internal field has a rich structure of peaks and valleys, as shown by Roder et al. [52] for cylindrical nanowires.

For small single particles trapped in a laser tweezer, Brownian motion leads to convective heat transfer between the particle surface and the surrounding fluid which affects the boundary conditions associated with the energy equation. There is considerable uncertainty about convective heat transfer between a nanoparticle and the surrounding fluid, as discussed below, but we can model the transport process by introducing appropriate heat transfer coefficients for the surfaces normal to the x and y directions. For the z direction the boundary conditions at the upper and lower surfaces depend on the configuration of the particle.

For a long rod (ribbon) suspended in an optical trap we assume that heat conduction

between the upper and lower surfaces is by conduction between the particle surface and the bounding surfaces of the laser trap chamber. Consequently, the non-dimensional boundary conditions become

$$\begin{aligned} \frac{dX}{d\xi}(0) = 0, \quad \frac{dX}{d\xi}(1) = -\mathrm{Bi}_x X(1), \\ \frac{dY}{d\eta}(0) = 0, \quad \frac{dY}{d\eta}(1) = -\mathrm{Bi}_y Y(1), \\ \frac{dZ}{d\zeta}(0) = \mathrm{Bi}_{z,0} Z(0), \\ \frac{dZ}{d\zeta}(1) = -\mathrm{Bi}_{z,1} Z(1) \end{aligned} \tag{5.13}$$

where the Biot numbers for the x and y directions are related to the appropriate heat transfer coefficients, h_x and h_y, and are defined by

$$\begin{aligned} \mathrm{Bi}_x \equiv \frac{h_x l_x}{\kappa_1}, \quad \mathrm{Bi}_y \equiv \frac{h_y l_y}{\kappa_1}, \\ \mathrm{Bi}_{z,0} \equiv \frac{\kappa_f l_z}{\kappa_1 l_{z,0}}, \quad \mathrm{Bi}_{z,1} \equiv \frac{\kappa_f l_z}{\kappa_1 l_{z,1}}, \end{aligned} \tag{5.14}$$

in which κ_f is the thermal conductivity of the fluid, $l_{z,0}$ is the distance between the bottom of the particle and the lower plate of an optical trap, $l_{z,1}$ is the distance between the top of the particle and upper plate of the trap as indicated in Fig. 5.2. It is convenient to define the parameters $\mathrm{Bi}_{z,0}$ and $\mathrm{Bi}_{z,1}$ as "equivalent" Biot numbers although they are based on conduction in the fluid rather than convection.

There is some uncertainty about heat transfer coefficients for nanorods and nanoribbons. Cheng et al.[150] reported heat transfer data for long cantilevered VO_2 nanorods having rectangular cross sections, and they presented their heat transfer results for low pressures of air as h versus a characteristic dimension L_c, where L_c is defined in terms of the volume of the rod, V_{rod}, and the surface area of the rod, A_{rod}, as follows

$$L_c = \frac{4V_{rod}}{A_{rod}}. \tag{5.15}$$

In this case the heat transfer coefficient is usually presented in the form of the Nusselt number

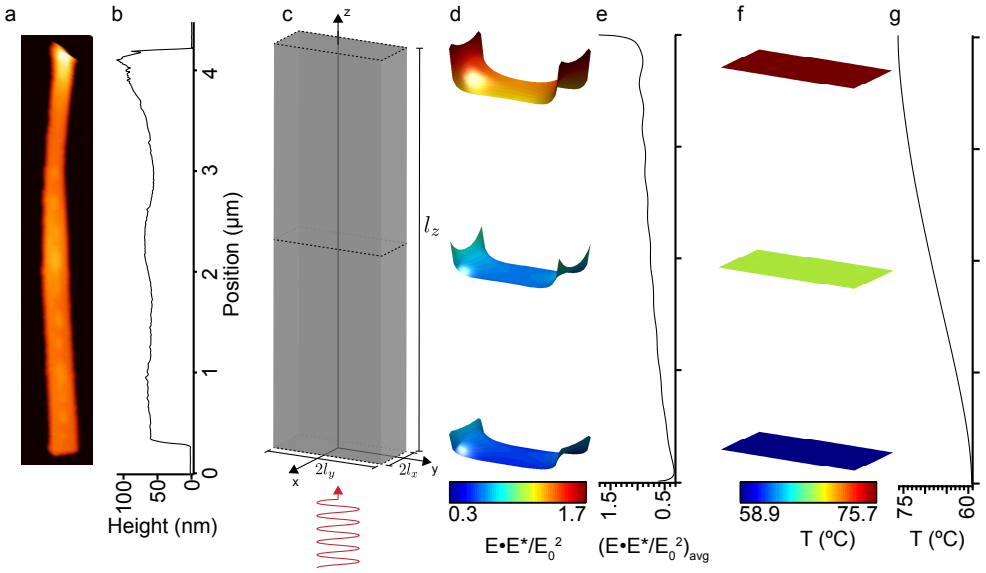

Figure 5.6: (a) Atomic force microscopy (AFM) image of a representative CSNR. (b) Line profile of the CSNR in the AFM image in panel (a). (c) Schematic of a 1D rectangular structure oriented with its long axis parallel to the direction of propagation of an electromagnetic wave as experienced in an optical trap. (d) Cross sectional profiles of the normalized electric field internal to the CSNR under 975 nm illumination with the (e) average axial field. (f) Cross sectional profiles of the theoretical temperatures under 975 nm illumination at 25 MW/cm^2 with the (g) axial average.

defined by

$$\mathrm{Nu} = \frac{hL_c}{\kappa_f} \tag{5.16}$$

Park et al. [151] reported heat transfer coefficients for nanorrods shaped like long capsules, that is, cylindrical rods with hemisperical ends. Their results for gold nanorods in methanol, ethanol, toluene, and hexane yield Nu = 1.82, 1.91, 2.00, and 2.10, respectively. Similar experiments by Ekici et al. [152] for gold nanorods in water yield Nu = 2.18 based on their assumed heat transfer coefficient, which was a value reported by Plech et al. [136] Consequently, we have used Nu = 2.00 in our calculations for nanoribbons.

The steady-state solution of the governing equations, obtained by classical methods in terms of a series of orthogonal functions, can be written as

$$\Theta(\xi,\eta,\zeta) = \sum_{lmn} A_{lmn} X_l(\xi) Y_m(\eta) Z_n(\zeta). \tag{5.17}$$

Here, the orthonormal eigenfunctions are defined by

$$\begin{aligned} X_l(\xi) &= \frac{\cos(\beta_l \xi)}{\|X_l\|}, \\ Y_m(\eta) &= \frac{\cos(\gamma_m \eta)}{\|Y_m\|}, \\ Z_n(\zeta) &= \frac{\cos(\delta_n \zeta) + \frac{\mathrm{Bi}_0}{\delta_n}\sin(\delta_n \zeta)}{\|Z_n\|}, \end{aligned} \tag{5.18}$$

where the norms are defined by

$$\|W\|^2 = \int_0^1 [W(\omega)]^2 d\omega, \tag{5.19}$$

in which $W = X,\ Y$, or Z, and $\omega = \xi,\ \eta$, or ζ.

Table 5.1: Eigenvalues for a CSNR with dimensions of 100 x 200 x 4000 nm.

l, m, n	β_l	γ_m	δ_n
1	0.1048	0.1480	0.0398
2	3.1451	3.1486	3.1421
3	6.2849	6.2867	6.2834
4	9.4259	9.4271	9.4249

The coefficients A_{lmn} are given by

$$A_{lmn} = \frac{1}{\alpha_{lmn}^2} \int_0^1 \int_0^1 \int_0^1 S^*(\xi', \eta', \zeta') X_l(\xi') Y_m(\eta') Z_n(\zeta') d\xi' d\eta' d\zeta' \tag{5.20}$$

where the primes indicate dummy variables of integration, and α_{lmn} is

$$\alpha_{lmn}^2 \equiv \beta_l^2 + a^2\gamma_m^2 + b^2\delta_n^2 \tag{5.21}$$

The eigenvalues satisfy transcendental equations given by

$$\begin{aligned} \tan(\beta_l) = \frac{\mathrm{Bi}_x}{\beta_l}, \quad \tan(\gamma_m) = \frac{\mathrm{Bi}_y}{\gamma_m}, \\ \tan(\delta_n) = \frac{-\mathrm{Bi}_0 + \delta_n \mathrm{Bi}_1}{\mathrm{Bi}_0 \mathrm{Bi}_1 + \delta_n^2}. \end{aligned} \tag{5.22}$$

Simulations using a representative NR geometry (Fig. 5.6a - c) and a wavelength of 1064 nm with the outlined theory predict temperature changes <20 mK for irradiances typical for optical trapping experiments. These results provide support to the experimental outcome where heating of CSNRs in an optical trap at 1064 nm is due solely to solvent absorption, identical to SiO_2 spheres. Should the reader be interested in their own calculations using the analysis given above, I have provided the first 4 eigenvalues for comparison in Table 5.1.

As pointed out earlier, however, trapping at 975 nm shows a significant increase in measured temperatures due to nonlinear absorption. To account for this increased heating in

the simulations, the imaginary index of refraction for CdS was increased until results were consistent with measured temperatures (Fig. 5.6g) relative to the background solvent absorption. The results of 975 nm simulations can be seen in Fig. 5.6d-g. The internal electric field varies significantly in the axial direction and relatively little transversely (Fig. 5.6d), but the corresponding temperature cross-sections (Fig. 5.6f) are uniform in the xy-plane. Along the z-axis, the ribbon acts as an antenna where the internal field (Fig. 5.6e) increases in the direction of propagation and so, consequently, the average axial temperature is also found to increase from the bottom to the top of the ribbon (Fig. 5.6g). Given that the 975 nm laser used for trapping these experiments is an unpolarized source, calculations were done using orthogonal polarizations and the average of the two outcomes was found to yield a refractive index $N = 2.3456 - i0.0001$. Essentially, this value is an effective imaginary index for CdS at 975 nm and could be used to account for nonlinear absorption in situations with large electromagnetic fields.

With these experiments, I have successfully synthesized cadmium sulfide nanoribbons and demonstrated that there is no measurable heating beyond solvent absorption for an optically trapped CSNR in a 1064 nm laser tweezer. The analysis of heating of a rectangular structure in an electromagnetic field gives temperatures rises less than 20 mK, which supports the experimental results. However, when CSNRs are trapped at a wavelength of 975 nm, a nonlinear heating trend is observed which is explained through the two-photon absorption above the band gap, followed first by a non-radiative relaxation to the band edge and final radiative recombination, supported by visible emission spectra from trapped NRs. The CVD synthesis used to produce CSNRs limits the cross-sectional dimensions but future efforts could explore methods for increasing and controlling these dimensions to generate morphology dependent resonances[52] which can lead to increased internal fields and, consequently, increased temperatures.

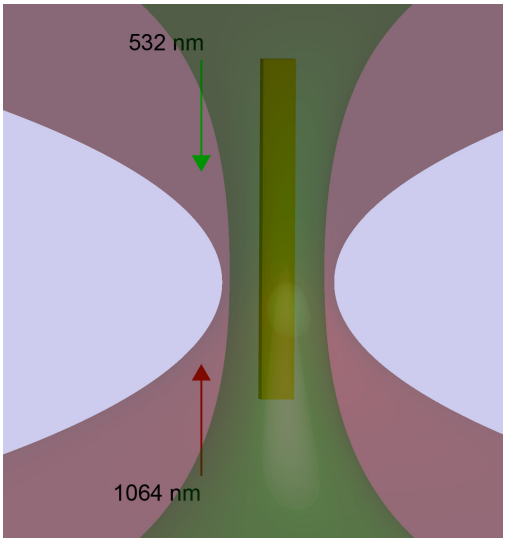

Figure 5.7: Schematic of the initially proposed experiment of cooling an optically trapped CSNR by irradiating with a counter-propagating 532 nm beam.

5.3 Challenges with Laser Cooling of Optically Trapped CdS Nanoribbons

Similar to our experiments demonstrating the laser refrigeration of optically trapped 10% Yb_{3+}-doped $YLiF_4$ crystals, as discussed in section 1.2, the initial goal was to experimentally demonstrate cooling of CSNRs trapped with a 1064 nm laser by co-aligning a 532 nm laser (Fig. 5.7. However, these experiments were never able to produce any detectable anti-Stokes photoluminescence. It had been suggested that interaction of the CSNR surface and solvent molecules can occur thereby introducing surface trap states [153–155] which can affect the luminescence spectral profile and quantum yields. To test the potential of surface effects in aqueous suspension, CSNRs were deposited on a SiO_2 window for use in a perfusion chamber. After identifying a CSNR with ideal PL characteristics (i.e. strong anti-Stokes band with no defect emission), a spectral profile was acquired under a 532 nm excitation at 1 mW. Next, de-ionized H_2O was perfused into the chamber and the CSNR was excited under the same conditions. A comparison of relative intensities can be seen in Figure 5.8. Integration of the emission profiles for each environment shows that ratio of efficiencies gives

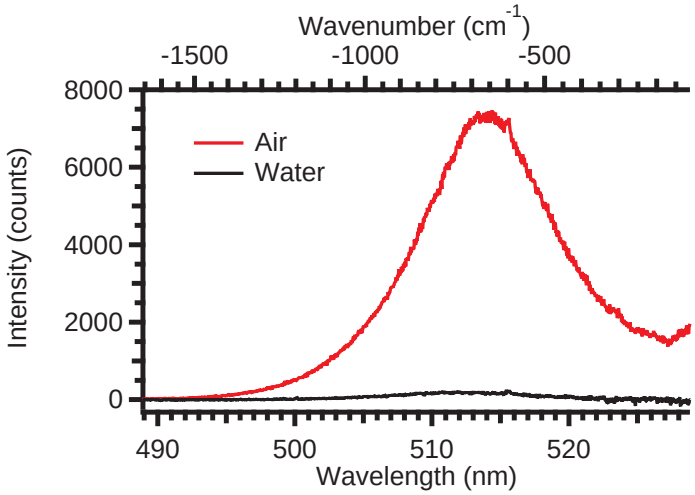

Figure 5.8: Relative emission intensities for a CSNR in air and water, demonstrating a large drop in quantum efficiency.

$\eta_{H_2O}/\eta_{air} = 0.025$. As it will be discussed in the following section, a material's ability to cool under laser irradiation is dependent on its quantum efficiency.

5.4 Entropy of Light

As pointed out in Sec. 1.2, a main focus of the Pauzauskie researh group has been the study of nanomaterials for laser refrigeration. A material's propensity for laser cooling, simply put, is determined by its ability to produce anti-Stokes luminescence. However, merely generating anti-Stokes photoluminescence is not sufficient for refrigeration. One method for evaluating a materials suitability for cooling is through an analysis of the entropy for both the incident and emitted light, as initially proposed by Landau [3]. To make a direct comparison between the light sources, Ruan et al. [4] have shown that the entropy flow rate, $\dot{S}$, per unit power, P, under a narrow-band approximation can be used, which is expressed as

$$\frac{\dot{S}}{P} = \frac{k_B}{\hbar\omega_0}\frac{(1+\bar{n})\ln(1+\bar{n}) - \bar{n}\ln\bar{n}}{\bar{n}}, \tag{5.23}$$

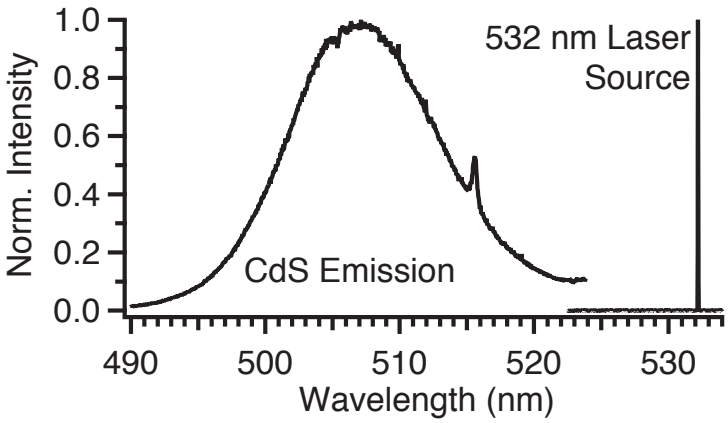

Figure 5.9: Emission profiles for the 532 nm SLM laser used to excite a CdS nanoribbon and the corresponding anti-Stokes emission profile.

where k_B and $\hbar$ are the Boltzmann and Planck's constants, respectively, ω_0 is the central frequency, and $\bar{n}$ is the average distribution function given by

$$\bar{n} = \frac{P}{A\Delta\omega\pi\sin^2\delta}\frac{4\pi^3c^2}{\hbar\omega_0^3}. \tag{5.24}$$

Here, P is the power, A is the emission area, $\Delta\omega$ is the spectral bandwidth, δ is the emission divergence angle, and c is the speed of light.

For the CdS nanoribbons synthesized in our lab, a typical emission profile is given in Fig. 5.9. Using parameters extracted from these profiles, values for $\dot{S}/P$ for the respective light sources were calculated and are listed in Table 5.4

	CdS Bandgap Emission	SLM Laser
Beam power, P (W)	0.001	0.001
Central wavelength, λ_0 (nm)	507.5	532.1
Wavelength bandwidth, $\Delta\lambda$ (nm)	14.3	0.018
Central frequency, ω_0 (rad/s)	$3.712 * 10^{15}$	$3.540 * 10^{15}$
Frequency bandwidth, $\Delta\omega$ (rad/s)	$1.046 * 10^{14}$	$1.120 * 10^{11}$
Surface area, A (m^2)	$3.926 * 10^{-11}$	$9.079 * 10^{-8}$
Beam divergence, δ (rad)	$\pi/2$	0.002
Average distribution function, $\bar{n}$	0.1602	17440
Entropy flow rate per unit power, $\dot{S}/P$ (K^{-1})	$1.026 * 10^{-4}$	$2.283 * 10^{-8}$

The results of entropy calculations for the two different types of luminescence demonstrates that the process does not violate the second law of thermodynamics. Further, it is possible to estimate the cooling efficiency limit from these values. Consider the first law of thermodynamics relative to a system of laser refrigeration

$$P_{out} = P_{in} + Q_c \tag{5.25}$$

where P_{out} and P_{in} refer to the emitted and incident light, respectively, and Q_c is the cooling load. Next, the second law can be expressed by relating the entropy flow rates for the absorbed irradiation, $\dot{S}_{in}$, output emission, $\dot{S}_{out}$, and thermal load, $\dot{S}_c$:

$$\dot{S}_{out} \geq \dot{S}_{in} + \dot{S}_c. \tag{5.26}$$

This can also be written as

$$P_{out}\left(\frac{\dot{S}}{P}\right)_{out} \geq P_{in}\left(\frac{\dot{S}}{P}\right)_{in} + \frac{Q_c}{T}. \tag{5.27}$$

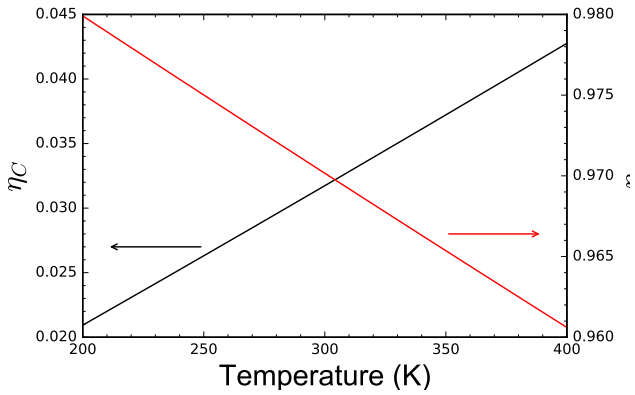

Figure 5.10: Evaluation of the Carnot efficiency limit and necessary quantum efficiency to achieve laser refrigeration for a CSNR under 532 nm irradiation.

Using the customary definition for refrigeration efficiency [4]

$$\eta = \frac{Q_c}{P_{in}}, \tag{5.28}$$

we can determine the Carnot limit (η_C) by combining equations 5.25, 5.27, and 5.28 to obtain

$$\eta_C = \frac{[(\dot{S}/P)_{out} - (\dot{S}/P)_{in}]T}{1 - (\dot{S}/P)_{out}T}. \tag{5.29}$$

An examination of Eq. 5.29 reveals that efficiency limits can be improved by maximizing $(\dot{S}/P)_{out}$ and minimizing $(\dot{S}/P)_{in}$. For a CdS nanoribbon at 300K under 532 nm excitation, an efficiency limit of $\sim$3% is predicted.

In addition to the theoretical efficiency limit which assumes a luminescence quantum efficiency (η_q) of 1, it is possible to estimate the threshold η_q at which cooling will occur. If an excitation can result in either an emitted photon or internal heat generation (Q_h) by non-radiative relaxation, we can express η_q as

$$\eta_q = \frac{P_{out}}{P_{out} + Q_h}. \tag{5.30}$$

Energy balance of the system now requires

$$P_{out} + Q_h = P_{in} + Q_c. \tag{5.31}$$

The net cooling power is the difference between the competitive cooling and heating, or

$$Q = Q_c - Q_h = P_{in}[\eta_C - (1 + \eta_C)(1 - \eta_q)/\eta_q], \tag{5.32}$$

and the cooling efficiency is

$$\eta = \frac{Q}{P_{in}} = \eta_C - (1 + \eta_C)(1 - \eta_q)/\eta_q. \tag{5.33}$$

To get the necessary η_q to achieve cooling as a function of temperature, $\eta = 0$ and we get

$$\eta_q = (1 + \eta_C/(1 + \eta_C))^{-1}. \tag{5.34}$$

Evaluation of equations 5.29 and 5.34 as a function of temperature are plotted in Figure 5.10. Analysis of the necessary quantum efficiency to achieve cooling demonstrates that although the absolute quantum efficiency of the as-synthesized CSNRs is unknown, even if it were unity the 2.5% achieved after placing the ribbon in H_2O is well below the η_q cooling threshold.

5.5 Temperature-dependent resonances of CdS Cantilevers

After evaluating the challenge of cooling an optically trapped CSNR due to its decreased η_q in aqueous solvents, I proposed to evaluate temperatures of laser-irradiated CSNRs that had been freely suspended from the edge of a silicon wafer by monitoring their resonant frequencies. The movement of a cantilever can be described by the Euler-Bernoulli equation

$$EI\frac{\partial^4 y}{\partial x^4} + \rho A\frac{\partial^2 y}{\partial t^2} = 0 \tag{5.35}$$

where E is the Young's modulus, I is the second moment of inertia, ρ is the density, and A is the cross-sectional area. Equation 5.35 can be solved [156] to give the resonance frequency, f_n of each bending mode for a cantilever of length L and thickness h

$$f_n = \frac{\beta_n^2}{4\sqrt{3}\pi}\frac{h}{L^2}\sqrt{\frac{E}{\rho}} \tag{5.36}$$

where β_n are the solutions of

$$1 + \cos\beta_n \cosh\beta_n = 0. \tag{5.37}$$

From Eq. 5.36 it can be seen that the frequency is dependent on three variables, specifically the geometry, the material density and Young's modulus. Although each of these parameters will presumably have some temperature dependence, it has been shown [157] for cantilevers comprised of a single material that the dominating factor is the temperature dependence of the Young's modulus. It was the goal of these experiments to utilize this thermal dependence to calibrate and monitor temperatures of CdS cantilevers.

To prepare cantilevers, CdS nanoribbons were first synthesized as described in Section 5.1 producing a dense film of randomly oriented, 1-dimensional structures (Fig. 5.11a). X-ray diffraction (Fig. 5.11b) of the film confirms a wurtzite crystal stucture [146]. Mechanical exfoliation of the film onto a silicon wafer provided isolated nanoribbons which could then be transferred to another silicon chip in a cantilever geometry using an electronically controlled tungsten probe.

After the preparation of CdS cantilevers on Si, the chip was placed into a Janis ST-500 cryostat which was then evacuated to a pressure $< 10^{-7}$ mbar. A custom Raman spectroscopy system (Fig. 5.12) was used to probe the resonances of individual cantilevers. A 532 nm SLM laser (Coherent Compass 315M) was spectrally cleaned by passing the beam through a holographic laser bandpass (Kaiser Optical) and then focused onto the cantilever using a long working distance 50x objective (Mitutoyo). The transmitted beam was focused onto an avalanche photodiode (Thorlabs APD430A2). The time-dependent voltage signal was

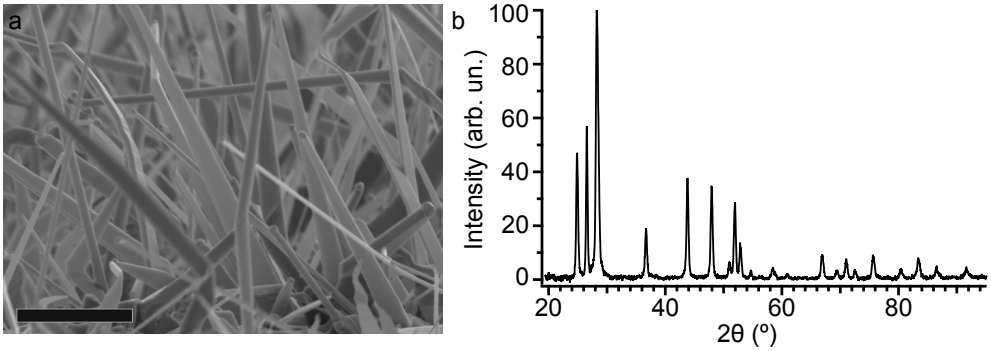

Figure 5.11: Characterization of CdS nanoribbons. (a) Scanning electron micrograph of as-synthesized nanoribbons. Scalebar = 4 μm. (b) X-ray diffraction of as-synthesized nanoribbons matching a wurtzite crystal structure.

monitored and analyzed using custom written code using LabView software (see Appendix A.4). Photoluminescence spectra of individual nanoribbons were obtained by collecting emission through the 50x objective, filtering the pump signal with a notch filter (Kaiser Optical, SuperNotch Plus) and focusing into a spectrometer (Acton, SpectraPro 500i) with a liquid nitrogen-cooled detector (Princeton Instruments).

Like any other method, to accurately measure the temperature of a cantilever (Fig. reffig:cala) through the measurement of its resonant frequency it is necessary to first calibrate the frequencies across the entire temperature range of interest. Calibration was performed at 20 K intervals between 240 and 320 K with a laser power of 50 μW at 532 nm. Because each cantilever's geometry is different, its respective resonant frequencies will be different, according to Eq. 5.36. But normalization of the frequencies to the resonance at 240 K ($f(T)/f(240K)$) can provide information on the Young's modulus temperature coefficient for cadmium sulfide. A plot of 23 separate resonances found from 13 individual CdS cantilevers (Fig. 5.13b) gives a slope of -149 ppm/K, which matches previous reports [158].

Once each cantilever's resonances had been calibrated, the cryostat was set to a temperature of 280 K and the laser power was increased and resonances were recorded at powers of 160, 320 and 480 μW. An example cantilever is shown in Fig. 5.14a. The anti-Stokes's

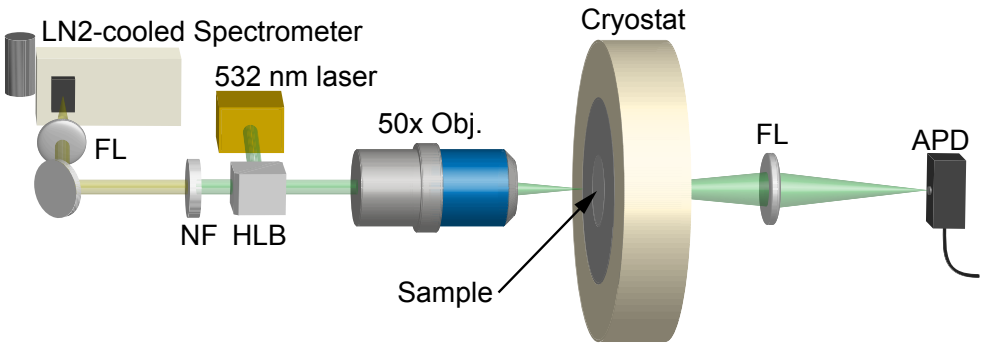

Figure 5.12: Schematic of the experimental setup used to detect resonances of cantilevers where the 532 nm excitation source was passed through holographic laser bandpass (HLB) cube into a 50x objective and focused onto the tip of a cantilever. Focusing lenses (FL) were used to direct the transmitted beam onto an avalanche photodiode (APD) for resonance measurements and to collect photoluminescence for spectral analysis using a spectrometer with a L-N_2-cooled detector. Intense scattering from the 532 nm source was attenuated using a notch filter (NF).

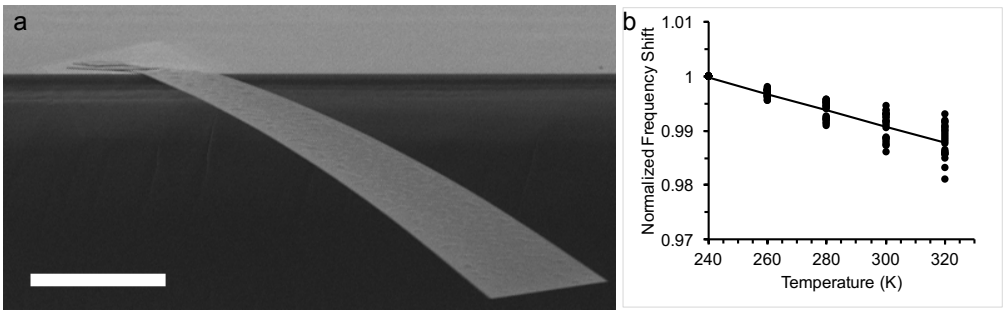

Figure 5.13: (a) SEM image of a CdS nanoribbon suspended off the edge of a Si wafer. Scalebar = 5 μm. (b) Plot of 23 normalized resonances obtained from 13 individual CdS cantilevers as a function of temperature and a linear fit with a slope of -149 ppm/K.

photoluminescence at increasing powers is shown in Fig. 5.14b, demonstrating the existence of the mechanism necessary for cooling. However, as discussed in Sec. 5.4, what it is not known is the quantum efficiency, which should be in excess of 97% at a temperature of 280 K to achieve refrigeration. The frequency at increasing powers for the cantilever in Fig. 5.14a are shown in Fig. 5.14c. Seeing as the temperature coefficient for the modulus has a negative value (Fig. 5.13b), it is clear that the nanoribbon is heating as the laser power is increased. In fact, a subsequent increase in power to 1000 μW resulted in ablation of the wire tip as indicated by the green circle in Fig. 5.14a. The heating results observed seem to contradict the reports of Zhang et al. [6], especially where they report cooling at powers as high as 12 mW and cantilevers in these experiments undergo degradation (presumably due to intense heating) at powers that are approximately an order of magnitude smaller. The average temperature found at the powers evaluated show a consistent heating trend amongst each of the cantilevers (Fig. 5.14d).

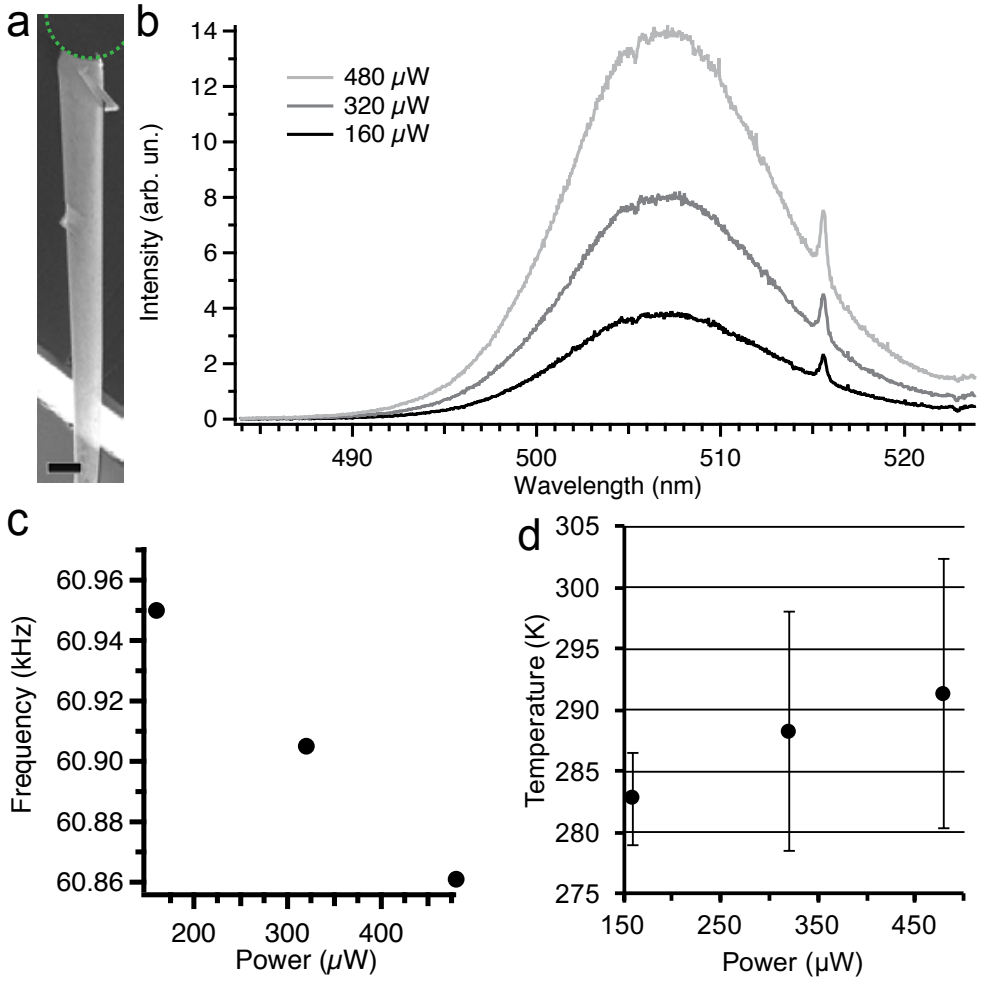

Figure 5.14: (a) SEM image of a CSNR cantilever. Dotted green circle indicates the profile of the beam location when the CSNR was ablated at a power or 1000 μW. Scalebar = 2 μm. (b) Anti-Stokes photoluminescence under increasing powers of the CSNR in panel (a). (c) Measured resonant frequencies of the CSNR cantilever in panel (a) as a function of 532 nm laser power, indicating a rise in temperature as power is increased. (d) Average calculated temperatures of 12 resonances from multiple cantilevers, demonstrating an overall heating trend as the 532 nm power is increased.

Chapter 6

CONCLUSION

As part of a young research group, there are many opportunities to explore a wide variety of research topics before the group eventually settles on a more defined track of experiments. This is evidenced in the many different projects that I have been able to either contribute or lead over the past 5 years. In chapter 1, I introduced the laser tweezer system, the main tool of our group, and how it was developed to extract temperatures from trapped particles, eventually leading to the collaborative effort to demonstrate laser refrigeration of 10%Yb^{3+}:YLF microcrystals by 15 K from ambient temperatures. My proposed thesis was intended to follow these experiments with cooling of optically trapped CdS nanoribbons, although I later realized the entropic challenges with the experimental design.

In chapter 2, I detailed the methods for extracting temperatures from a laser tweezer and showed how these measurements were applied to intrinsic and ion-implanted silicon nanowires, ultimately demonstrating the ability to superheat the local water environment. These experiments eventually led me to explore the photochemical effects of SiNWs in an optical trap. Using a commercial dye and two-photon pumping from the trapping source, I was able to verify that both silicon nanowires and gold nanorods are able to sensitize singlet oxygen in aqueous solutions. The implication of potential photo-induced chemistry in an optical tweezer is valuable information for the trapping community.

Chapter 3 gives the details of nonlinear optical studies in a LT, building on my laser spectroscopy and nonlinear optics interests vis-à-vis the $^1O_2$ dye fluorescence experiments. Here, I found that by trapping a $KNbO_3$ nanowire with a NIR source, the second harmonic signal could be enhanced through Fabry-Pérot resonances within the optical cavity (i.e. nanowire). By co-aligning multiple sources, tunable sum frequency generation was demonstrated. The

trapped wires were also found to heat beyond solvent background absorption, which is likely due to lattice defects incurred during the hydrothermal synthesis.

Part of the necessary infrastructure to reproduce laser cooling of CdS nanoribbons was a 532 nm laser source. Chapter 4 discusses the Raman system that I designed and assembled for general use by lab members and for use in the semiconductor laser refrigeration experiments. The system has been utile for the group and I have been able to use it for several separate projects. Rotational-vibrational modes of gaseous O_2 molecules were observed. High pressure phases changes of SiNWs were probed with Raman spectroscopy and through the use of a diamond anvil cell.

After building the necessary infrastructure and knowledge-base, I proceeded with experiments to reproduce previous reports of semiconductor cooling. The first experiments demonstrated the nonlinear heating of trapped CSNRs and estimation of nonlinear absorption coefficients through an analytical solution to the heat equation. I quickly realized, however, that it was improbable that trapped CSNRs would demonstrate any cooling due to the extremely low quantum yield when suspended in H_2O. The experiments were then adjust to look at resonant frequencies of cantilevered CSNRs in a vacuum. The temperature-dependent Young's modulus could be employed to first calibrate a cantilever's resonance as a function of temperature and then determine temperatures as laser power increased. The results of the experiments indicate an overall heating trend with cases where the heating progressed to the point of ablating the CSNR at the focal point of the beam.

Given these results, the claims of cooling remain unverified. I am skeptical of the reports since the influence of high carrier concentrations within the semiconductor can complicate the luminescence and potentially corrupt temperature estimations. However, entropy requires quantum yields of these materials to be near unity at temperatures around 300 K and our lab is not currently equipped to make these measurements. Future efforts could benefit from pursuing evaluations of CSNR quantum yields. But it is clear that simpler, mechanistic studies on the material are needed to better understand whether or not the Varshni shift may have been misinterpreted.

LIST OF PUBLICATIONS

P.B. Roder, **B.E. Smith**, E.J. Davis, and P.J. Pauzauskie. Photothermal Heating of Nanowires. *The Journal of Physical Chemistry C*, 118(3):1407–1416, 2014.

S. Manandhar, P.B. Roder, J.L. Hanson, M.B. Lim, **B.E. Smith**, A. Mann, and P.J. Pauzauskie Rapid Sol-Gel Synthesis of Nanodiamond Aerogel. *Journal of Materials Research*, 29(24):2905–2911, 2014.

B.E. Smith, P.B. Roder, J.L. Hanson, S. Manandhar, A. Deveraj, D. Perea, W.J. Kim, A.L.D. Kilcoyne, and P.J. Pauzauskie. Singlet-oxygen Generation from Individual Semiconducting and Metallic Nanostructures during Near-Infrared Laser Trapping. *ACS Photonics*, 2(4):559–564, 2015.

B.E. Smith, P.B. Roder, X. Zhou, and P.J. Pauzauskie. Nanoscale materials for hyperthermal theranostics. *Nanoscale*, 7(16):7115–7126, 2015.

B.E. Smith*, P.B. Roder*, X. Zhou, and P.J. Pauzauskie. Hot Brownian thermometry and cavity-enhanced harmonic generation with nonlinear optical nanowires. *Chemical Physics Letters*, 639:310–314, 2015.

P.B. Roder, S. Manandhar, **B.E. Smith**, X. Zhou, V. Shutthanandan, and P.J. Pauzauskie. Photothermal Superheating of Water with Ion-Implanted Silicon Nanowires. *Advanced Optical Materials*, 3(10):1362–1367, 2015.

P.B. Roder*, **B.E. Smith***, X. Zhou*, M.J. Crane, and P.J. Pauzauskie. Laser refrigeration of hydrothermal nanocrystals in physiological media. *The Proceedings of the National Academy of Sciences of the United States of America*, 112(49):15024–15029, 2015.

B.E. Smith, X. Zhou, P.B. Roder, and P.J. Pauzauskie. Recovery of hexagonal Si-IV nanowires from extreme GPA pressure. *Journal of Applied Physics*, 119(18):185902, 2016.

B.E. Smith, X. Zhou, E.J. Davis, and P.J. Pauzauskie. Photothermal Heating of Nanoribbons. *Optical Engineering*, Submitted.

X. Zhou, **B.E. Smith**, P.B. Roder, P.J. Pauzauskie. Laser refrigeration of ytterbium-doped sodium-yttrium-fluoride nanocrystals. *Advanced Materials, (in press)* 2016.

---

* Indicates equal contribution

Appendix A

CODES

A.1 Matlab: Er^{3+} Spectroscopic Analysis

```
% Script to integrate the specified areas (2) from the
% Princeton 500i SpectraPro spectrum SPE files assuming multiple trials
%
% Author: Bennett Smith, University of Washington, Pauzauskie Group
% Created: 12 Mar 2014
% Updated: 12 Mar 2014

clear
close all;

%% Variables
filenameA='Er2Yb10YLF_br_'; % First portion of repetitive filename
filenameB='.SPE'; % Second portion of repetitive filename
trialCount=1;    % Starting trial
maxTrial=700;      % Maximum trial
trialStep=1;      % Trial Increment
%%%%%%%%%%%%%%%%%%%
startwl1=516;      % 516(New ErYbYLF), 460(YbYLF), 560(Rhodamine)
endwl1=532;        % 532(New ErYbYLF), 475(YbYLF), 600(Rhodamine)
startwl2=539;      % 539(New ErYbYLF), 475(YbYLF), 660(Rhodamine)
endwl2=562;        % 562(New ErYbYLF), 490(YbYLF), 700(Rhodamine)
%%%%%%%%%%%%%%%%%%%
basestartwl=580;  % Baseline start wavelength (580 ErYbYLF)
baseendwl=590;    % Baseline end wavelength (600 ErYbYLF)
plotstartwl=500;  % Plot start wavelength (500 ErYbYLF)
```

```
plotendwl=600;     % Plot end wavelength (600 ErYbYLF)
beamWaist=1.1*10^-4; % Beam waist in cm (1.1 um for laser tweezer)
beamArea=pi*(beamWaist/2)^2;

%% Background File
bgchk=input('Subtract a background from separate file? (y/n): ', 's');
if bgchk == 'y'
    [bgfilename,bgpathname,~]=uigetfile();
    bgfile=strcat(bgpathname,bgfilename);
    fid=fopen(bgfile,'r');

    % Polynomial degree
    errchk=fseek(fid,3101,'bof');
    polydeg=fread(fid,1,'char');
    if errchk == -1
        error('Unable to extract polynomial degree for wavelength calibration'
    );
    end

    % Polynomial coefficients
    errchk=fseek(fid,3263,'bof');
    polycoeff=fread(fid,6,'double');
    if errchk == -1
        error('Unable to extract polynomial coefficients for wavelength
    calibration');
    end

    % Generate wavelength vector
    polycoeff=polycoeff(1:polydeg+1); % Remove all but non-zero elements
    polycoeff=flipud(polycoeff); % Flips vector to decreasing polynomial
    coefficients
    pxl=(1:1:1340)';
    wavelength=polyval(polycoeff,pxl);
```

```
    % Get Data type
    errchk=fseek(fid,108,'bof');
    dataType=fread(fid,1,'uint16');
    if errchk == -1
        error('Unable to determine data type');
    end
    if dataType == 0
        type='single';
    elseif dataType == 1
        type='int32';
    elseif dataType == 2
        type='int16';
    elseif dataType == 3
        type='uint16';
    else
        error('Error');
    end

    % Get CCD data
    errchk=fseek(fid,4100,'bof');
    data=fread(fid,1340,type);

    % Combine into single matrix
    bgMtrx=[wavelength,data];
else
    bgMtrx=0;
end
fclose all;

%% Spectra Import
% Ask for baseline subtraction
if bgchk == 'n'
```

```
    basechk=input('Subtract the baseline? (y/n): ', 's');
else
    basechk='n';
end
figure(1)
axes('FontSize',16.0,'FontWeight','bold');
pathname=pwd; % Get current folder path
finalArrayCnt=1; % Increment for matrix building
maxEm1=0; % Maximum from region 1
maxEm2=0; % Maximum from region 2
while trialCount <= maxTrial;
    filename = [filenameA...
        num2str(trialCount) filenameB];

    if exist(filename)
        % Import the file
        file=strcat(pathname,'/',filename);
        fid=fopen(file,'r');

        % Polynomial degree
        errchk=fseek(fid,3101,'bof');
        polydeg=fread(fid,1,'char');
        if errchk == -1
            error('Unable to extract polynomial degree for wavelength
   calibration');
        end

        % Polynomial coefficients
        errchk=fseek(fid,3263,'bof');
        polycoeff=fread(fid,6,'double');
        if errchk == -1
            error('Unable to extract polynomial coefficients for wavelength
   calibration');
```

```
        end

        % Get Data type
        errchk=fseek(fid,108,'bof');
        dataType=fread(fid,1,'uint16');
        if errchk == -1
            error('Unable to determine data type');
        end
        if dataType == 0
            type='single';
        elseif dataType == 1
            type='int32';
        elseif dataType == 2
            type='int16';
        elseif dataType == 3
            type='uint16';
        else
            error('Error');
        end

        % Get CCD data
        errchk=fseek(fid,4100,'bof');
        data=fread(fid,1340,type);
        if errchk == -1
            error('Unable to extract CCD data');
        end

        % Generate wavelength vector
        polycoeff=polycoeff(1:polydeg+1); % Remove all but non-zero elements
        polycoeff=flipud(polycoeff); % Flips vector to decreasing polynomial
    coefficients
        pxl=(1:1:1340)';
        wavelength=polyval(polycoeff,pxl);
```

```
% Combine into single matrix
dataMtrx=[wavelength,data];
Ndatapts=length(dataMtrx);

% Get baseline average (only if background is not subtracted)
if basechk == 'y'
    step=1;
    for i=1:Ndatapts
        if dataMtrx(i,1) >= basestartwl && dataMtrx(i,1) <= baseendwl
            BLArray(step,1)=dataMtrx(i,2);
            step=step+1;
        end
    end
    aveBL=mean(BLArray);
else
    aveBL=0;
end

% Subtract background/baseline (if selected)
corrDataMtrx(:,1)=dataMtrx(:,1);
if bgchk == 'y'
    corrDataMtrx(:,2)=dataMtrx(:,2)-bgMtrx(:,2);
elseif basechk == 'y'
    corrDataMtrx(:,2)=dataMtrx(:,2)-aveBL;
else
    corrDataMtrx(:,2)=dataMtrx(:,2);
end

% Code to remove cosmic rays
erp=5; % Set percentage error limit
err=erp/100;
for i=1:Ndatapts % This loop removes hot regions one pixel wide
```

```
        if i>1 ...
                && i<Ndatapts ...
                && corrDataMtrx(i,2)>(1+err)*corrDataMtrx(i+1,2) ...
                && corrDataMtrx(i,2)>(1+err)*corrDataMtrx(i-1,2) ...
            corrDataMtrx(i,2)=(corrDataMtrx(i-1,2)...
                +corrDataMtrx(i+1,2))/2;
        end

    end
    for i=1:Ndatapts % This loop removes hot regions up to 3 pixels wide
        if i>2 ...
                && i<Ndatapts-1 ...
                && corrDataMtrx(i,2)>(1+err)*corrDataMtrx(i+2,2) ...
                && corrDataMtrx(i,2)>(1+err)*corrDataMtrx(i-2,2)
            corrDataMtrx(i,2)=(corrDataMtrx(i-2,2)...
                +corrDataMtrx(i+2,2))/2;
            corrDataMtrx(i-1,2)=(corrDataMtrx(i,2)...
                +corrDataMtrx(i-2,2))/2;
            corrDataMtrx(i+1,2)=(corrDataMtrx(i+2,2)...
                +corrDataMtrx(i,2))/2;
        end
    end
    for i=1:Ndatapts % This loop removes dead regions one pixel wide
        if i>1 ...
                && i<Ndatapts ...
                && corrDataMtrx(i,2)<(1-err)*corrDataMtrx(i+1,2) ...
                && corrDataMtrx(i,2)<(1-err)*corrDataMtrx(i-1,2) ...
            corrDataMtrx(i,2)=(corrDataMtrx(i-1,2)...
                +corrDataMtrx(i+1,2))/2;
        end

    end
    for i=1:Ndatapts % This loop removes dead regions up to 3 pixels wide
```

```
    if i>2 ...
            && i<Ndatapts-1 ...
            && corrDataMtrx(i,2)<(1-err)*corrDataMtrx(i+2,2) ...
            && corrDataMtrx(i,2)<(1-err)*corrDataMtrx(i-2,2)
        corrDataMtrx(i,2)=(corrDataMtrx(i-2,2)...
            +corrDataMtrx(i+2,2))/2;
        corrDataMtrx(i-1,2)=(corrDataMtrx(i,2)...
            +corrDataMtrx(i-2,2))/2;
        corrDataMtrx(i+1,2)=(corrDataMtrx(i+2,2)...
            +corrDataMtrx(i,2))/2;
    end
end

% Add spectrum to plot
hold on
figure(1)
plot(corrDataMtrx(:,1),corrDataMtrx(:,2),'k');

% Create array for region of interest 1(region to integrate)
step=1;
for i=1:Ndatapts
    if corrDataMtrx(i,1) >= startwl1 && corrDataMtrx(i,1) <= endwl1
        integArray1(step,1)=corrDataMtrx(i,1);
        integArray1(step,2)=corrDataMtrx(i,2);
        step=step+1;
    end
end

% Create array for region of interest 2 (region to integrate)
step=1;
for i=1:Ndatapts
    if corrDataMtrx(i,1) >= startwl2 && corrDataMtrx(i,1) <= endwl2
        integArray2(step,1)=corrDataMtrx(i,1);
```

```
                integArray2(step,2)=corrDataMtrx(i,2);
                step=step+1;
            end
        end

        % Integrate 2 regions
        area1=trapz(integArray1(:,1),integArray1(:,2));
        area2=trapz(integArray2(:,1),integArray2(:,2));
        ratio=area1/area2;
        lnratio=log(ratio);

        % Convert ratio to temperature
        slope=-771.295;
        intercept=0.72822;
        temp=((lnratio-intercept)/slope)^-1-273.15;

        % Add to final results
        finalResults(finalArrayCnt,1)=trialCount;
        finalResults(finalArrayCnt,2)=lnratio;
        finalArrayCnt=finalArrayCnt+1;

        % Get maximum emission (for plotting below)
        if maxEm1 < max(integArray1(:,2))
            maxEm1=max(integArray1(:,2));
        end
        if maxEm2 < max(integArray2(:,2))
            maxEm2=max(integArray2(:,2));
        end
    end

    trialCount=trialCount+trialStep;
end
```

```
% Statistics
average=mean(finalResults(:,2));
stdev=std(finalResults(:,2));

%% Plotting
figure(1)
xlabel('Wavelength (nm)','FontSize',20);
ylabel('Counts','FontSize',20);
% Indicate Regions for integration
lnspc=max(max(maxEm1,maxEm2))*0.05;
l2x1=startwl2;
l2y1=maxEm2+lnspc;
l2x2=endwl2;
l2y2=l2y1;
line([l2x1,l2x2],[l2y1,l2y2],'Color','k',...
    'LineWidth',3)
txtspc=l2y1*0.08;
text((l2x2+l2x1)/2,l2y1+txtspc,'E1','FontSize',18,...
    'HorizontalAlignment','center')
l1x1=startwl1;
l1y1=maxEm1+lnspc;
l1x2=endwl1;
l1y2=l1y1;
line([l1x1,l1x2],[l1y1,l1y2],'Color','k',...
    'LineWidth',3)
text((l1x2+l1x1)/2,l1y1+txtspc,'E2','FontSize',18,...
    'HorizontalAlignment','center')
xlim([plotstartwl plotendwl])

figure(2)
axes('FontSize',16.0,'FontWeight','bold');
plot(finalResults(:,1),finalResults(:,2),'ko',...
    'MarkerFaceColor','k');
```

```
%axis([3.08 3.37 -1.96 -1.84]);
%title('0.01% Eb^{3+}, 10% Yb^{3+}:YLF pumped at 1020 nm','FontSize',20,'
    FontWeight','bold');
ylabel('ln(E2/E1)','FontSize',20,'FontWeight','bold');
xlabel('Trial Number','FontSize',20,'FontWeight','bold');
%text(5.5,43,[num2str(average,3) ' \pm ' num2str(stdev,2) '\circC'],'FontSize
    ',18);
%text(5.5,43.2,'Set Temp:  35\circC','FontSize',18);

figure(2)

save('ratiostats_erybylf.dat', 'finalResults', '-ASCII')
```

A.2 Matlab: Rectangular Heating Theory

```
%%%%%%%%%%%%%%%%%%%%%%%%%%%%%%%%%%%%%%%%%%%%%%%%%%%%%%%%%%%%%%%%%%%%%%%%%%%%
%%%%%%%%%%%%%%%%%%%% RIBBON THEORY USING DDSCAT %%%%%%%%%%%%%%%%%%%%%%%%%%%%
%%%%%%%%%%%%%%%%%%%%%%%%%%%%%%%%%%%%%%%%%%%%%%%%%%%%%%%%%%%%%%%%%%%%%%%%%%%%
% This code implements heating theory for a nanoribbon developed in the
% Pauzauskie Group in the Materials Science & Engineering department at
% the University of Washington, building on the theory set forth in
% the article by P. B. Roder, P.J. Pauzauskie and E. J. Davis titled,
% "Nanowire Heating by Optical Electromagnetic Irradiation" published in
% Langmuir 2012, 28, 16177-16185 and
% See Bennett Smith's Notebook #2  pp. 99-104 for further details on the
% ribbon theory
% Created: Oct 2013
% Updated: 29 Sep 2015

close all
reuseDDA=input('Do you want to keep the same DDSCAT results from the last run
    ?: (y/n)', 's');
if reuseDDA == 'y'
```

```
    clearvars -except EEfield comp xcoord ycoord zcoord reuseDDA
else
    clearvars -except reuseDDA
end

%% Variables
%%%%%%%%%%%%%%%%%%%%%%%%%%%%%%%%%%%%%%%%%%%%%%%%%%%%%%%%%%%%%%%%%%%%%%%%%%%%%%%%
material=1; % 1=CdS; 2=KNbO3
length=4*10^-6; % Give the length of the particle in meters
temp_infC=25; % Assumed infinite temperature (C)
lambda_laser=1.064; % Give the wavelength of the laser in micrometers
DDSCATpol=2; % Polarization of Efield in DDSCAT simulation
ddscatfilename = (['CdSNR00006_E' num2str(DDSCATpol) '_1064nm_1.vtr']);
irrad=25; % laser irradiance in MW cm^-2
eigValNo=8; % Number of eigenvalues to calculate
spacer=150*10^-6; % Spacer thickness in meters
Nu=0.24; % 0.32 represents Nu number taken from cylindrical case by PB Roder

%% Output
%%%%%%%%%%%%%%%%%%%%%%%%%%%%%%%%%%%%%%%%%%%%%%%%%%%%%%%%%%%%%%%%%%%%%%%%%%%%%%%%
writeFieldMovCheck = 0; % 1 to write AVI movie of normalized field along axis,
    0 to skip
writeTempMovCheck = 0; % 1 to write AVI movie of temperature distribution
   along axis, 0 to skip
plotFieldCheck = 1; % 1 to plot average field along axis, 0 to skip
plotTempCheck = 1; % 1 to plot average temperature along axis, 0 to skip
savVarChk = 0; % 1 to save variables

%% Constants
%%%%%%%%%%%%%%%%%%%%%%%%%%%%%%%%%%%%%%%%%%%%%%%%%%%%%%%%%%%%%%%%%%%%%%%%%%%%%%%%
muPerm_0=1.2566*10^-6; % Magnetic permeability (N A^-2)
cvel=299792458; % Velocity of light in vacuum (m s^-1)
epsilon=8.854188*10^-12; %Free Space permittivity (F m^-1=W s V^-2 m^-1)
```

```
%% Individual Materials Properties
%%%%%%%%%%%%%%%%%%%%%%%%%%%%%%%%%%%%%%%%%%
N_water=[0.488, 1.33548+1i*9.6880*10^-10; ... % Real and imaginary values
   taken from refractiveindex.info
         0.532, 1.33372+1i*1.4992*10^-9; ...
         0.975, 1.32700+1i*3.4800*10^-6; ...
         0.980, 1.32700+1i*3.3620*10^-6; ...
         1.020, 1.32670+1i*3.5900*10^-6; ...
         1.030, 1.32655+1i*3.9400*10^-6; ...
         1.040, 1.32640+1i*4.2900*10^-6; ...
         1.064, 1.32604+1i*5.1300*10^-6];

kappa_water=0.58; % Thermal conductivity of medium (water) (W m^-1 K^-1)

N_CdS=[0.532, 2.66970+1i*0.687549; ... % Real values from refractiveindex.info
   ; Imaginary from DOI: 10.1364/OE.21.019302
       0.975, 2.34561+1i*0.00009; ...
       0.980, 2.34482+1i*0.000001; ...
       1.020, 2.33895+1i*0.000001; ...
       1.030, 2.33761+1i*0.000001; ...
       1.040, 2.33631+1i*0.000001; ...
       1.064, 2.33335+1i*0.00006];

N_KNbO3=[0.975, 2.1248+1i*0.0034; ...
    1.020, 2.1220+1i*0.000001; ...
    1.030, 2.1214+1i*0.000001; ...
    1.040, 2.1208+1i*0.000001; ...
    1.064, 2.1195+1i*0.0005];

% Select medium refractive index based on laser wavelength
[m,~]=size(N_water);
N_2=0;
```

```
for i=1:m
    if N_water(i,1)==lambda_laser
        N_2=N_water(i,2);
    end
end

% Select properties based on chosen material
if material==1
    % CdS Constants
    kappa = 40.1; % Thermal conductivity of material (W m^-1 K^-1)
    rho = 4.82*10^3; % Density of material (kg/m^3)
    C_pm = 47.293; % Molar heat capacity (J/(mol K)) of CdS @ 298 K (from RP
    Breyer et al., J Chem Thermodynamics, 1983, 15, 827-834)
    C_p = 369.0288; % Specific heat (J/(kg K)) of CdS (Klocek,"Handbook of IR
    optical materials", 1991,p222)
    Nmat=N_CdS;
elseif material==2
    % KNbO3 Constants
    kappa = 11; % Thermal conductivity (W / m K) http://dx.doi.org
    /10.1063/1.2978072
    rho = 4.62*10^3; % Density http://www.surfacenet.de/html/potassium_niobate
    .html
    C_p = 628; % Value for LiNbO3 (J / kg K): http://www.korth.de/index.php
    /162/items/19.html
    Nmat=N_KNbO3;
else
    error('Material does not have properties ')
end

% Select refractive index of material
[m,~]=size(Nmat);
N_1=0;
for i=1:m
```

```
    if Nmat(i,1)==lambda_laser
        N_1=Nmat(i,2);
    end
end

% Determine if medium and material have index of refraction for selected
    wavelength
if N_2==0 || N_1==0
    error('Error: Medium and/or material information needed for selected
    wavelength');
end

% Calculated quantities
irradSI=irrad*10^6*10^4;
E_0=sqrt(2*irradSI/(cvel*epsilon*real(N_2))); % (V m^-1)
temp_inf=temp_infC+273.15;
alpha = kappa/(rho*C_p); %Thermal diffusivity
sigma = 4*pi*real(N_1)*imag(N_1)/(lambda_laser*10^-6*muPerm_0*cvel); %
    Electrical Conductivity (S m^-1)

%% DDSCAT Import
%%%%%%%%%%%%%%%%%%%%%%%%%%%%%%%%%%%%%%%%%%%%%%%%%%%%%%%%%%%%%%%%%%%%%%%%
if reuseDDA == 'n'
    disp('Importing DDSCAT file...');
    tic
    fid = fopen(ddscatfilename);
    tline = fgetl(fid);
    count = 1;
    while ischar(tline)
        if count == 6
            xcoord=tline;
            xcoord=str2num(xcoord); %#ok<ST2NM>
        end
```

```
        if count == 9
            ycoord=tline;
            ycoord=str2num(ycoord); %#ok<ST2NM>
        end
        if count == 12
            zcoord=tline;
            zcoord=str2num(zcoord); %#ok<ST2NM>
        end
        if count == 17
            EEfield=tline;
            EEfield=str2num(EEfield); %#ok<ST2NM>
        end
        if count == 20
            comp=tline;
            comp=str2num(comp); %#ok<ST2NM>
        end
        tline=fgetl(fid);
        count = count+1;
    end
    fclose(fid);
    toc
end

%% DDSCAT Analysis
%%%%%%%%%%%%%%%%%%%%%%%%%%%%%%%%%%%%%%%%%%%
[~,Nx]=size(xcoord); %Find number of dipoles in each direction
[~,Ny]=size(ycoord);
[~,Nz]=size(zcoord);
EEfield3dmat=reshape(EEfield,Nx,Ny,Nz); %(EE* still unitless) Redimension
    EEfield data into 3d matrix
comp3dmat=reshape(comp,Nx,Ny,Nz); % Redimension compositional data to 3d
    matrix
```

```
normnwfieldonly(:,:,:)=EEfield3dmat(:,:,:).*comp3dmat(:,:,:); % Normalized 3d
    EEfield of NW only

% These loops will remove any slices from the computational area that are
% completely outside the geometry to determine dipole spacing, height
% and width

% Length loop
count=1;
for i=1:Nx
    EEFieldSum=0;
    for j=1:Ny
        for k=1:Nz
            EEFieldSum=EEFieldSum+normnwfieldonly(i,j,k); % Sum EEfield for
    each layer along x-axis
        end
    end
    if EEFieldSum ~= 0
        cnstrctxnwfield(count,:,:)=normnwfieldonly(i,:,:); %#ok<SAGROW> %
    Generate matrix with geometry
        count=count+1;
    end
end
[Nx,~,~]=size(cnstrctxnwfield);
dspace=length/Nx;

% Width loop
count=1;
for k=1:Nz
    EEFieldSum=0;
    for j=1:Ny
        for i=1:Nx
```

```
            EEFieldSum=EEFieldSum+cnstrctxnwfield(i,j,k); % Sum EEfield for
    each layer along x-axis
        end
    end
    if EEFieldSum ~= 0
        cnstrctznwfield(:,:,count)=cnstrctxnwfield(:,:,k); %#ok<SAGROW> %
    Generate matrix with geometry
        count=count+1;
    end
end
[~,~,Nz]=size(cnstrctznwfield);
width=Nz*dspace;
widthVec=linspace(-width/2, width/2,Nz)*10^6; % Generates vector representing
    ribbon width in real space

% Height loop
count=1;
for j=1:Ny
    EEFieldSum=0;
    for k=1:Nz
        for i=1:Nx
            EEFieldSum=EEFieldSum+cnstrctznwfield(i,j,k); % Sum EEfield for
    each layer along x-axis
        end
    end
    if EEFieldSum ~= 0
        cnstrctynwfield(:,count,:)=cnstrctznwfield(:,j,:); %#ok<SAGROW> %
    Generate matrix with geometry
        count=count+1;
    end
end
[~,Ny,~]=size(cnstrctynwfield);
height=Ny*dspace;
```

```
heightVec=linspace(-height/2,height/2,Ny)*10^6;

% These definitions are set forth in the theory developed by EJ Davis and
% Bennett Smith
Lz=length;
Ly=width/2;
Lx=height/2;
a=Ly/Lx;
b=Lz/Lx;

%% Biot Numbers
%%%%%%%%%%%%%%%%%%%%%%%%%%%%%%%%%%%%%%%%%%%%%%%%%%%%%%%%%%%%%%%%%%%%%%%%%%%%
volume=length*width*height;% Volume of ribbon
area=length*width*2+length*height*2+height*width*2;% Surface area of ribbon
L_char=4*volume/area;
h_coeff=Nu*kappa_water/L_char;
dist1=(spacer-length)/2;
dist2=dist1;
Bix=h_coeff*(height/2)/kappa;
Biy=h_coeff*(width/2)/kappa;
Bi0=kappa_water/kappa*(length/dist1);
Bi1=kappa_water/kappa*(length/dist2);

%% Preallocate Matrices
%%%%%%%%%%%%%%%%%%%%%%%%%%%%%%%%%%%%%%%%%%%%%%%%%%%%%%%%%%%%%%%%%%%%%%%%%%%%
[alpha_m,beta_n,gamma_p,norm_m,norm_n,norm_p]=deal(zeros(eigValNo,1));
[checkx,checky,checkz]=deal(zeros(eigValNo,eigValNo));
[omega_mnp,W_mnp]=deal(zeros(eigValNo,eigValNo,eigValNo));
tempMatr=zeros(Ny,Nz,Nx);
aveLayerEEfield=zeros(Nx,2);
aveLayerTemp=zeros(Nx,2);

%% Source
```

```
%%%%%%%%%%%%%%%%%%%%%%%%%%%%%%%%%%%%%%%%%%%%%%%%%%%
sourceAdj=(Lx)^2*(1/2*sigma*cnstrctynwfield*(E_0^2))/(kappa*temp_inf);
sourceDDSCAT=cnstrctynwfield;
sourceS=1/2*sigma*sourceDDSCAT*(E_0^2);
source=sourceAdj;

%% Field Movie
%%%%%%%%%%%%%%%%%%%%%%%%%%%%%%%%%%%%%%%%%%%%%%%%%%%
% Generate movie visualizing EEfield while traveling along axis of particle
% including fields in the material only
if writeFieldMovCheck == 1
    writerObj = VideoWriter(['AxialFieldMovieE' num2str(DDSCATpol)]);
    open(writerObj);
    h=figure;
    for i=1:Nx
        if i==1
            surf(widthVec,heightVec,squeeze(cnstrctynwfield(i,:,:)));
            axis ([widthVec(1) widthVec(Nz) heightVec(1) heightVec(Ny) 0 max(
   max(max(cnstrctynwfield)))+0.1*max(max(max(cnstrctynwfield))) min(min(min(
   cnstrctynwfield))) max(max(max(cnstrctynwfield)))])
            colorbar('FontSize',20)
            title({'Normalized E*E','Axial Position ( \mum): ' num2str(i*
   dspace*10^6)},'FontSize',20)
            light('Position',[-1 0 50],'Style','local');
            lighting phong
            shading interp
            xlabel('\mum','FontSize',26);
            ylabel('\mum','FontSize',26);
            set(gca,'FontSize',20,'GridLineStyle','-');
            set(gca,'DataAspectRatio', [1 1 5]);
            set(gca,'nextplot','replacechildren');
            set(gcf,'Renderer','zbuffer');
            frame=getframe(h);
```

```
            writeVideo(writerObj,frame);
        else
            surf(widthVec,heightVec,squeeze(cnstrctynwfield(i,:,:)));
            light('Position',[-1 0 50],'Style','local');
            lighting phong
            shading interp
            %colorbar('FontSize',20)
            title({'Normalized E*E','Axial Position ( \mum): ' num2str(i*
    dspace*10^6)},'FontSize',20)
            frame=getframe(h);
            writeVideo(writerObj,frame);
        end
    end
    hold off
    close(writerObj);
end

%% Average Field & Plot
%%%%%%%%%%%%%%%%%%%%%%%%%%%%%%%%%%%%%%%%%%%%%%%%%%%%%%%%%%%%%%%%%%%%%%%%%%%%%%%
% This loop scans the entire computational area and extracts the average
% field per layer along the direction of propagation within just the particle
for i=1:Nx
    EEFieldSum=0;
    dipCount=0;
    for j=1:Ny
        for k=1:Nz
            EEFieldSum=EEFieldSum+source(i,j,k); % Sum EEfield for each layer
    along x-axis
            if source(i,j,k) ~= 0
                dipCount=dipCount+1; % Tally number of dipoles per layer
            end
        end
    end
```

```
    aveLayerEEfield(i,1)=i/Nx*length*10^6;
    if dipCount == 0
        aveLayerEEfield(i,2)=0; %Sets average EEfield to 0 outside the
    geometry
    else
        aveLayerEEfield(i,2)=EEFieldSum/dipCount; % Average EEField per layer
    end
end

% Fit to average field along axis
splineFit=fit(aveLayerEEfield(:,1),aveLayerEEfield(:,2),'splineinterp');
fitfun=@(x) splineFit(x); % Function representing the fit of the axial average

% Plot the average along the axis
if plotFieldCheck == 1
    figure(9)
    axes('FontSize',38.0,'FontWeight','bold');
    plot(aveLayerEEfield(:,1),aveLayerEEfield(:,2),'k');
    hold on
    plot(splineFit,'r')
    xlabel('Position (\mum)','FontSize',38);
    ylabel('S^*','FontSize',38);
    xlim([min(aveLayerEEfield(:,1)) max(aveLayerEEfield(:,1))])
end

%% Eigenvalues
%%%%%%%%%%%%%%%%%%%%%%%%%%%%%%%%%%%%%%%%%%%%%%%%%%%%%%%%%%%%%%%%%%%%%%%%%%%%
egnlim=0.001; % Set lower limit for eigenvalues
disp('Calculating Eigenvalues...');
tic
% Eigenvalues for x
options=optimset('Display','off'); % This suppresses the output from fzero due
    to its trying to locate complex zeros
```

```
start=0.1; % Specify starting value to determine eigenvalues
incr=pi; % Set resolution to check for eigenvalues
last=-0.001;
count=start;
temp=1;
f=@(x) x*sin(x)-Bix*cos(x); % Eigenvalue function
status=waitbar(0,'Calculating X Eigenvalues...');
while alpha_m(eigValNo) == 0
    checkEigV=fzero(f,count,options);
    if temp == 1
        if checkEigV-last > 0 && checkEigV > egnlim
            alpha_m(temp)=checkEigV;
            temp=temp+1;
            waitbar(temp/eigValNo);
        end
    else
        if (checkEigV - last > .001) && (checkEigV > egnlim) && (checkEigV > (
   alpha_m(temp-1)+.01))
            alpha_m(temp)=checkEigV;
            temp=temp+1;
            waitbar(temp/eigValNo);
        end
    end
    last=checkEigV;
    count=count+incr;
end
close(status)

% Eigenvalues for y
start=0.1; % Specify starting value to determine eigenvalues
incr=pi; % Set resolution to check for eigenvalues
last=-0.001;
count=start;
```

```
temp=1;
f=@(x) x*sin(x)-Biy*cos(x); % Eigenvalue function
status=waitbar(0,'Calculating Y Eigenvalues...');
while beta_n(eigValNo) == 0
    checkEigV=fzero(f,count,options);
    if temp == 1
        if checkEigV-last > 0 && checkEigV > egnlim
            beta_n(temp)=checkEigV;
            temp=temp+1;
            waitbar(temp/eigValNo);
        end
    else
        if (checkEigV - last > .001) && (checkEigV > egnlim) && (checkEigV > (
    beta_n(temp-1)+.01))
            beta_n(temp)=checkEigV;
            temp=temp+1;
            waitbar(temp/eigValNo);
        end
    end
    last=checkEigV;
    count=count+incr;
end
close(status)

% Eigenvalues for z
start=0.001; % Specify starting value to determine eigenvalues
incr=pi/10; % Set resolution to check for eigenvalues
last=-0.001;
count=start;
temp=1;
f=@(x) sin(x).*(x-(Bi1^2)/x)-2*Bi1*cos(x); % Eigenvalue equation
status=waitbar(0,'Calculating Z Eigenvalues...');
while gamma_p(eigValNo) == 0
```

```
    checkEigV=fzero(f,count,options);
    if temp == 1
        if checkEigV-last > 0 && checkEigV > egnlim
            gamma_p(temp)=checkEigV;
            temp=temp+1;
            waitbar(temp/eigValNo);
        end
    else
        if (checkEigV - last > .001) && (checkEigV > egnlim) && (checkEigV > (
   gamma_p(temp-1)+.01))
            gamma_p(temp)=checkEigV;
            temp=temp+1;
            waitbar(temp/eigValNo);
        end
    end
    last=checkEigV;
    count=count+incr;
end
close(status);

% Uncomment these lines to plot the z-eigenvalue function for sanity check
% xplot = 0:1/500:5;
% yplot = f(xplot);
% plot(xplot, yplot)
%%
% Omega constant
status=waitbar(0,'Calculating Constants (omega)...');
count=0;
for m=1:eigValNo
    for n=1:eigValNo
        for p=1:eigValNo
            omega_mnp(m,n,p)=(alpha_m(m))^2+(a^-2)*(beta_n(n))^2+...
                (b^-2)*(gamma_p(p))^2;
```

```
            waitbar((count/eigValNo^3))
            count=count+1;
        end
    end
end
close(status);
toc

%% Norms
%%%%%%%%%%%%%%%%%%%%%%%%%%%%%%%%%%%%%%%%%%%%%%%%%%%%%%%%%%%%%%%%%%%%%%%%%%%%%%%%
disp('Calculating Norms...');
tic
% Create matrix for alpha_m norm
status=waitbar(0,'Calculating X Norms...');
for m=1:eigValNo
    %norm_m(m)=1+sin(alpha_m(m))*cos(alpha_m(m))/alpha_m(m); % BES
    norm_m(m) = 0.5*(1+(sin(alpha_m(m)))^2/Bix);
    waitbar(m/eigValNo);
end
close(status);

% Create matrix for beta_n norm
status=waitbar(0,'Calculating Y Norms...');
for n=1:eigValNo
    %norm_n(n)=1+sin(beta_n(n))*cos(beta_n(n))/(beta_n(n)); % BES
    norm_n(n) = 0.5*(1+(sin(beta_n(n)))^2/Biy);
    waitbar(n/eigValNo);
end
close(status);

% Create matrix for gamma_p norm
status=waitbar(0,'Calculating Z Norms...');
for p=1:eigValNo
```

```
    norm_p(p) = 0.5 + ... % BES
                Bi0^2/(2*gamma_p(p)^2)+...
                Bi0/(gamma_p(p)^2)*(sin(gamma_p(p)))^2 + ...
                1/(2*gamma_p(p))*(1-Bi0^2/(gamma_p(p))^2)*sin(gamma_p(p))*cos(
    gamma_p(p));
%     norm_p(p) = 0.5*(1+Bi0^2/gamma_p(p)^2*... % EJD
%         (1/Bi0-Bi0/gamma_p(p)^2)*sin(gamma_p(p))^2);
    waitbar(p/eigValNo);
end
close(status);
toc

%% Eigenfunctions
%%%%%%%%%%%%%%%%%%%%%%%%%%%%%%%%%%%%%%%%%%%%%%%%%%%%%%%%%%%%%%%%%%%%%%%%%%%%%%%%
% The following are the eigenfunctions for each axis.  The orthonormality
% will be determined and output into checkx, checky, and checkz
% X_m = cos(alpha_m(m)*xi);
% Y_n = cos(beta_n(n)*eta);
% Z_p = cos(gamma_p(p)*zeta)+Bi0/gamma_p(p)*sin(gamma_p(p)*zeta);
for i=1:eigValNo
    for j=1:eigValNo
        XiXj=@(x) cos(alpha_m(i)*x).*cos(alpha_m(j)*x);
        checkx(i,j)=integral(XiXj,0,1);
    end
    checkx(i,i)=checkx(i,i)/norm_m(i);
end

for i=1:eigValNo
    for j=1:eigValNo
        YiYj=@(x) cos(beta_n(i)*x).*cos(beta_n(j)*x);
        checky(i,j)=integral(YiYj,0,1);
    end
    checky(i,i)=checky(i,i)/norm_n(i);
```

```
end

for i=1:eigValNo
    for j=1:eigValNo
        ZiZj=@(x) (cos(gamma_p(i)*x)+Bi0/(gamma_p(i)).*sin(gamma_p(i)*x)) ...
            .*(cos(gamma_p(j)*x)+Bi0/(gamma_p(j)).*sin(gamma_p(j)*x));
        checkz(i,j)=integral(ZiZj,0,1);
    end
    checkz(i,i)=checkz(i,i)/norm_p(i);
end

checkx(checkx<10^-14)=0; % Assume any value less than cutoff value is 0
checky(checky<10^-14)=0;
checkz(checkz<10^-14)=0;
disp(checkx)
disp(checky)
disp(checkz)


%% Coefficients (W_mnp)
%%%%%%%%%%%%%%%%%%%%%%%%%%%%%%%%%%%%%%%%%%%%%%%%%%%%%%%%%%%%%%%%%%%%%%%%%%%%%%%
% This loop will determine the coefficients for a steady state temperature
disp('Calculating Coefficients...');
tic
status=waitbar(0,'Calculating Coefficients...');
count=0;
for m=1:eigValNo
    for n=1:eigValNo
        for p=1:eigValNo
            tripInt=0;
            for X=1:Ny/2
                for Y=1:Nz/2
                    for Z=1:Nx
```

```
                        tripInt=tripInt+source(Z,X,Y)*...
                            (cos(alpha_m(m)*X/(Ny/2)))/(Ny/2)*...
                            (cos(beta_n(n)*Y/(Nz/2)))/(Nz/2)*...
                            (cos(gamma_p(p)*Z/Nx)+Bi0/(gamma_p(p))*sin(gamma_p
    (p)*Z/Nx))/Nx;
                    end
                end
            end
            W_mnp(m,n,p)=(omega_mnp(m,n,p)*norm_m(m)*norm_n(n)*norm_p(p))^(-1)
    *tripInt;
            count=count+1;
            waitbar(count/(eigValNo^3));
        end
    end
end
close(status);
toc

%% Steady State Temperature (phi)
%%%%%%%%%%%%%%%%%%%%%%%%%%%%%%%%%%%%%%%%%%%%%%%%%%%%%%%%%%%%%%%%%%%%%%%%%%%%%%%%
disp('Calculating Temperature...');
tic
status=waitbar(0,'Calculating Temperature...');
count=0;
for X=1:Ny
    for Y=1:Nz
        for Z=1:Nx
            tempSum=0;
            for m=1:eigValNo
                for n=1:eigValNo
                    for p=1:eigValNo
                        tempSum=tempSum+W_mnp(m,n,p).*...
                            cos(alpha_m(m)*(2*X/Ny-1)).*...
```

```
                                cos(beta_n(n)*(2*Y/Nz-1)).*...
                                (cos(gamma_p(p)*Z/Nx)+Bi0/(gamma_p(p))*sin(gamma_p
    (p)*Z/Nx));
                        end
                    end
                end
                count=count+1;
                waitbar(count/(Nx*Ny*Nz));
                tempMatr(X,Y,Z)=tempSum;
            end
        end
end

%%%%%%%%%
%%% The following calculation of temperature uses a meshgrid method
%%% which runs significantly faster than the summation method above;
%%% however, when the profiles are viewed in the movie output it is
%%% clear they are incorrect. Further investigation into meshgrid would
%%% be needed to consider its use here.
% xdiv = Nz;
% ydiv = Ny;
% zdiv = Nx;
% xvec = -1:1/xdiv:1;
% yvec = -1:1/ydiv:1;
% zvec =  0:1/zdiv:1;
% [Xf, Yf, Zf] = meshgrid(xvec, yvec, zvec);
% tempSum=0;
% for m=1:eigValNo
%     for n=1:eigValNo
%         for p=1:eigValNo
%             tempSum=W_mnp(m,n,p).*...
%                 cos(alpha_m(m).*Xf).*...
%                 cos(a*beta_n(n).*Yf).*...
```

```
%                   (cos(b*gamma_p(p).*Zf)+Bi0/(b*gamma_p(p))*sin(b*gamma_p(p).*
    Zf));
%               count=count+1;
%               waitbar(count/(eigValNo^3))
%           end
%       end
% end
% count=count+1;
%tempMatr=tempSum;
%%%%%%%%%
tempMatrAbs=tempMatr*temp_inf+temp_inf-273.15;

close(status);
if savVarChk==1
    save(['TempCalcVariablesE' num2str(DDSCATpol)],'tempMatr','tempMatrAbs','
    source',...
        'cnstrctynwfield','aveLayerEEfield','alpha_m','beta_n','gamma_p',...
        'norm_p','norm_m','norm_n','width','height','length');
end
toc

%% Temperature Movie
%%%%%%%%%%%%%%%%%%%%%%%%%%%%%%%%%%%%%%%%%%%%%%%%%%%%
% Generate movie visualizing temperature distribution while traveling along
    axis of particle
% including fields in the material only
if writeTempMovCheck == 1
    writerObj = VideoWriter(['AxialTempMovieE' num2str(DDSCATpol)]);
    open(writerObj);
    h=figure;
    for i=1:Nx
        if i==1
            surf(widthVec,heightVec,squeeze(tempMatrAbs(:,:,i)));
```

```
        axis ([widthVec(1) widthVec(Nz) heightVec(1) heightVec(Ny) min(min
(min(tempMatrAbs))) -0.00001*min(min(min(tempMatrAbs))) ...
            max(max(max(tempMatrAbs))) +0.00001*max(max(max(tempMatrAbs)))
...
            min(min(min(tempMatrAbs))) max(max(max(tempMatrAbs)))])
        colorbar('FontSize',20);
        title({'Temperature','Axial Position ( \mum): ' num2str(i*dspace*
10^6)},'FontSize',20)
        zlabel('(\circC)','FontSize',18);
        light('Position',[0 0 100],'Style','local');
        lighting phong
        shading interp
        xlabel('\mum','FontSize',26);
        ylabel('\mum','FontSize',26);
        set(gca,'FontSize',20,'GridLineStyle','-');
        set(gca,'DataAspectRatio', [1 1 0.1]);
        set(gca,'nextplot','replacechildren');
        set(gcf,'Renderer','zbuffer');
        frame=getframe(h);
        writeVideo(writerObj,frame);
    else
        surf(widthVec,heightVec,squeeze(tempMatrAbs(:,:,i)));
        light('Position',[0 0 100],'Style','local');
        lighting phong
        shading interp
        %colorbar('FontSize',20)
        title({'Temperature','Axial Position ( \mum): ' num2str(i*dspace*
10^6)},'FontSize',20)
        frame=getframe(h);
        writeVideo(writerObj,frame);
    end
end
hold off
```

```
    close(writerObj);
end

%% Average Temperature Plot
%%%%%%%%%%%%%%%%%%%%%%%%%%%%%%%%%%%%%%%%%%%%%
% This loop scans the geometry and extracts the average
% temperature per layer along the direction of propagation within just the
    particle
for i=1:Nx
    aveTempSum=0;
    cnt=0;
    for j=1:Ny
        for k=1:Nz
            aveTempSum=aveTempSum+tempMatr(j,k,i); % Sum Temp for each layer
    along DDSCAT x-axis
            if tempMatr(j,k,i) ~= 0
                cnt=cnt+1; % Tally number of dipoles per layer
            end
        end
    end
    aveLayerTemp(i,1)=i/Nx*length*10^6;
    aveLayerTemp(i,2)=aveTempSum/cnt*temp_inf+temp_inf-273.15; % Average
    EEField per layer
end

% Plot the average along the axis
if plotTempCheck == 1
    figure(10)
    axes('FontSize',38.0,'FontWeight','bold');
    plot(aveLayerTemp(:,1),aveLayerTemp(:,2),'k');
    xlabel('Position (\mum)','FontSize',38);
    ylabel('Temperature (^\circ C)','FontSize',38);
    xlim([min(aveLayerTemp(:,1)) max(aveLayerTemp(:,1))])
```

```
end
```

A.3 LabView: Laser Tweezer Brownian Temperature GUI

The following code was used to extract temperatures from optically trapped CdS NRs (Ch. 5).

Front Panel:

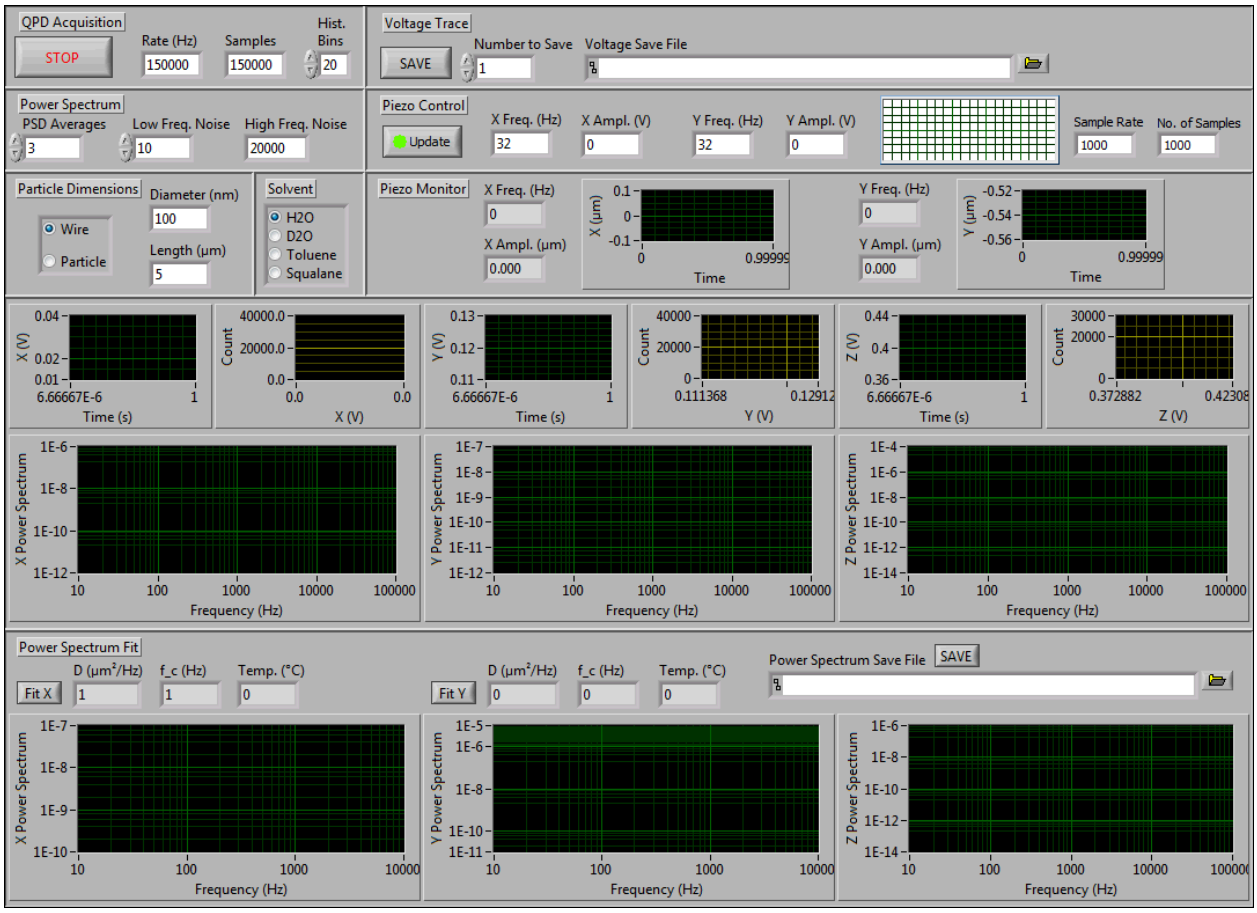

Block Diagram, Piezo Control Loop:

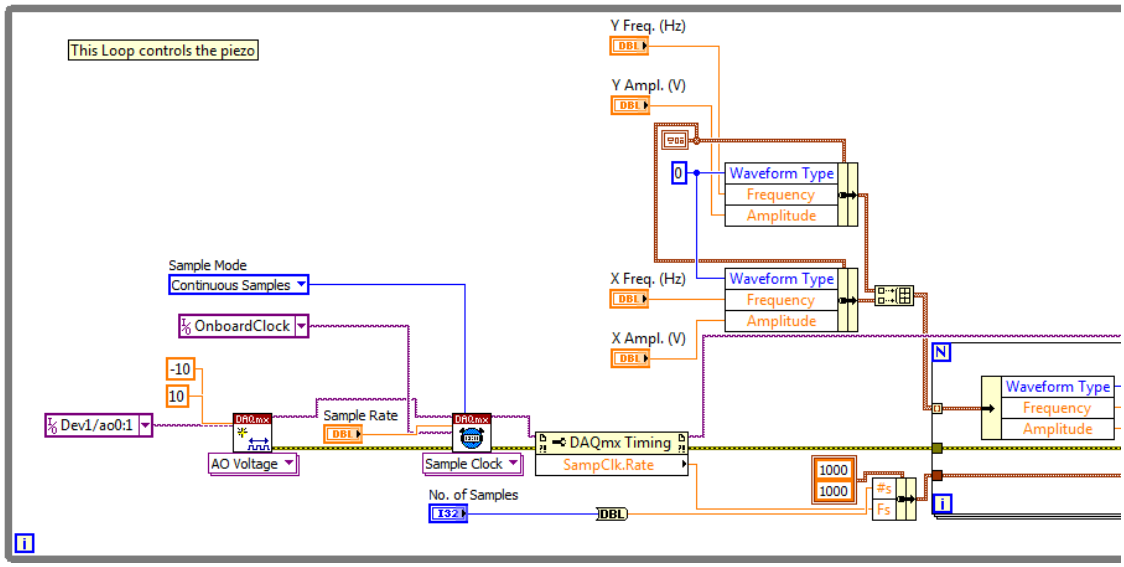

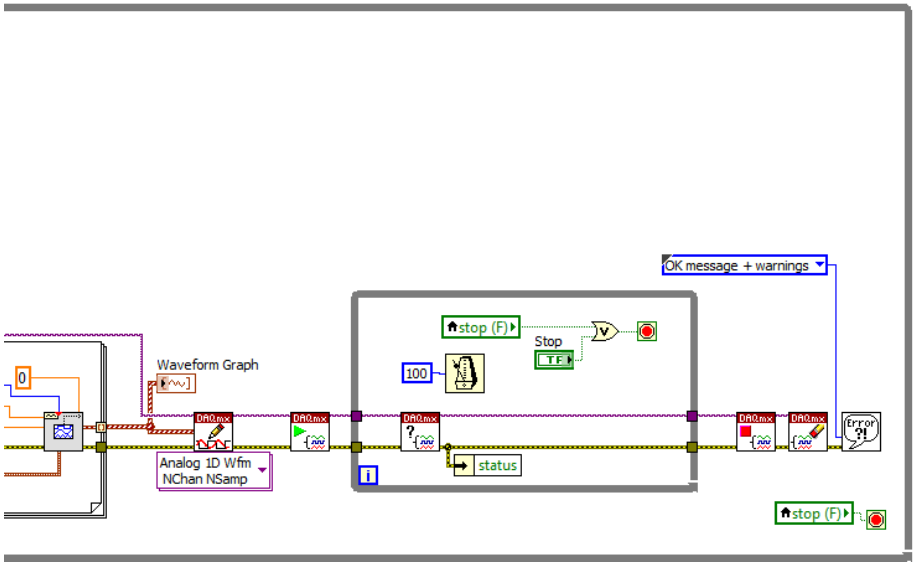

Block Diagram, QPD Loop:

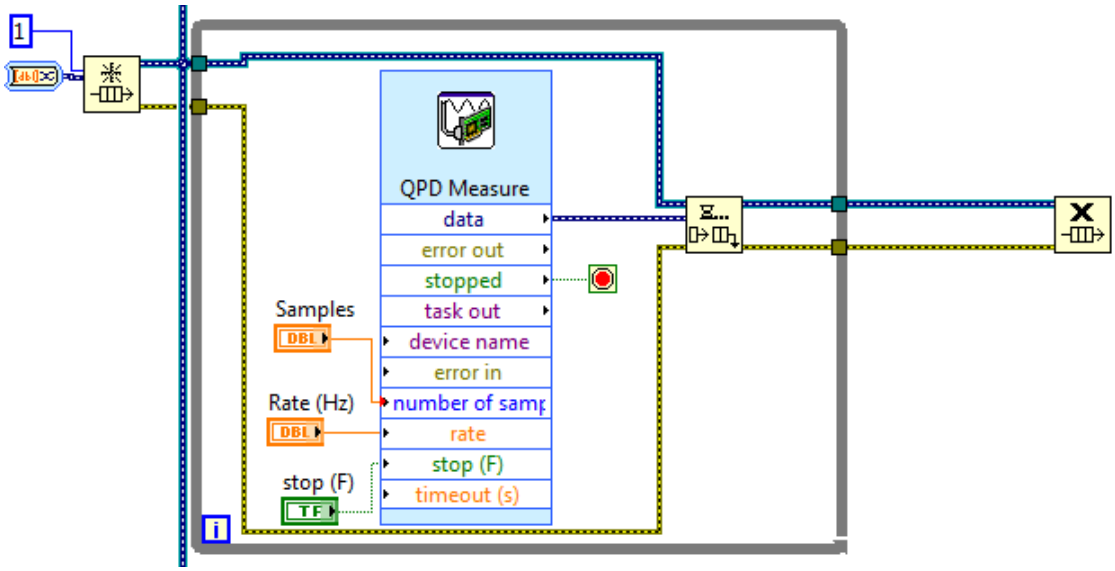

Block Diagram, Live Voltage Loop:

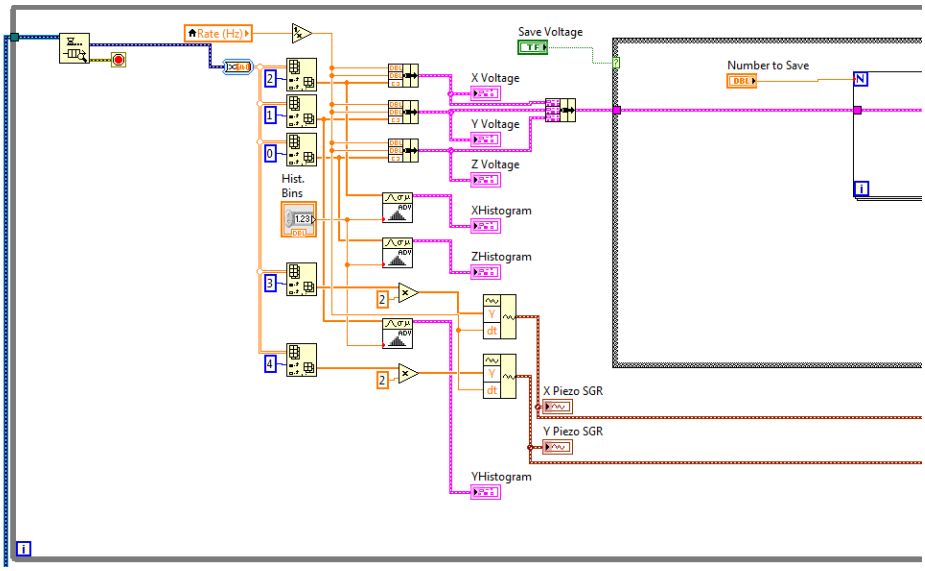

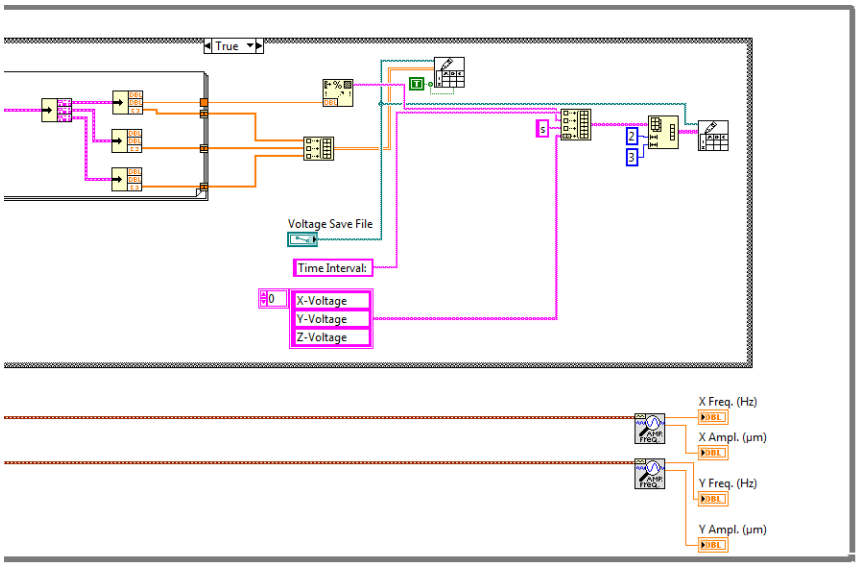

Block Diagram, Live PSD Loop:

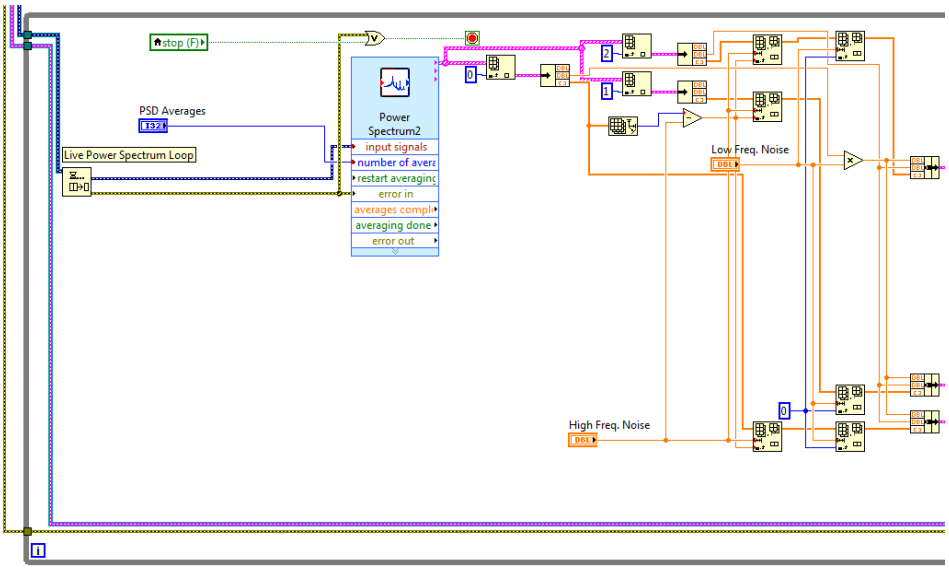

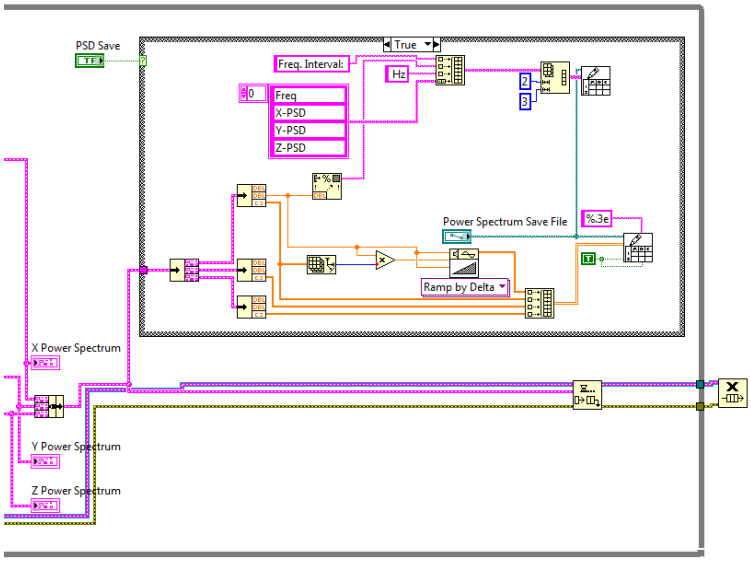

Block Diagram, Temperature Extraction Loop:

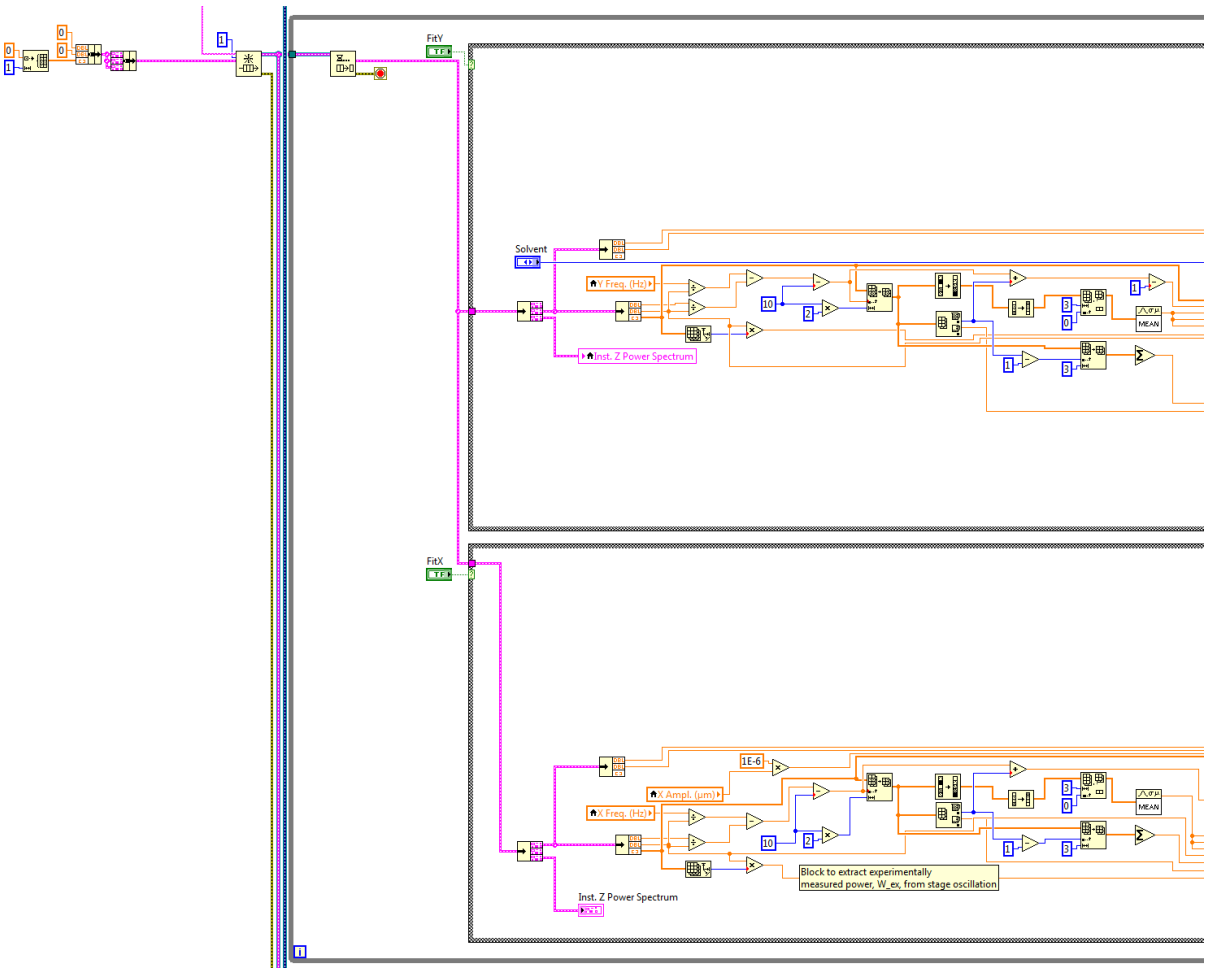

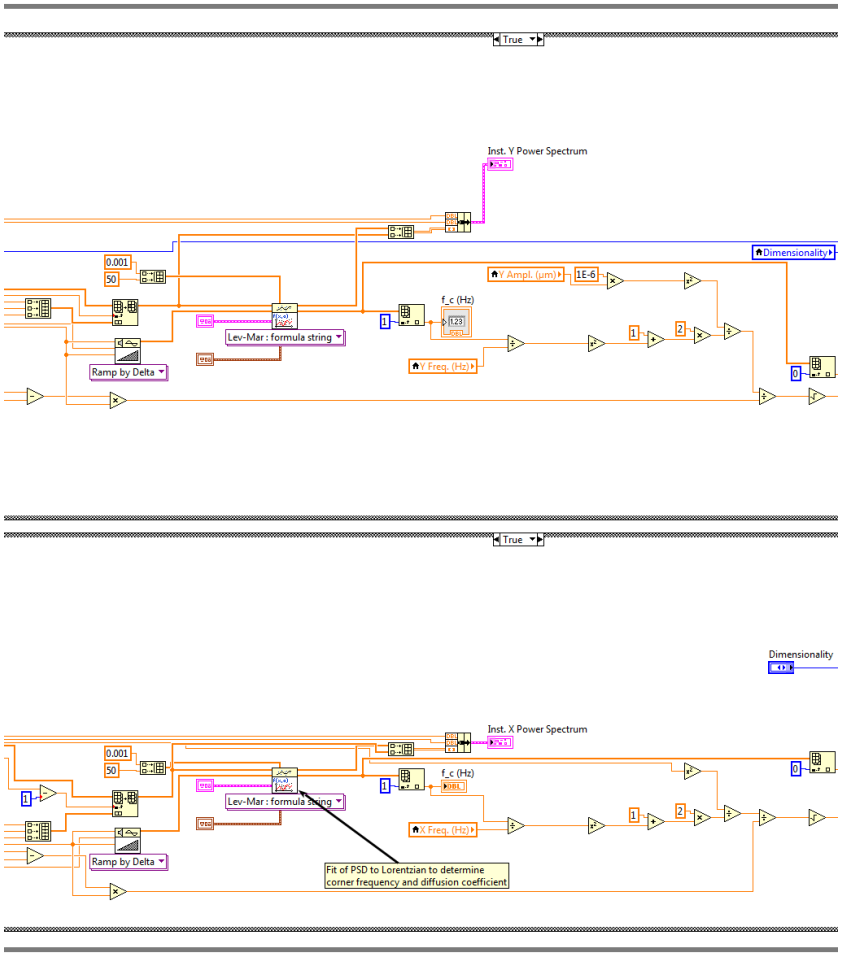
True
Inst. Y Power Spectrum
Dimensionality
0.001
50
Y Ampl. (µm)
1E-6
f_c (Hz)
Lev-Mar : formula string
Ramp by Delta
Y Freq. (Hz)
True
Dimensionality
Inst. X Power Spectrum
0.001
50
f_c (Hz)
Lev-Mar : formula string
Ramp by Delta
X Freq. (Hz)
Fit of PSD to Lorentzian to determine
corner frequency and diffusion coefficient

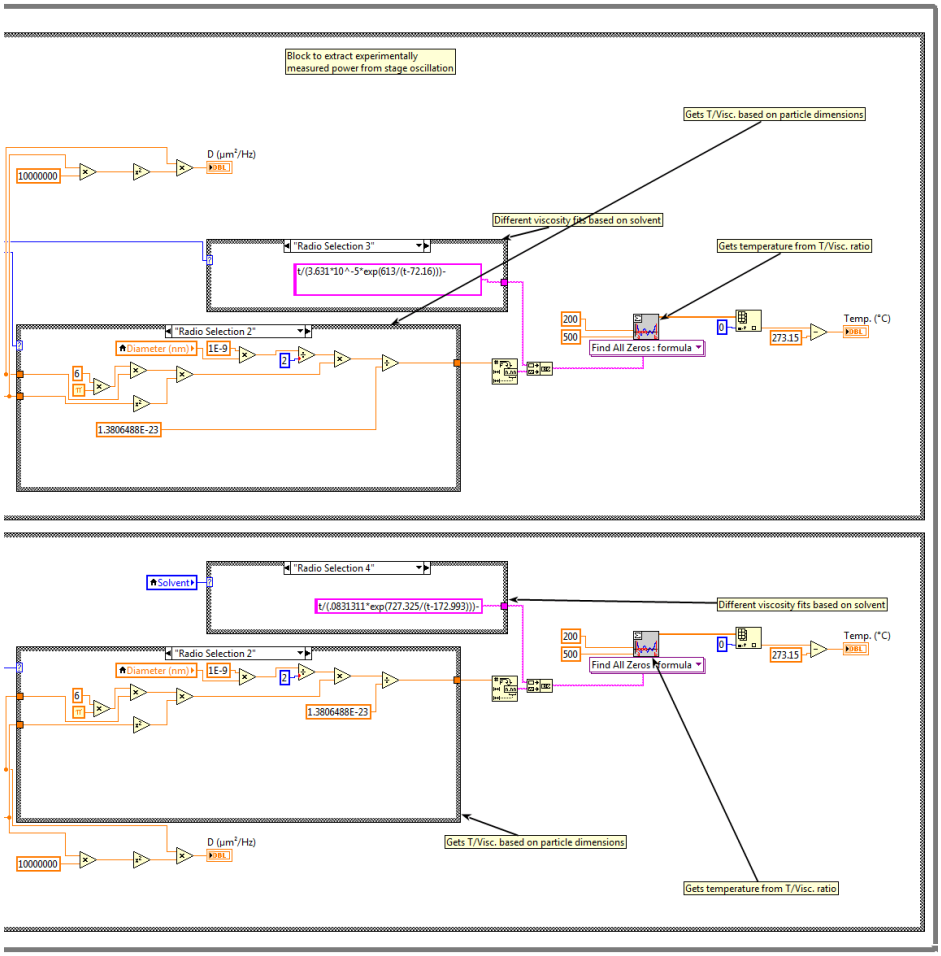
Block to extract experimentally measured power from stage oscillation
Gets T/Visc. based on particle dimensions
D (μm²/Hz)
10000000
Different viscosity fits based on solvent
"Radio Selection 3"
t/(3.631*10^-5*exp(613/(t-72.16)))-
Gets temperature from T/Visc. ratio
"Radio Selection 2"
Diameter (nm)
1E-9
6
1.3806488E-23
200
500
Find All Zeros : formula
0
273.15
Temp. (°C)
"Radio Selection 4"
Solvent
t/(.0831311*exp(727.325/(t-172.993)))-
Different viscosity fits based on solvent
Gets T/Visc. based on particle dimensions
Gets temperature from T/Visc. ratio

A.4 LabView: Cantilever APD Code

The following LabView code was used to monitor resonances in cantilevered CdS nanoribbons. The reader may notice the relatively simple block diagram compared to the stucture for the code in Appendix A.3. Certainly, the analysis is not as complex, but care was taken to keep the diagram simple for the benefit of future developers. This is the advice given by many expert programmers that I only later realized but encourage future lab members/readers to attempt from the beginning.

Front panel:

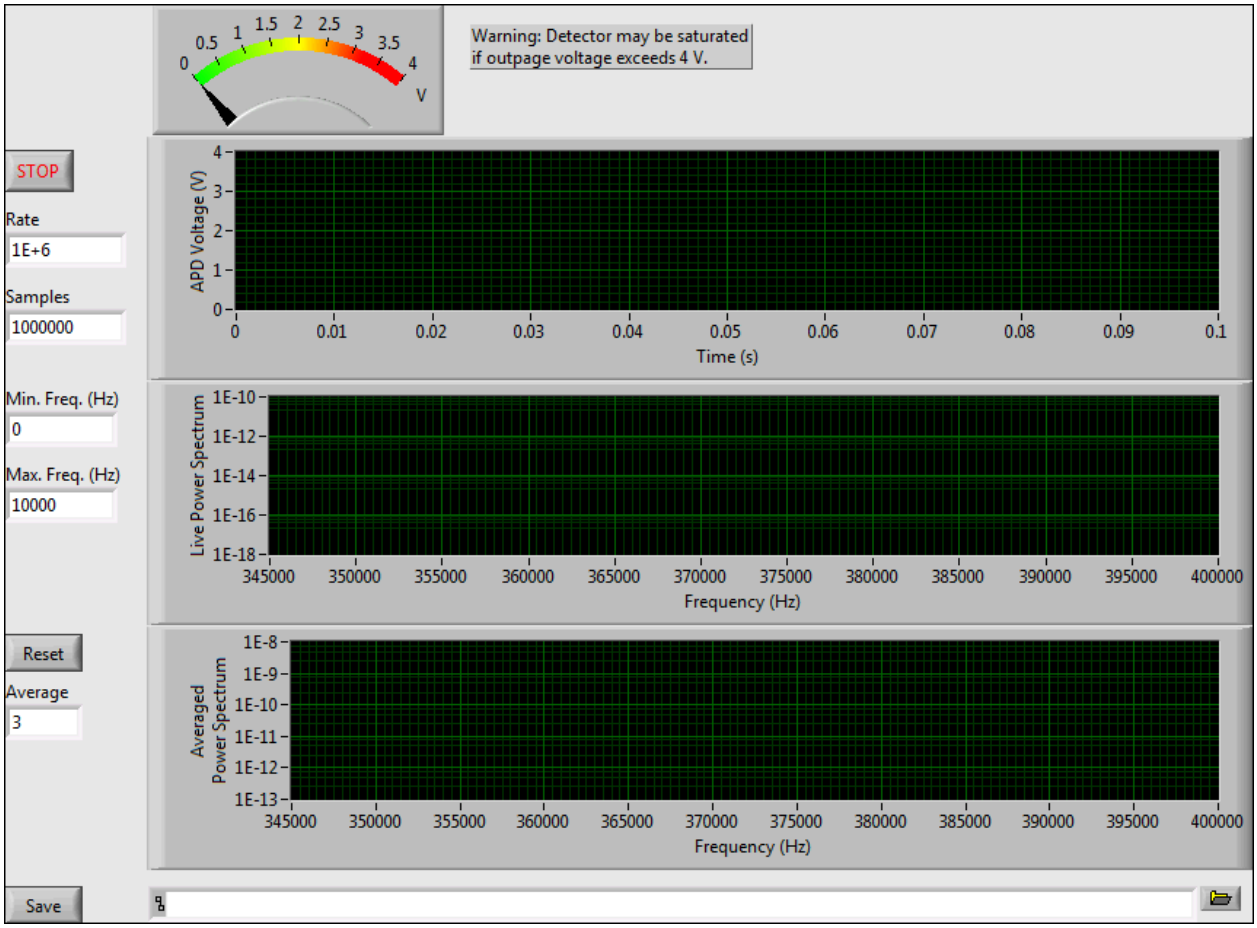

Block Diagram:

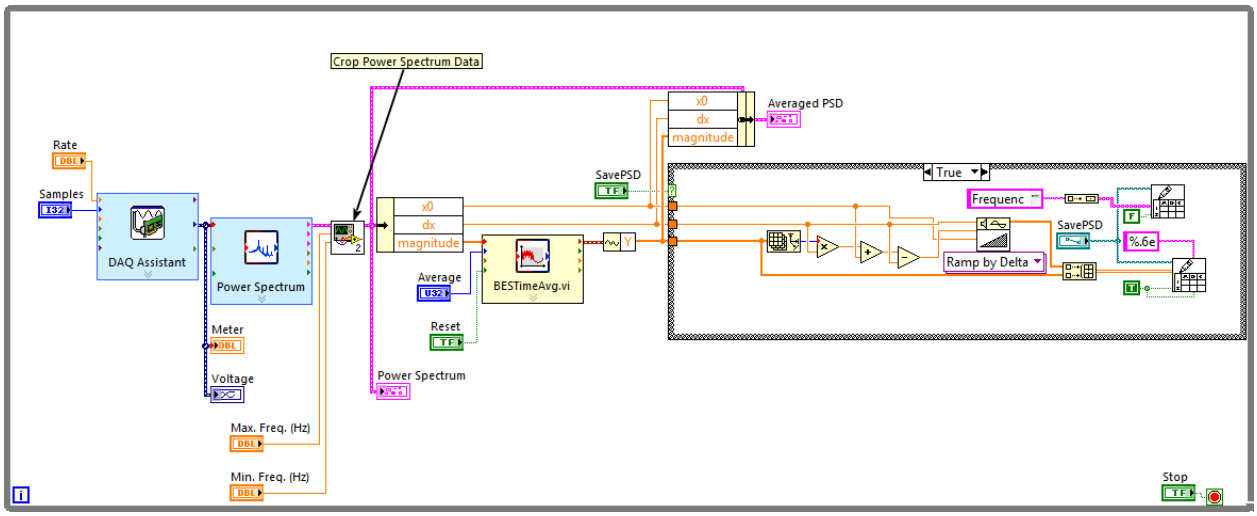

A.5 Python: Infinite Cylinder Heating

```
# This script is meant to calculate internal fields and temperature profiles
    for an
# infinite cylinder irradiated with monochromatic light
# Author(s): Bennett Smith
# Created: 27 Jul 2015
# Updated: 31 Jan 2016



#%% Retrieve functions from external libraries
#-------------------------------------------------------------------------
from math import pi, sqrt
from scipy.special import jv, hankel1
from scipy.integrate import quad
import sys
import scipy.optimize
import numpy as np
import matplotlib.pyplot as plt
from mpl_toolkits.mplot3d import axes3d
from matplotlib import cm



#%% Input
#-------------------------------------------------------------------------
mater = 0 # Material of cylinder; 0: Si
med = 3 # Medium; 0: Air, 1: H2O, 2: Solid Ar, 3: 4:1 MeOH:EtOH (See
    parameters below for MeOHEtOH)
diam = 536.0  # Cylinder diameter in nm
lambda_nm = 532  # Laser wavelength in nm
eigno = 14  # Number of eigenvalues;
irrad = 25.0  # Laser irradiance in kW/cm^2
T_inf = 298.0  # Ambient temperature (K)
press = 10.0 # Pressure in GPa
```

```
Nu = 0.32
checksave = 1 # Save images of source and temperature profiles, 0: no, 1: yes

#%% Constants
#-------------------------------------------------------------------------
radius = (diam/2)*1e-9  # Cylinder radius SI (m)
lambda_m = lambda_nm*1e-9  # Wavelength SI (m)
cvel = 299792458.0  # Velocity of light in vacuum SI (m s^-1)
epsilon_0 = 8.854188e-12  # Free Space permittivity SI (F m^-1=W s V^-2 m^-1)
mu_0 = 1.2566e-6  # Magnetic permeability SI (N A^-2)

#%% Functions
#-------------------------------------------------------------------------

def d_n(r, m, n, rho1, rho2):  # Internal field coefficient from Roder et al.
    Langmuir, 2012
    r=1
    out = ((jv(n+1, rho2*r)*hankel1(n, rho2*r) - jv(n, rho2*r)*hankel1(n+1,
    rho2*r))/ \
        (((n/rho2*r) - (n*m/rho1*r))*jv(n, rho1*r)*hankel1(n, rho2*r) \
        - jv(n, rho1*r)*hankel1(n+1, rho2*r) \
        + m*(jv(n+1, rho1*r)*hankel1(n, rho2*r))))*(1/m)
    return out

jsum = 25  # Sums are used in calculation of internal electric field
ksum = 25
def normField(r, th, rho1, rho2, jsum, ksum, e_0, m):  # Calculate internal
    fields
    e_1a = d_n(r, m, 0, rho1, rho2)*jv(0, rho1*r)

    e_1b = 0
    for jj in range(1, jsum):
```

```
        e_1b += ((-1)**(jj - 1))*d_n(r, m, 2*jj, rho1, rho2) * jv(2*jj, rho1*r
    ) * np.cos(2*jj*th)

    e_1c = 0
    for kk in range(1, ksum):
        e_1c += ((-1)**(kk - 1))*d_n(r, m, 2*kk-1, rho1, rho2)*jv(2*kk-1, rho1
    *r)*np.cos((2*kk - 1)*th)

    field = e_0*(e_1a - 2*e_1b - 2j*e_1c)

    out = (field.real ** 2 + field.imag ** 2)/(e_0 ** 2)

    return out

#%% Material Properties
#-------------------------------------------------------------------------
# Expand as needed for different materials
def N_Si(wl): # Values from luxpop.com
    return {
          532 : 4.150+0.0440j, # wavelength : complex index
          975 : 3.604+0.0025j,
          980 : 3.6014+0.0005763j,
          1064: 3.562+0.0010j,
    }[wl]

def N_air(wl):
    return{
        532 : 1.0002994,
        975 : 1.0002954,
        980 : 1.0002954,
        1064: 1.0002952,
    }[wl]
```

```
def N_H2O(wl): # Values from refractiveindex.info
    return {
        532 : 1.3337+0.0000000014992j,
        975 : 1.3270+0.0000034800j,
        980 : 1.3270+0.0000033620j,
        1064: 1.3260+0.0000051300j,
    }[wl]

def N_solAr(wl): # Solid argon refractive index at ~10GPa
    return {
        532 : 1.45
    }[wl]

def N_MethEth(wl,p): # High pressure refractive index of methanol:ethanol;
   from http://dx.doi.org/10.1063/1.351591
    h = 4.135667662 * 1e-15 # eV s
    dens = (1 - 1/(10.18 + 1) * np.log((10.18 + 1) * p / 0.778 + 1))**-1
    En_0 = 13.38 * dens**0.07
    En_d = 10.58 * dens**1.31
    n_MeEtOH = sqrt(1.0 + En_d * En_0 / (En_d ** 2.0 - h ** 2.0 * (cvel / (wl
   * 1e-9)) ** 2.0))
    # !! Warning !! Although these are the formulae provided, they do not seem
     to give correct values. Check reference for approximate value
    return 1.6

#%% Calculated constants
#-----------------------------------------------------------------------
# Select cylinder properties
if mater == 0:
    N_1 = N_Si(lambda_nm) # Material index; Check for value from material
    properties
    kappa_1 = 60.489 # 60.489 # Thermal conductivity
else:
```

```
    sys.exit("Error: Unknown material")
# Select medium properties
if med == 0:    # air
    N_2 = N_air(lambda_nm) # Complex refractive index of medium
    kappa_2 = 0.024 # Thermal conductivity
elif med == 1: # H2O
    N_2 = N_H2O(lambda_nm)
    kappa_2 = 0.58
elif med == 2: # Solid Ar
    N_2 = N_solAr(lambda_nm)
    kappa_2 = 11.0
elif med == 3: #MeOH/EtOH
    N_2 = N_MethEth(lambda_nm,press)
    kappa_2 = 2.0 # From http://dx.doi.org/10.1063/1.4922632
else:
    sys.exit("Error: Unknown medium")
sigma = 4*pi*N_1.real*N_1.imag/(lambda_m*mu_0*cvel)  # Optical conductivity
Biot = (kappa_2/kappa_1)*(Nu/2)

#print Biot
#print N_2
#sys.exit() # For debugging purposes

# The following constants will be used in external functions
rho1 = 2*pi*N_1*radius/lambda_m
rho2 = 2*pi*N_2*radius/lambda_m
m = N_1/N_2
E_0 = sqrt((2/(cvel*epsilon_0*N_2.real))*irrad*1.e7)  # Incident electric
    field
srcConstant = sigma * radius**2 * E_0**2/(2 * kappa_1 * T_inf)

#%% Source
#-------------------------------------------------------------------------
```

```
N_rth = 150
th = np.linspace(0, 2*pi, N_rth)
r = np.linspace(0, 1, N_rth)
TH, R = np.meshgrid(th, r)
X = R * np.cos(TH)
Y = R * np.sin(TH)
Xnm = X * radius * 10**9
Ynm = Y * radius * 10**9
fieldMtrx = normField(R, TH, rho1, rho2, jsum, ksum, E_0, m)

# Plot source - 2D
figSrc = plt.figure()
ax = figSrc.add_subplot(111)
plt.contourf(Ynm, -Xnm, fieldMtrx, 900, cmap=cm.coolwarm)
ax.axis('image') # Scales image correctly and removes excess whitespace
ax.set_xlabel('\nX (nm)')
ax.set_ylabel('\nY (nm)')
plt.colorbar(fraction=0.15)

# Plot source - 3D
#fig = plt.figure()
#ax = fig.add_subplot(111, projection='3d')
#ax.plot_surface(Xnm, Ynm, fieldMtrx, rstride=2, cstride=1, cmap=cm.coolwarm,
    linewidth=0)
#ax.set_xlabel('\nX (nm)')
#ax.set_ylabel('\nY (nm)')
#ax.set_zlabel('EE*/E$_{0}$$^{2}$')
#ax.view_init(elev=90., azim=0)

# Save figure
if checksave == 1:
    filename = ('sourced' + str(diam) + 'lamdba' + str(lambda_nm) +
        'mat' + str(mater) + 'med' + str(med) + '.jpg')
```

```
    plt.savefig(filename, format='jpg', dpi=300)


#%% Find eigenvalues
#-----------------------------------------------------------------------
step = pi / 2
a = (eigno, eigno)
Ljk = np.zeros(a)
xplot = np.linspace(0, 20, 500)
fig2 = plt.figure()
for k in range(eigno):
    count = 0
    test = 0.05 #0.1
    if k > 1:
        test = Ljk[0, k - 1] + step
    def FL(x):
        if k == 0:
            return - x * jv(k + 1, x) + Biot * jv(k, x) # From Langmuir Paper
        else:
            return (k/x) * jv(k, x) - jv(k + 1, x) + Biot * jv(k, x) # From
   Langmuir Paper
    yplot = FL(xplot)
    if k >= 0: # Change this value to plot different eigenvalue functions
        plt.plot(xplot, yplot)
    while Ljk[eigno - 1, k] == 0: # Find roots until Ljk is filled
        xcheck = scipy.optimize.fsolve(FL, test)
        if Ljk[0, k] == 0 and xcheck > 0.001: # Assign Initial Eigenvalue;
   minumum set to .001
            if xcheck > k * 4 and k > 0:
                test = xcheck - 3 * step
            else:
                Ljk[count, k] = xcheck
                count = count + 1
```

```
        elif Ljk[0, k] != 0 and xcheck > Ljk[count - 1, k] + 6: # Check for
    overshoot for subsequent eigenvalue
            test = xcheck - 3 * step
        elif Ljk[0, k] != 0 and xcheck > Ljk[count - 1, k] + 1: # Check for
    repeated eigenvalue and assign
            Ljk[count, k] = xcheck
            count = count + 1
        test = test + step

# Save eigenvalue functions figure
#plt.savefig('EigenvalueFxns')

#%% Calculate Norms
#-------------------------------------------------------------------------
Njk = np.zeros(a)
for j in range(eigno):
    for k in range(eigno):
        def FN(x):
            return x * jv(k, Ljk[j,k] * x) * jv(k, Ljk[j,k] * x)
        Njk[j, k] = quad(FN, 0, 1)[0]

#%% Build constant matrix
#-------------------------------------------------------------------------
Bjk = 1 / (Ljk**2 * Njk)

#%% Calculate Ajk coefficient
#-------------------------------------------------------------------------
def FA(x,t):
    return (2 / pi) * Bjk[j, k] * x * jv(k, Ljk[j, k] * x) \
        * np.cos(k * t) * normField(x, t, rho1, rho2, jsum, ksum, E_0, m)

Ajk = np.zeros(a)
for j in range(eigno):
```

```
    for k in range(eigno):
        Afxn = srcConstant * FA(R,TH)
        I = np.zeros(N_rth)
        for i in range(N_rth):
            I[i] = np.trapz(Afxn[i,:], r) # Trapezoidal method solves in
    reasonable amount of time
        Ajk[j, k] = np.trapz(I, th)

# Unable to get dblquad to solve in reasonable time lengths, even though
    matlab does
#for j in range(eigno):
#    for k in range(eigno):
#        Ajk[j, k] = srcConstant * dblquad(FA, 0, 1, lambda x: 0, lambda x: pi
    )[0]
#        print(Ajk[j,k])

#%% Calculate temperature
#-----------------------------------------------------------------------
phi = np.zeros((N_rth, N_rth))
for j in range(eigno):
    for k in range(eigno):
        phi += (2 / pi) * Ajk[j, k] * jv(k, Ljk[j, k] * R) * np.cos(k * TH)

tempK = phi * T_inf + T_inf
tempC = tempK-273

#%% Plot Temperature - 2D
figTemp = plt.figure()
ax = figTemp.add_subplot(111)
plt.contourf(Ynm, -Xnm, tempC, 900, cmap=cm.coolwarm)
plt.colorbar(format='%.3f')
ax.axis('image') # Scales image correctly and removes excess whitespace
ax.set_xlabel('\nX (nm)')
```

```
ax.set_ylabel('\nY (nm)')

# Plot Temperature - 3D
#figTemp = plt.figure()
#ax = figTemp.add_subplot(111, projection='3d')
#ax.plot_surface(Xnm, Ynm, tempC, rstride=2, cstride=1, cmap=cm.coolwarm,
    linewidth=0)
#ax.set_xlabel('\nX (nm)')
#ax.set_ylabel('\nY (nm)')
#ax.zaxis.set_major_formatter(plt.FormatStrFormatter('%.3f'))
#ax.set_zlabel('\n\n' + 'Temperature (C)', linespacing = 1.8)
#ax.tick_params(axis='z',pad=10)

# Save Temperature Figure
if checksave == 1:
    filename = ('tempd' + str(diam) + 'lambda' + str(lambda_nm) +
        'mat' + str(mater) + 'med' + str(med) + '.jpg')
    plt.savefig(filename, format='jpg', dpi=300)
```

BIBLIOGRAPHY

1. Ashkin, A., Dziedzic, J. M., Bjorkholm, J. E. & Chu, S. Observation of a single-beam gradient force optical trap for dielectric particles. *Optics Letters* **11,** 288 (1986).
2. Pringsheim, P. Two Observations about the Difference between Luminescence and Thermal radiation. *Zeitschrift Fur Physik* **57,** 739–746 (1929).
3. Landau, L. D. On the thermodynamics of photoluminescence. *J. Phys. U.S.S.R.* **10,** 503 (1946).
4. Ruan, X. L., Rand, S. C. & Kaviany, M. Entropy and efficiency in laser cooling of solids. *Physical Review B* **75,** 214304 (2007).
5. Roder, P. B., Smith, B. E., Zhou, X., Crane, M. J. & Pauzauskie, P. J. Laser refrigeration of hydrothermal nanocrystals in physiological media. *Proceedings of the National Academy of Sciences* **112,** 15024–15029 (2015).
6. Zhang, J., Li, D., Chen, R. & Xiong, Q. Laser cooling of a semiconductor by 40 kelvin. *Nature* **493,** 504–508 (2013).
7. Epstein, R. I., Buchwald, M. I., Edwards, B. C., Gosnell, T. R. & Mungan, C. E. Observation of laser-induced fluorescent cooling of a solid. *Nature* **377,** 500–503 (1995).
8. Bowman, S. R. & Mungan, C. E. New materials for optical cooling. *Applied Physics B* **71,** 807–811 (2000).
9. Bigotta, S., Parisi, D., Bonelli, L., Toncelli, A., Lieto, A. D. & Tonelli, M. Laser cooling of a Yb^{3+}-doped BaY_2F_8 single crystal. *Optical Materials. Proceedings of the 1st International Workshop on Photoluminescence in Rare Earths: Photonic Materials and Devices* **28,** 1321–1324 (2006).
10. Epstein, R. I., Brown, J. J., Edwards, B. C. & Gibbs, A. Measurements of optical refrigeration in ytterbium-doped crystals. *Journal of Applied Physics* **90,** 4815–4819 (2001).
11. Melgaard, S. D., Albrecht, A. R., Hehlen, M. P. & Sheik-Bahae, M. Solid-state optical refrigeration to sub-100 Kelvin regime. *Scientific Reports* **6,** 20380 (2016).
12. Seletskiy, D. V., Hehlen, M. P., Epstein, R. I. & Sheik-Bahae, M. Cryogenic optical refrigeration. *Advances in Optics and Photonics* **4,** 78–107 (2012).
13. Hoyt, C. W., Sheik-Bahae, M., Epstein, R. I., Edwards, B. C. & Anderson, J. E. Observation of Anti-Stokes Fluorescence Cooling in Thulium-Doped Glass. *Physical Review Letters* **85,** 3600–3603 (2000).
14. Fernandez, J., Garcia-Adeva, A. J. & Balda, R. Anti-Stokes Laser Cooling in Bulk Erbium-Doped Materials. *Physical Review Letters* **97,** 033001 (2006).
15. Hehlen, M. P. *Crystal-field effects in fluoride crystals for optical refrigeration* **7614** (2010), 761404–761404–12.

16. Hüfner, S. *Optical Spectra of Transparent Rare Earth Compounds* 38–114 (Academic Press, 1978).

17. Lojpur, V., Nikolić, G. & Dramićanin, M. D. Luminescence thermometry below room temperature via up-conversion emission of Y_2O_3:Yb^{3+},Er^{3+} nanophosphors. *Journal of Applied Physics* **115,** 203106 (2014).

18. Finkeißen, E., Potemski, M., Wyder, P., Viña, L. & Weimann, G. Cooling of a semiconductor by luminescence up-conversion. *Applied Physics Letters* **75,** 1258–1260 (1999).

19. Hasselbeck, M. P., Sheik-Bahae, M. & Epstein, R. I. *Effect of high carrier density on luminescence thermometry in semiconductors Proceedings of SPIE* **6461** (2007), 646107.

20. Reece, P. J., Toe, W. J., Wang, F., Paiman, S., Gao, Q., Tan, H. H. & Jagadish, C. Characterization of Semiconductor Nanowires Using Optical Tweezers. *Nano Letters* **11,** 2375–2381 (2011).

21. Berg-Sørensen, K. & Flyvbjerg, H. Power spectrum analysis for optical tweezers. *Review of Scientific Instruments* **75,** 594–612 (2004).

22. Roder, P. B., Manandhar, S., Smith, B. E., Zhou, X., Shutthanandan, V. S. & Pauzauskie, P. J. Photothermal Superheating of Water with Ion-Implanted Silicon Nanowires. *Advanced Optical Materials* **3,** 1362–1367 (2015).

23. Tolić-Nørrelykke, S. F., Schäffer, E., Howard, J., Pavone, F. S., Jülicher, F. & Flyvbjerg, H. Calibration of optical tweezers with positional detection in the back focal plane. *Review of Scientific Instruments* **77,** 103101 (2006).

24. Huang, Z., Geyer, N., Werner, P., de Boor, J. & Gösele, U. Metal-Assisted Chemical Etching of Silicon: A Review. *Advanced Materials* **23,** 285–308 (2011).

25. Roder, P. B., Smith, B. E., Davis, E. J. & Pauzauskie, P. J. Photothermal Heating of Nanowires. *The Journal of Physical Chemistry C* **118,** 1407–1416 (2014).

26. Kyrsting, A., Bendix, P. M., Stamou, D. G. & Oddershede, L. B. Heat Profiling of Three-Dimensionally Optically Trapped Gold Nanoparticles using Vesicle Cargo Release. *Nano Letters* **11,** 888–892 (2011).

27. Fujii, M., Nishimura, N., Fumon, H., Hayashi, S., Kovalev, D., Goller, B. & Diener, J. Dynamics of photosensitized formation of singlet oxygen by porous silicon in aqueous solution. *Journal of Applied Physics* **100,** 124302–124302–5 (2006).

28. Xiao, L., Gu, L., Howell, S. B. & Sailor, M. J. Porous Silicon Nanoparticle Photosensitizers for Singlet Oxygen and Their Phototoxicity against Cancer Cells. *ACS Nano* **5,** 3651–3659 (2011).

29. Kovalev, D. & Fujii, M. Silicon Nanocrystals: Photosensitizers for Oxygen Molecules. *Advanced Materials* **17,** 2531–2544 (2005).

30. Fujii, M., Kovalev, D., Goller, B., Minobe, S., Hayashi, S. & Timoshenko, V. Y. Time-resolved photoluminescence studies of the energy transfer from excitons confined in Si nanocrystals to oxygen molecules. *Physical Review B* **72,** 165321 (2005).

31. Dougherty, T. J., Gomer, C. J., Henderson, B. W., Jori, G., Kessel, D., Korbelik, M., Moan, J. & Peng, Q. Photodynamic Therapy. *Journal of the National Cancer Institute* **90,** 889–905 (1998).

32. Dolmans, D. E. J. G. J., Fukumura, D. & Jain, R. K. Photodynamic therapy for cancer. *Nature Reviews Cancer* **3,** 380–387 (2003).

33. Robertson, C. A., Evans, D. H. & Abrahamse, H. Photodynamic therapy (PDT): A short review on cellular mechanisms and cancer research applications for PDT. *Journal of Photochemistry and Photobiology B: Biology* **96,** 1–8 (2009).

34. Bonnett, R. Photosensitizers of the porphyrin and phthalocyanine series for photodynamic therapy. *Chemical Society Reviews* **24,** 19 (1995).

35. Gilson, D., Ash, D., Driver, I., Feather, J. W. & Brown, S. Therapeutic ratio of photodynamic therapy in the treatment of superficial tumours of skin and subcutaneous tissues in man. *British Journal of Cancer* **58,** 665–667 (1988).

36. Allison, R. & Sibata, C. Oncologic photodynamic therapy photosensitizers: A clinical review. *Photodiagnosis and Photodynamic Therapy* **7,** 61–75 (2010).

37. Lukyanov, A. N., Gao, Z. & Torchilin, V. P. Micelles from polyethylene glycol/phosphatidylethanolamine conjugates for tumor drug delivery. *Journal of Controlled Release. Proceedings of the Second International Symposium on Tumor Targeted Delivery Systems* **91,** 97–102 (2003).

38. Sharma, A. & Sharma, U. S. Liposomes in drug delivery: Progress and limitations. *International Journal of Pharmaceutics* **154,** 123–140 (1997).

39. Bhirde, A. A. *et al.* Targeted Killing of Cancer Cells in Vivo and in Vitro with EGF-Directed Carbon Nanotube-Based Drug Delivery. *ACS Nano* **3,** 307–316 (2009).

40. Vivero-Escoto, J. L., Slowing, I. I., Wu, C.-W. & Lin, V. S.-Y. Photoinduced Intracellular Controlled Release Drug Delivery in Human Cells by Gold-Capped Mesoporous Silica Nanosphere. *Journal of the American Chemical Society* **131,** 3462–3463 (2009).

41. Lu, J., Liong, M., Li, Z., Zink, J. I. & Tamanoi, F. Biocompatibility, Biodistribution, and Drug-Delivery Efficiency of Mesoporous Silica Nanoparticles for Cancer Therapy in Animals. *Small* **6,** 1794–1805 (2010).

42. Secret, E. *et al.* Two-Photon Excitation of Porphyrin-Functionalized Porous Silicon Nanoparticles for Photodynamic Therapy. *Advanced Materials* **26,** 7643–7648 (2014).

43. Huang, Y.-F., Zhang, M., Zhao, L.-B., Feng, J.-M., Wu, D.-Y., Ren, B. & Tian, Z.-Q. Activation of Oxygen on Gold and Silver Nanoparticles Assisted by Surface Plasmon Resonances. *Angewandte Chemie International Edition* **53,** 2353–2357 (2014).

44. Zhao, T., Shen, X., Li, L., Guan, Z., Gao, N., Yuan, P., Yao, S. Q., Xu, Q.-H. & Xu, G. Q. Gold nanorods as dual photo-sensitizing and imaging agents for two-photon photodynamic therapy. *Nanoscale* **4,** 7712–7719 (2012).

45. Llansola Portolés, M. J., David Gara, P. M., Kotler, M. L., Bertolotti, S., San Román, E., Rodríguez, H. B. & Gonzalez, M. C. Silicon Nanoparticle Photophysics and Singlet Oxygen Generation. *Langmuir* **26,** 10953–10960 (2010).

46. Gross, E., Kovalev, D., Knzner, N., Diener, J., Koch, F., Timoshenko, V. Y. & Fujii, M. Spectrally resolved electronic energy transfer from silicon nanocrystals to molecular oxygen mediated by direct electron exchange. *Physical Review B* **68,** 115405 (2003).

47. Park, J.-H., Gu, L., von Maltzahn, G., Ruoslahti, E., Bhatia, S. N. & Sailor, M. J. Biodegradable luminescent porous silicon nanoparticles for in vivo applications. *Nature Materials* **8,** 331–336 (2009).

48. Champion, J. A. & Mitragotri, S. Role of target geometry in phagocytosis. *Proceedings of the National Academy of Sciences of the United States of America* **103,** 4930–4934 (2006).

49. Shi, X., von dem Bussche, A., Hurt, R. H., Kane, A. B. & Gao, H. Cell entry of one-dimensional nanomaterials occurs by tip recognition and rotation. *Nature Nanotechnology* **6,** 714–719 (2011).

50. Chithrani, B. D., Ghazani, A. A. & Chan, W. C. W. Determining the Size and Shape Dependence of Gold Nanoparticle Uptake into Mammalian Cells. *Nano Letters* **6,** 662–668 (2006).

51. Barua, S., Yoo, J.-W., Kolhar, P., Wakankar, A., Gokarn, Y. R. & Mitragotri, S. Particle shape enhances specificity of antibody-displaying nanoparticles. *Proceedings of the National Academy of Sciences* **110,** 3270–3275 (2013).

52. Roder, P. B., Pauzauskie, P. J. & Davis, E. J. Nanowire Heating by Optical Electromagnetic Irradiation. *Langmuir* **28,** 16177–16185 (2012).

53. Pasparakis, G. Light-Induced Generation of Singlet Oxygen by Naked Gold Nanoparticles and its Implications to Cancer Cell Phototherapy. *Small* **9,** 4130–4134 (2013).

54. Gao, L., Liu, R., Gao, F., Wang, Y., Jiang, X. & Gao, X. Plasmon-Mediated Generation of Reactive Oxygen Species from Near-Infrared Light Excited Gold Nanocages for Photodynamic Therapy in Vitro. *ACS Nano,* 140703192109006 (2014).

55. Kachynski, A. V., Pliss, A., Kuzmin, A. N., Ohulchanskyy, T. Y., Baev, A., Qu, J. & Prasad, P. N. Photodynamic therapy by in situ nonlinear photon conversion. *Nature Photonics* **8,** 455–461 (2014).

56. Wang, X., Liu, K., Yang, G., Cheng, L., He, L., Liu, Y., Li, Y., Guo, L. & Liu, Z. Near-infrared light triggered photodynamic therapy in combination with gene therapy using upconversion nanoparticles for effective cancer cell killing. *Nanoscale* **6,** 9198–9205 (2014).

57. Vankayala, R., Sagadevan, A., Vijayaraghavan, P., Kuo, C.-L. & Hwang, K. C. Metal Nanoparticles Sensitize the Formation of Singlet Oxygen. *Angewandte Chemie International Edition* **50,** 10640–10644 (2011).

58. Kovalev, D., Gross, E., Knzner, N., Koch, F., Timoshenko, V. Y. & Fujii, M. Resonant Electronic Energy Transfer from Excitons Confined in Silicon Nanocrystals to Oxygen Molecules. *Physical Review Letters* **89,** 137401 (2002).

59. Skovsen, E., Snyder, J. W., Lambert, J. D. C. & Ogilby, P. R. Lifetime and Diffusion of Singlet Oxygen in a Cell. *The Journal of Physical Chemistry B* **109,** 8570–8573 (2005).

60. Flors, C., Fryer, M. J., Waring, J., Reeder, B., Bechtold, U., Mullineaux, P. M., Nonell, S., Wilson, M. T. & Baker, N. R. Imaging the production of singlet oxygen in vivo using a new fluorescent sensor, Singlet Oxygen Sensor Green. *Journal of Experimental Botany* **57,** 1725–1734 (2006).

61. Ragàs, X., Jiménez-Banzo, A., Sànchez-García, D., Batllori, X. & Nonell, S. Singlet oxygen photosensitisation by the fluorescent probe Singlet Oxygen Sensor Green. *Chemical Communications,* 2920 (2009).

62. Shen, H. *et al.* Cooperative, Nanoparticle-Enabled Thermal Therapy of Breast Cancer. *Advanced Healthcare Materials* **1,** 84–89 (2012).

63. Su, Y. *et al.* Silicon nanowire-based therapeutic agents for in vivo tumor near-infrared photothermal ablation. *Journal of Materials Chemistry B* **2,** 2892–2898 (2014).

64. Hu, S., Shaner, M. R., Beardslee, J. A., Lichterman, M., Brunschwig, B. S. & Lewis, N. S. Amorphous TiO2 coatings stabilize Si, GaAs, and GaP photoanodes for efficient water oxidation. *Science* **344,** 1005–1009 (2014).

65. Nakayama, Y., Pauzauskie, P. J., Radenovic, A., Onorato, R. M., Saykally, R. J., Liphardt, J. & Yang, P. Tunable nanowire nonlinear optical probe. *Nature* **447,** 1098–1101 (2007).

66. Franken, P. A., Hill, A. E., Peters, C. W. & Weinreich, G. Generation of Optical Harmonics. *Physical Review Letters* **7,** 118–119 (1961).

67. Chang, Z., Rundquist, A., Wang, H., Murnane, M. M. & Kapteyn, H. C. Generation of Coherent Soft X Rays at 2.7 nm Using High Harmonics. *Physical Review Letters* **79,** 2967–2970 (1997).

68. Boyd, R. W. *Nonlinear Optics (Third Edition)* (ed Boyd, R. W.) 1–67 (Academic Press, Burlington, 2008).

69. Giordmaine, J. A. & Miller, R. C. Tunable Coherent Parametric Oscillation in $LiNbO_3$ at Optical Frequencies. *Physical Review Letters* **14,** 973–976 (1965).

70. Kaiser, W. & Garrett, C. G. B. Two-Photon Excitation in CaF_2:Eu^{2+}. *Physical Review Letters* **7,** 229–231 (1961).

71. Lu, Z., Karakoti, A., Velarde, L., Wang, W., Yang, P., Thevuthasan, S. & Wang, H.-f. Dissociative Binding of Carboxylic Acid Ligand on Nanoceria Surface in Aqueous Solution: A Joint In Situ Spectroscopic Characterization and First-Principles Study. *The Journal of Physical Chemistry C* **117,** 24329–24338 (2013).

72. Thomas, G., van Voskuilen, J., Gerritsen, H. C. & Sterenborg, H. J. C. M. Advances and challenges in label-free nonlinear optical imaging using two-photon excitation fluorescence and second harmonic generation for cancer research. *Journal of Photochemistry and Photobiology B: Biology* **141,** 128–138 (2014).

73. Hsieh, M.-C., Chien, C.-H., Chang, C.-C. & Chang, T.-C. Aggregation induced photodynamic therapy enhancement based on linear and nonlinear excited FRET of fluorescent organic nanoparticles. *Journal of Materials Chemistry B* **1,** 2350–2357 (2013).

74. Garmire, E. Nonlinear optics in daily life. *Optics Express* **21,** 30532 (2013).

75. Roke, S. & Gonella, G. Nonlinear Light Scattering and Spectroscopy of Particles and Droplets in Liquids. *Annual Review of Physical Chemistry* **63,** 353–378 (2012).

76. Johnson, J. C., Yan, H., Schaller, R. D., Petersen, P. B., Yang, P. & Saykally, R. J. Near-Field Imaging of Nonlinear Optical Mixing in Single Zinc Oxide Nanowires. *Nano Letters* **2,** 279–283 (2002).

77. Johnson, J. C., Yan, H., Yang, P. & Saykally, R. J. Optical Cavity Effects in ZnO Nanowire Lasers and Waveguides. *The Journal of Physical Chemistry B* **107,** 8816–8828 (2003).

78. Johnson, J. C., Knutsen, K. P., Yan, H., Law, M., Zhang, Y., Yang, P. & Saykally, R. J. Ultrafast Carrier Dynamics in Single ZnO Nanowire and Nanoribbon Lasers. *Nano Letters* **4,** 197–204 (2004).

79. Peng, P., Milliron, D. J., Hughes, S. M., Johnson, J. C., Alivisatos, A. P. & Saykally, R. J. Femtosecond Spectroscopy of Carrier Relaxation Dynamics in Type II CdSe/CdTe Tetrapod Heteronanostructures. *Nano Letters* **5,** 1809–1813 (2005).

80. Smith, B. E., Roder, P. B., Zhou, X. & Pauzauskie, P. J. Nanoscale materials for hyperthermal theranostics. *Nanoscale* (2015).

81. Angelatos, A. S., Radt, B. & Caruso, F. Light-Responsive Polyelectrolyte/Gold Nanoparticle Microcapsules. *The Journal of Physical Chemistry B* **109,** 3071–3076 (2005).

82. Guo, C., Yin, S., Yu, H., Liu, S., Dong, Q., Goto, T., Zhang, Z., Li, Y. & Sato, T. Photothermal ablation cancer therapy using homogeneous Cs_xWO_3 nanorods with broad near-infra-red absorption. *Nanoscale* **5,** 6469–6478 (2013).

83. Smith, B. E., Roder, P. B., Hanson, J. L., Manandhar, S., Devaraj, A., Perea, D. E., Kim, W. J., Kilcoyne, A. L. D. & Pauzauskie, P. J. Singlet-Oxygen Generation from Individual Semiconducting and Metallic Nanostructures during Near-Infrared Laser Trapping. *ACS Photonics* **2,** 559–564 (2015).

84. Chatterjee, D. K., Fong, L. S. & Zhang, Y. Nanoparticles in photodynamic therapy: An emerging paradigm. *Advanced Drug Delivery Reviews* **60,** 1627–1637 (2008).

85. Ladj, R. *et al.* Aminodextran-coated potassium niobate ($KNbO_3$) nanocrystals for second harmonic bio-imaging. *Colloids and Surfaces A: Physicochemical and Engineering Aspects* **439,** 131–137 (2013).

86. Pantazis, P., Maloney, J., Wu, D. & Fraser, S. E. Second harmonic generating (SHG) nanoprobes for in vivo imaging. *Proceedings of the National Academy of Sciences* **107,** 14535–14540 (2010).

87. Weissleder, R. A clearer vision for in vivo imaging. *Nature Biotechnology* **19,** 316–317 (2001).

88. Fluck, D & Günter, P. Efficient generation of CW blue light by sum-frequency mixing of laser diodes in $KNbO_3$. *Optics Communications* **136,** 257–260 (1997).

89. Dickson, J. A. & Oswald, B. E. The sensitivity of a malignant cell line to hyperthermia (42°C) at low intracellular pH. *British Journal of Cancer* **34,** 262–271 (1976).

90. Kim, S., Lee, J.-H., Lee, J., Kim, S.-W., Kim, M. H., Park, S., Chung, H., Kim, Y.-I. & Kim, W. Synthesis of Monoclinic Potassium Niobate Nanowires That Are Stable at Room Temperature. *Journal of the American Chemical Society* **135,** 6–9 (2013).

91. Cullity, B. D. *Elements Of X-Ray Diffraction* (Addison-Wesley Publishing Company, Inc., 1956).

92. Douillard, L., Jollet, F., Bellin, C., Gautier, M. & Duraud, J. P. The electronic structure of KNbO3: an XPS and XAS study. *Journal of Physics: Condensed Matter* **6,** 5039 (1994).

93. Van der Ziel, J. Effect of Fabry-Perot interference on second harmonic generation in a GaAs plate. *IEEE Journal of Quantum Electronics* **12,** 407–411 (1976).

94. Umemura, N., Yoshida, K. & Kato, K. Phase-Matching Properties of KNbO_3 in the Mid-Infrared. *Applied Optics* **38,** 991 (1999).

95. Chakraborty, D., Gnann, M. V., Rings, D., Glaser, J., Otto, F., Cichos, F. & Kroy, K. Generalised Einstein relation for hot Brownian motion. *EPL (Europhysics Letters)* **96,** 60009 (2011).

96. Rings, D., Chakraborty, D. & Kroy, K. Rotational hot Brownian motion. *New Journal of Physics* **14,** 053012 (2012).

97. Grinberg, I. *et al.* Perovskite oxides for visible-light-absorbing ferroelectric and photovoltaic materials. *Nature* **503,** 509–512 (2013).

98. Magee, T. J., Peng, J. & Bean, J. Microscopic Defects and Infrared Absorption in Cadmium Telluride. *physica status solidi (a)* **27,** 557–564 (1975).

99. Smekal, A. Zur Quantentheorie der Dispersion. *Naturwissenschaften* **11,** 873–875 (1923).

100. Raman, C. V. & Krishnan, K. S. A New Type of Secondary Radiation. *Nature* **121,** 501–502 (1928).

101. Raman, C. V. A new radiation. *Indian Journal of Physics* **2,** 387–398 (1928).

102. Nakamoto, K. *Infrared spectra of inorganic and coordination compounds* (Wiley, 1963).

103. Gylys, V. T. & Rubin, L. F. Direct measurement of $O_2(a^1\Delta)$ and $O_2(X^3\Sigma)$ in chemical oxygeniodine lasers with use of spontaneous Raman imaging. *Applied Optics* **37,** 1026 (1998).

104. Levine, I. N. *Molecular spectroscopy* (Wiley, 1975).

105. Fletcher, W. H. & Rayside, J. S. High resolution vibrational Raman spectrum of oxygen. *Journal of Raman Spectroscopy* **2,** 3–14 (1974).

106. Frederick K. Lutgens. *Essentials of Geology* 11th ed. (Prentice Hall, Boston, 2012).

107. Rödl, C., Sander, T., Bechstedt, F., Vidal, J., Olsson, P., Laribi, S. & Guillemoles, J.-F. Wurtzite silicon as a potential absorber in photovoltaics: Tailoring the optical absorption by applying strain. *Physical Review B* **92,** 045207 (2015).

108. Wippermann, S., Vörös, M., Rocca, D., Gali, A., Zimanyi, G. & Galli, G. High-Pressure Core Structures of Si Nanoparticles for Solar Energy Conversion. *Physical Review Letters* **110,** 046804 (2013).

109. Fontcuberta i Morral, A., Arbiol, J., Prades, J. D., Cirera, A. & Morante, J. R. Synthesis of Silicon Nanowires with Wurtzite Crystalline Structure by Using Standard Chemical Vapor Deposition. *Advanced Materials* **19,** 1347–1351 (2007).

110. Zhang, Y., Iqbal, Z., Vijayalakshmi, S. & Grebel, H. Stable hexagonal-wurtzite silicon phase by laser ablation. *Applied Physics Letters* **75,** 2758–2760 (1999).

111. Kim, D. Y., Stefanoski, S., Kurakevych, O. O. & Strobel, T. A. Synthesis of an open-framework allotrope of silicon. *Nature Materials* **14,** 169–173 (2015).

112. Voronin, G. A., Pantea, C., Zerda, T. W., Wang, L. & Zhao, Y. *In situ* x-ray diffraction study of silicon at pressures up to 15.5 GPa and temperatures up to 1073 K. *Physical Review B* **68,** 020102 (2003).

113. Dyuzheva, T. I., Kabalkina, S. S. & Novichkov, V. P. Polymorphism of Silicon Under High-Pressure. *Zhurnal Eksperimentalnoi I Teoreticheskoi Fiziki* **74,** 1784–1787 (1978).

114. Hu, J. Z. & Spain, I. L. Phases of silicon at high pressure. *Solid State Communications* **51,** 263–266 (1984).

115. Hu, J. Z., Merkle, L. D., Menoni, C. S. & Spain, I. L. Crystal data for high-pressure phases of silicon. *Physical Review B* **34,** 4679–4684 (1986).

116. Tolbert, S. H. & Alivisatos, A. P. High-Pressure Structural Transformations in Semiconductor Nanocrystals. *Annual Review of Physical Chemistry* **46,** 595–626 (1995).

117. Fabbri, F., Rotunno, E., Lazzarini, L., Fukata, N. & Salviati, G. Visible and Infra-red Light Emission in Boron-Doped Wurtzite Silicon Nanowires. *Scientific Reports* **4** (2014).

118. Besson, J. M., Mokhtari, E. H., Gonzalez, J. & Weill, G. Electrical properties of semimetallic silicon III and semiconductive silicon IV at ambient pressure. *Physical Review Letters* **59,** 473–476 (1987).

119. Weill, G, Mansot, J. L., Sagon, G, Carlone, C & Besson, J. M. Characterisation of Si III and Si IV, metastable forms of silicon at ambient pressure. *Semiconductor Science and Technology* **4,** 280–282 (1989).

120. Demishev, S., Lunts, D., Nekhaev, D., Sluchanko, N., Samarin, N., Brazhkin, V., Lyapin, A., Popova, S. & Mel'nik, N. Structural relaxation of the metastable Kasper phase of silicon. *Journal of Experimental and Theoretical Physics* **82,** 1159–1167 (1996).

121. Yablonovitch, E. Photonic band-gap structures. *Journal of the Optical Society of America B* **10,** 283 (1993).

122. Joannopoulos, J. D., Villeneuve, P. R. & Fan, S. Photonic crystals: putting a new twist on light. *Nature* **386,** 143–149 (1997).

123. Birner, A., Wehrspohn, R. B., Gösele, U. M. & Busch, K. Silicon-Based Photonic Crystals. *Advanced Materials* **13,** 377–388 (2001).

124. Kennedy, S. R., Brett, M. J., Miguez, H., Toader, O. & John, S. Optical properties of a three-dimensional silicon square spiral photonic crystal. *Photonics and Nanostructures - Fundamentals and Applications* **1,** 37–42 (2003).

125. Bermel, P., Luo, C., Zeng, L., Kimerling, L. C. & Joannopoulos, J. D. Improving thin-film crystalline silicon solar cell efficiencies with photonic crystals. *Optics Express* **15,** 16986 (2007).

126. Garnett, E. & Yang, P. Light Trapping in Silicon Nanowire Solar Cells. *Nano Letters* **10,** 1082–1087 (2010).

127. Mao, H. K., Xu, J. & Bell, P. M. Calibration of the ruby pressure gauge to 800 kbar under quasi-hydrostatic conditions. *Journal of Geophysical Research: Solid Earth* **91,** 4673–4676 (1986).

128. Kittel, C. *Introduction to Solid State Physics* 8th ed. (John Wiley and Sons, 2005).

129. Khachadorian, S., Papagelis, K., Ogata, K., Hofmann, S., Phillips, M. R. & Thomsen, C. Elastic Properties of CrystallineAmorphous CoreShell Silicon Nanowires. *The Journal of Physical Chemistry C* **117,** 4219–4226 (2013).

130. Weinstein, B. A. & Piermarini, G. J. Raman scattering and phonon dispersion in Si and GaP at very high pressure. *Physical Review B* **12,** 1172–1186 (1975).

131. Tateiwa, N. & Haga, Y. Evaluations of pressure-transmitting media for cryogenic experiments with diamond anvil cell. *Review of Scientific Instruments* **80,** 123901 (2009).

132. Giannozzi, P. *et al.* QUANTUM ESPRESSO: a modular and open-source software project for quantum simulations of materials. *Journal of Physics: Condensed Matter* **21,** 395502 (2009).

133. Khachadorian, S., Papagelis, K., Scheel, H., Colli, A., Ferrari, A. C. & Thomsen, C. High pressure Raman scattering of silicon nanowires. *Nanotechnology* **22,** 195707 (2011).

134. Hsieh, W.-P. Thermal conductivity of methanol-ethanol mixture and silicone oil at high pressures. *Journal of Applied Physics* **117,** 235901 (2015).

135. Goncharov, A. F., Wong, M., Dalton, D. A., Ojwang, J. G. O., Struzhkin, V. V., Konôpková, Z. & Lazor, P. Thermal conductivity of argon at high pressures and high temperatures. *Journal of Applied Physics* **111,** 112609 (2012).

136. Plech, A., Kotaidis, V., Grésillon, S., Dahmen, C. & von Plessen, G. Laser-induced heating and melting of gold nanoparticles studied by time-resolved x-ray scattering. *Physical Review B* **70,** 195423 (2004).

137. Widmann, J. F. & Davis, E. J. Pulsed electromagnetic heating of microparticles. *International Journal of Heat and Mass Transfer* **41,** 4195–4204 (1998).

138. Allen, T. M., Buehler, M. F. & Davis, E. J. Radiometric effects on absorbing microspheres. *Journal of Colloid and Interface Science* **142,** 343–356 (1991).

139. Yang, P., Yan, R. & Fardy, M. Semiconductor Nanowire: Whats Next? *Nano Letters* **10,** 1529–1536 (2010).

140. Xing, J., Liu, X. F., Zhang, Q., Ha, S. T., Yuan, Y. W., Shen, C., Sum, T. C. & Xiong, Q. Vapor Phase Synthesis of Organometal Halide Perovskite Nanowires for Tunable Room-Temperature Nanolasers. *Nano Letters* **15,** 4571–4577 (2015).

141. Zhu, H. *et al.* Lead halide perovskite nanowire lasers with low lasing thresholds and high quality factors. *Nature Materials* **14,** 636–642 (2015).

142. Gu, F., Zhang, L., Yin, X. & Tong, L. Polymer Single-Nanowire Optical Sensors. *Nano Letters* **8,** 2757–2761 (2008).

143. Kelzenberg, M. D. *et al.* Enhanced absorption and carrier collection in Si wire arrays for photovoltaic applications. *Nature Materials* **9,** 239–244 (2010).

144. Berry, D. W., Heckenberg, N. R. & Rubinsztein-Dunlop, H. Effects associated with bubble formation in optical trapping. *Journal of Modern Optics* **47,** 1575–1585 (2000).

145. Haro-González, P., Rosal, B. d., Maestro, L. M., Rodríguez, E. M., Naccache, R., Capobianco, J. A., Dholakia, K., Solé, J. G. & Jaque, D. Optical trapping of NaYF4:Er3+,Yb3+ upconverting fluorescent nanoparticles. *Nanoscale* **5,** 12192–12199 (2013).

146. Xu, X. *et al.* Dynamics of Bound Exciton Complexes in CdS Nanobelts. *ACS Nano* **5,** 3660–3669 (2011).

147. Smith, B. E., Roder, P. B., Zhou, X. & Pauzauskie, P. J. Hot Brownian thermometry and cavity-enhanced harmonic generation with nonlinear optical nanowires. *Chemical Physics Letters* **639,** 310–314 (2015).

148. Draine, B. T. & Flatau, P. J. Discrete-dipole approximation for scattering calculations. *Journal of the Optical Society of America A* **11,** 1491–1499 (1994).

149. Purcell, E. M. & Pennypacker, C. R. Scattering and Absorption of Light by Nonspherical Dielectric Grains. *The Astrophysical Journal* **186,** 705–714 (1973).

150. Cheng, C., Fan, W., Cao, J., Ryu, S. G., Ji, J., Grigoropoulos, C. P. & Wu, J. Heat Transfer across the Interface between Nanoscale Solids and Gas. *ACS Nano* **5,** 10102–10107 (2011).

151. Park, J., Huang, J., Wang, W., Murphy, C. J. & Cahill, D. G. Heat Transport between Au Nanorods, Surrounding Liquids, and Solid Supports. *The Journal of Physical Chemistry C* **116,** 26335–26341 (2012).

152. Ekici, O., Harrison, R. K., Durr, N. J., Eversole, D. S., Lee, M. & Ben-Yakar, A. Thermal analysis of gold nanorods heated with femtosecond laser pulses. *Journal of Physics D: Applied Physics* **41,** 185501 (2008).

153. Veamatahau, A., Jiang, B., Seifert, T., Makuta, S., Latham, K., Kanehara, M., Teranishi, T. & Tachibana, Y. Origin of surface trap states in CdS quantum dots: relationship between size dependent photoluminescence and sulfur vacancy trap states. *Physical Chemistry Chemical Physics* **17,** 2850–2858 (2014).

154. Chestnoy, N., Harris, T. D., Hull, R. & Brus, L. E. Luminescence and photophysics of cadmium sulfide semiconductor clusters: the nature of the emitting electronic state. *The Journal of Physical Chemistry* **90,** 3393–3399 (1986).

155. O'Neil, M., Marohn, J. & McLendon, G. Dynamics of electron-hole pair recombination in semiconductor clusters. *The Journal of Physical Chemistry* **94,** 4356–4363 (1990).

156. Boyd, E. J., Li, L., Blue, R. & Uttamchandani, D. Measurement of the temperature coefficient of Young's modulus of single crystal silicon and 3C silicon carbide below 273 K using microcantilevers. *Sensors and Actuators A: Physical* **198,** 75–80 (2013).

157. Sandberg, R., Svendsen, W., Mølhave, K. & Boisen, A. Temperature and pressure dependence of resonance in multi-layer microcantilevers. *Journal of Micromechanics and Microengineering* **15,** 1454 (2005).

158. Kobiakov, I. B. Elastic, piezoelectric and dielectric properties of ZnO and CdS single crystals in a wide range of temperatures. *Solid State Communications* **35,** 305–310 (1980).